Discovering Intermetallics Through Synthesis, Computation, and Data-Driven Analysis

by

Sogol Lotfi

A Dissertation Submitted to the Department of Chemistry,
College of Natural Sciences and Mathematics

In Partial Fulfillment of the Requirements for the Degree of
Doctor of Philosophy
in Chemistry

Chair of Committee: Dr. Jakoah Brgoch

Committee Member: Dr. Allan Jacobson

Committee Member: Dr. Arnold Guloy

Committee Member: Dr. Zhifeng Ren

Committee Member: Dr. Ding-Shyue (Jerry) Yang

University of Houston
May 2020

Acknowledgment

My research would have been impossible without the help and support of my great, understanding, and fantastic advisor, Prof. Jakoah Brgoch. Jakoah, I am so grateful to have an opportunity to work with you, and I would like to thank you for your dedicated help, advice, inspiration, encouragement, and continuous support during these years. Before starting my Ph.D., I was a shy girl who avoided talking to people, but you taught me how to become a sociable person. As you always say, you build a character, and as I always say, you are the best advisor that every graduate student wants to work with. I gratefully acknowledge Prof. Guloy for his insightful discussion about my projects and generously letting me use the instruments in his lab. I show my sincere appreciation for Dr. Korp for patiently teaching me crystallography and made me find it so enjoyable. I would like to thank my Ph.D. committee members for their time and valuable feedback on a preliminary version of this thesis.

I want to thank my Brgoch group family, especially, Martin, Anna, Erin, Aria, Ya, Shruti, and Anton. Thank you all for the stimulating discussions, for the sleepless nights we were working together before deadlines, and for all the fun we have had in the last four years. Also, I thank George for his training when I started my research and my undergraduate researchers, Gayatri, Katy, and Pablo, who did the synthesis for me.

I also thank my friends who made my stay in Houston memorable: Parastou, Hamed, Farnaz, Vahed, Arvand, Hamid, Hamed, Helina, Azadeh, Sara, Shaghayegh, and Maryam. Parastou and Hamed, you two are beyond a friend for me, just like a family, I am always grateful for your support when I first came to the US. Farnaz, you are the sister that I got to

choose; I love you so much, and I will miss our road trips, parties, and all the fun plans we had. Vahed and Arvand, you guys are awesome, but my thesis would be 50 pages more if you two did not say every single day, “let’s plan out something”. Hamid, I am so glad to have a buddy like you, and I always admire your integrity. Hamed and Helina, you are great friends, and we made many good memories. Azadeh, Sara, and Shaghayegh, you were the best roommates who became amazing friends.

I am so grateful for my family in the US: Fatti Joon, Sahar Joon, Mehry Joon, Dayi Mansour, Bahman Joon, and Dear Susie. Thank you all for accepting me here in the family, and I do not know what I did to deserve you all. Fatti Joon, my appreciation can hardly be expressed in words. Thank you for your love, support, encouragement during these years; I am honored to be your daughter. Sahar Joon, you are the sister that I always wanted to have, thank you for standing next to me in every tough situation that I had. Mehry joon and Dayi joon, for as long as I can remember, you have motivated me and support me, thank you so much. Bahman Joon and Dear Susie, I never forget your kindness, and I greatly appreciate your love and support. I also want to thank Said, Rachel, Audrey, and our precious Ethan and Mason.

I must express my very profound gratitude to my amazing family, my mother, my father, and my brother, for all their love, support, motivation, and sacrifice during my Ph.D. All that I am, or hope to be, I owe to my angel parents, Maman Soheila and Baba Ali. Words cannot describe how grateful I am for all of your love, support, and patience during my Ph.D. Maman Joon, I will never forget that you wake up at 5 a.m. to call me every single day during these 5 years. Baba Joon, you always believe in me and motivates me with your magic words. Soroush azizam, if I could pick the best brother, I would pick you; I am always proud of you. Although I did not have you here, you were in my thought and heart all the time.

Finally, I want to dedicate my dissertation to my wonderful grandmother, Maman Aalieh, who taught me how to write for the first time. She had a very beautiful soul, and she would have been so proud of me if she was alive today.

Abstract

Intermetallics adopt an array of crystal structures, boast diverse chemical compositions, and possess exotic physical properties that have led to a wide range of applications from the biomedical to aerospace industries. Despite a long history of intermetallic synthesis and crystal structure analysis, identifying new intermetallic phases has remained challenging due to the prolonged nature of experimental phase space searching or the need for fortuitous discovery. New approaches with a specific focus on realizing novel intermetallics have been proposed that expand on traditional methods for materials synthesis and characterization. One of the most notable methods is to merge traditional intermetallic synthesis and characterization with computation and materials informatics, when combined, provide a new set of tools capable of advancing the discovery of metal-rich solids.

Each chapter of this dissertation employs solid-state synthesis, first-principle calculations, and machine learning to modernize how intermetallics are discovered and to better understand their complex structures. For example, we combined exploratory solid-state synthesis with *ab initio* calculations to investigate gold's polyanionic bonding in intermetallic phases. The application of density functional theory goes beyond merely studying the electronic structure and chemical bonding of intermetallics. We also utilized an *ab initio* approach coupled with a structure-search algorithm (CALYPSO) to predict the crystal structure of intermetallics under pressure. Our research revealed the existence of two binaries in the *A*-Ir (*A* = Rb, Cs) system over ~10 GPa. Further, a new approach merging experimental work, computation, and data-driven analysis to discover intermetallics was created. We developed a machine-learning model to predict the formation energy of metal-

rich solid based only on the constituent elements followed by experimental validation through the subsequent synthesis of a novel compound, $YAg_{0.65}In_{1.35}$. Finally, exploratory synthesis was carried out on the ternary *RE*-Au-Ge (*RE* = La, Ce, Pr, Nd) phase system leading to the discovery of six novel compounds: La_3Au_3Ge, La_2Au_2Ge, and RE_2AuGe_3 (*RE* = La, Ce, Pr, Nd). The research results presented in this dissertation discuss the opportunities and challenges in the discovery of new intermetallic phases while new approaches that merge synthesis, computation, and data science to accelerate the realization of metal-rich materials are created.

Table of Contents

List of Figures

List of Tables

Chapter 1

Introduction

Modified from *Chemistry—A European Journal*

(*Chem.: Eur. J*, 2020)

DOI: 10.1002/chem.202000742

Sogol Lotfi[1] and Jakoah Brgoch[1,2]*

[1]*Department of Chemistry, University of Houston, Houston, Texas 77204, United States*

[2]*Texas Center for Superconductivity, Houston 77204, Texas, United States*

1.1 Classifying Intermetallics Compound

One of the primary research goals pervasive across all subdisciplines of chemistry is to establish robust rules that allow for the categorization of compounds or materials using simple, recognizable empirical parameters such as the valence electron concentration or chemical composition. Intermetallic compounds in solid-state chemistry are no different. For instance, taking the ratio of valence electrons per atom (e/a) is a classical approach for classifying these materials into general groups, including Zintl phases, polar intermetallics, and Hume-Rothery phases. Generally, the conductive nature of intermetallic compounds increases by reducing the ratio of valence electrons per atom, (e/a), going from semiconducting Zintl phases to metallic Hume-Rothery phases.[1] As illustrated in Figure 1.1, a majority of the periodic table can adopt at least one of these types of compounds, and most can assume all three depending on the mixture of elements.

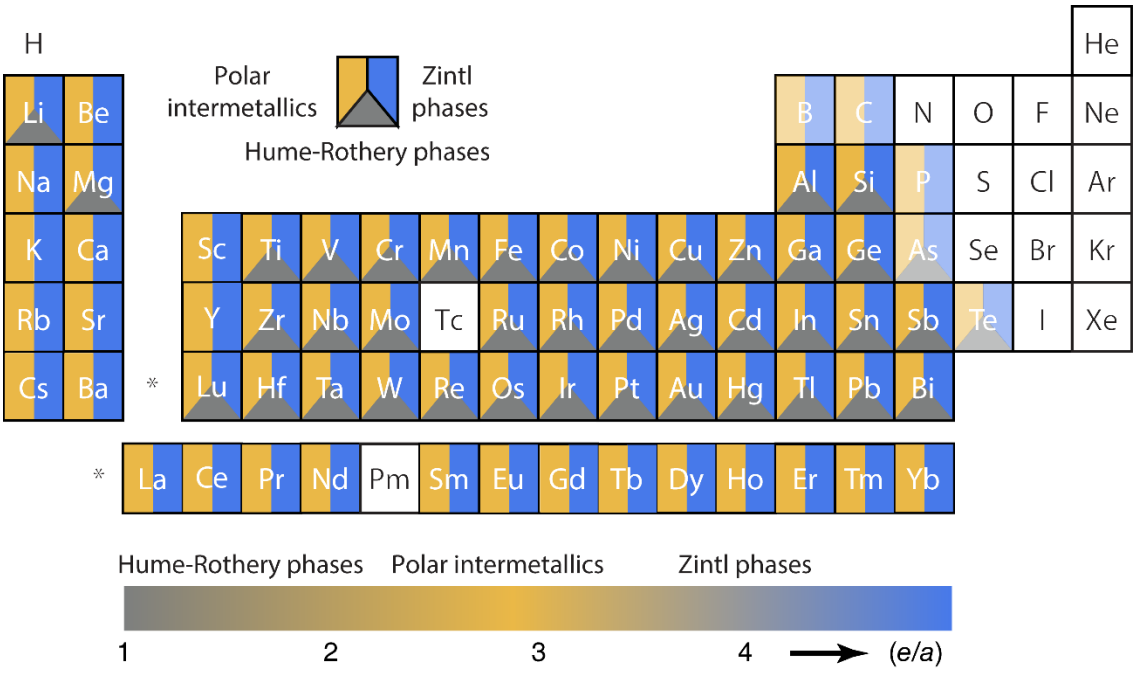

Figure 1.1. The elements in the periodic table that are reported in the literature to form intermetallics. The Zintl phase, polar intermetallics, and Hume-Rothery phases are shown by blue, yellow, and grey, respectively. The faded elements along the semi-metal line are also called intermetallics though this varies by the research field.

Historically, Zintl phases have consisted of combinations of cations from the alkali and alkali earth metals, and anions from the p-block elements (groups 13-15), where (e/a) ≥ 4. The significant difference in electronegativities between these elements results in a formal charge transfer between the ions allowing the elements to nominally follow the octet rule and making them salt-like semiconductors. For example, NaZnSb crystallizes in NaFeAs-structure type and is composed of alternating bilayers of Na^+ cations and polyanionic $[ZnSb]^-$ slabs.[2,3] Following the Zintl electron counting approach, the charge balanced composition, $Na^+Zn^{2-}Sb^+$, can be considered implying that Sb with 5 valence electrons loses an electron to become 4-bonded while Zn gains 2 more electrons to be 4-bonded and achieves an octet.[2] Recently, this concept has been revised, and rare-earth metals and transition metals have also been included in the Zintl phase category.[4] The ability for these compounds to achieve closed-shell electron configurations has allowed

scientists to assign oxidation states, which is rare in solid-state chemistry. Moreover, simple electron counting rules can be created, helping scientists design numerous novel Zintl phases with applications ranging from thermoelectrics and photovoltaics to topological insulators and Dirac semimetals.[1,5]

Reducing the number of electrons per atom to an (e/a) between ~ 1.2 and 4.0 results in another type of inorganic solid called a polar intermetallic.[6] Different from Zintl phases, there are currently no straightforward approaches to unambiguously count electrons or assign valence charges in these metals, making it hard to generalize polar intermetallics.[7] However, there are specific compositions that can be classified as polar intermetallics. For example, Laves phases, with the general composition AB_2, are one of the most significant subsets of polar intermetallics and can also be further classified into three groups based on the structure type: cubic $MgCu_2$-type, hexagonal $MgZn_2$-type, and hexagonal $MgNi_2$-type.[8,9] The primary factor governing the stability of these three relatively simple crystal structures is the electron concentrations of the constituent metals, allowing a homogeneity range for each crystal type.[10] Polar intermetallics also form complex crystal structures and adopt distinct features of chemical bonding that range from networks to clusters and even quasicrystals.[11] For example, K_3Au_5Tl, with e/a ≅ 1.83, form the puckered sheet of corner-connected gold tetrahedra while the voids are filled with potassium.[6,12] Finally, Hume-Rothery phases occur when the $1 \leq e/a \leq 2$, and they also have homogeneity ranges (although they are not line-compounds). The electrons concentration mostly controls Hume-Rothery phase formation and plays a leading role in the selection of crystal structures, whereas electronegativity and size are not as important.[13]

Although simple “design” strategies like these have allowed chemists to categorize compounds or crystal structures using empirical rules such as the electron count, the

creation of these rules was generally in retrospect. A majority of the known intermetallic phases were first discovered using classical trail-and-error solid-state synthesis or serendipitous discovery, and then the empirical rules were established. Given the critical importance of these materials, with many finding uses in modern applications like structural and magnetic materials, energy-storage and corrosion-resistant materials, heat-resistant aerospace materials, and biomedical applications, an approach to discover new metal-rich solids would be valuable.[14] Here, classical and modern strategies developed to identify new intermetallic compounds are discussed with a specific focus on merging synthesis and characterization with computation and materials informatics.

1.2 Experimental Techniques for the Discovery of Complex Intermetallics

1.2.1 Solid-State Synthetic Routes for Intermetallics Compounds

Before any new computational or data-driven materials discovery can take place, it is necessary first to understand the importance of different synthetic techniques used to prepare intermetallics and how these experimental approaches have led to our current understanding of solid-state chemistry. In general, intermetallics are formed in a single-step process where starting materials (often elemental pieces) are reacted through solid-solid diffusion.[15,16] The extreme temperatures used for these reactions necessitate containers that can not only withstand elevated temperatures but also do not react with the starting materials. Silica tubes, ceramic crucibles (*e.g.*, MgO, Al_2O_3, ZrO_2), metal crucibles (*e.g.*, Ag, stainless steel, Pt), and metal tubes (*e.g.*, Nb, Ta, W) are the most common reaction containers with the selection of the container depending entirely on the planned reaction temperature as well as the starting materials.[17] The heating profile used for reaction usually starts by choosing a temperature treatment that is at least 2/3 of the lowest melting point

starting material to maximize diffusion (Tammann's rule).[18,19] These sintering reactions are carried out in muffle or tube furnaces when the maximum required temperature is less than ~1700°C, which is usually the limit of conventional furnaces. If the reaction temperature is lower than ~1100°C, the samples can be sealed in evacuated silica tubes that have been flame sealed, whereas higher temperatures require using a vacuum furnace or flowing an inert gas like argon. To achieve an even high-temperature regime, another common reaction route for the preparation of intermetallics is arc-melting. Arc-melting can quickly achieve temperatures over ~2000°C using a water-cooled copper hearth to hold the sample, a gas (*e.g.*, argon or nitrogen) filled chamber, and an electrode (often tungsten-based) to strike a plasma. Given the enormous temperatures produced, arc-melting is limited to nonvolatile elements allowing most transition metals to be reacted and complex intermetallics products to be formed. Some elements are challenging to arc-melt like Mn or Sb while elements like Zn are almost impossible owing to their high vapor pressure.[20–24] If external pressure and temperature are both required to synthesize the desired compound, spark plasma sintering (SPS) is a viable approach to apply simultaneous temperature and pressure. Fast heating rates are achieved in SPS by employing pulsed, high DC current, and uniaxial pressure also allows shorter sintering times compared to using conventional furnaces, which can be advantageous. [25–27] An additional convenience of SPS is that the combination of temperature and pressure can produce a (nearly) fully dense sample that may be required for physical property measurements. Further, it is possible to use flux reactions where a molten solid can be used as a solvent. In many examples, the molten solvent (also called reactive flux) can also be used as a reagent that is required for the formation of final products.[28] The flux method, with its lower temperature and slow cooling rates, is ideal for large single crystal

growth. In the following section, metal flux is described in more detail as an effective synthetic method for the growth of the single crystal.

This brief description of synthetic approaches is by no means exhaustive, and all methods have their advantages and disadvantages, meaning it is essential to consider each possible route for every composition space explored. In some cases, multiple synthetic routes are required for the comprehensive investigation of a sophisticated composition space, which is one of the challenges in intermetallic synthesis.

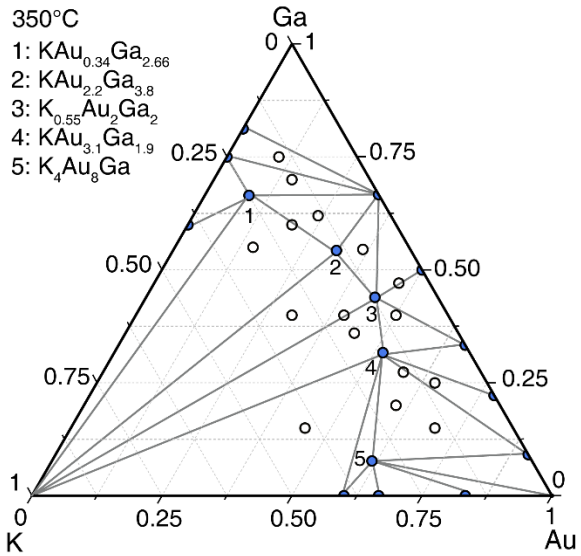

Figure 1.2. K–Au–Ga ternary phase diagram at 350°C. The open circles indicate compositions loaded, whereas points marked 1–5 were compounds identified by single-crystal X-ray diffraction (1: $KAu_{0.34}Ga_{2.66}$, 2: $KAu_{2.2}Ga_{3.8}$, 3: $K_{0.55}Au_2Ga_2$, 4: $KAu_{3.1}Ga_{1.9}$, 5: K_4Au_8Ga). This figure is adapted from reference 32.

The most traditional method to discover new compounds using these synthetic techniques is to examine a phase diagram systematically. A phase diagram depicts a material's state at thermodynamic equilibrium as a function of composition, temperature, and pressure; however, the pressure is often kept constant for more straightforward illustration. Experimental phase diagrams are constructed by either dynamic (thermal

analysis) or non-dynamic (static) methods. In the thermal analysis, the equilibrated phase is determined by analyzing a sample upon cooling or heating, while in the latter method, the phase diagram is achieved by studying the product of quenched samples to construct isothermal sections.[29,30]

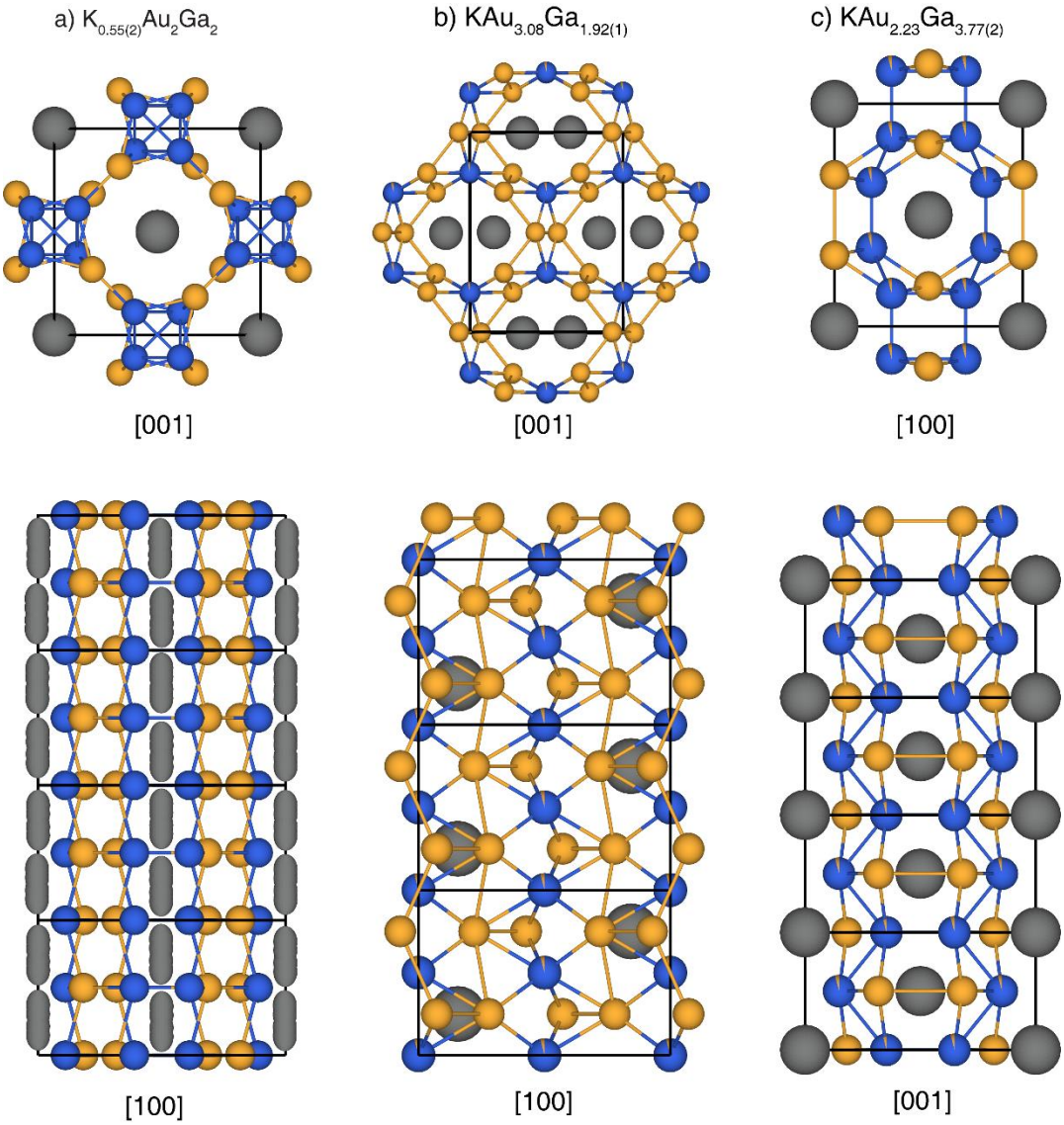

Figure 1.3. View of the crystal structure of a) $K_{0.55(2)}Au_2Ga_2$ with space group *I*4/*mcm*, b) $KAu_{3.08}Ga_{1.92(1)}$ with space group *Cmcm*, and c) $KAu_{2.23}Ga_{3.77(2)}$ with space group *Immm*, with projections along and normal to cation tunnels (K) at the top and bottom. The K, Au, Ga atoms are shown in grey, yellow, and blue, respectively. The potassium atoms in the $K_{0.55(2)}Au_2Ga_2$ structure is shown in the ellipsoid because of the disorder (reference 32).

Phase diagram exploration is an invaluable tactic that permits researchers to identify new compounds, and as a chemist looking for new crystal structures, exploring phase diagrams is arguably one of the most classical methodologies.[31] Smetana *et al.*,[32] for example, used this approach when they synthesized twenty-one different compositions in the K-Au-Ga ternary phase in a systematic search for new compounds. The results of this work were four ternary potassium gold gallides with compositions $K_{0.55}Au_2Ga_2$, KAu_3Ga_2, KAu_2Ga_4, the solid solution KAu_xGa_{3-x} (x = 0−0.33), and confirmation of K_4Au_8Ga.[33,34] Each new compound was solved by selecting single crystals picked from the bulk sample and using single-crystal X-ray diffraction to determine the crystal structure of the unknown phase.[35] Energy-dispersive X-ray spectroscopy was used to confirm the refined chemical composition.[4] Subsequently, the phase diagram for the K-Au-Ga isothermal section (at 350°C) could be created by analyzing the products from each reaction using powder X-ray diffraction and then constructing the plot shown in Figure 1.2 following the lever rule. The crystal structure of $K_{0.55(2)}Au_2Ga_2$, $KAu_{3.08}Ga_{1.92(1)}$, and $KAu_{2.23}Ga_{3.77(2)}$ solved by single-crystal X-ray diffraction are shown in Figure 1.3 with two orthogonal views of each crystal structure. $K_{0.55(2)}Au_2Ga_2$, Figure 1.3a, adopts the body-centered tetragonal $K_{0.5}Pt_2Si_2$ structure type. The network structure are formed of a packing of tetrahedral stars (TSs, ~stellae quadrangulae), while each of which consists of an inner Ga_4 and an outer Au_4 tetrahedron. $KAu_{3.08}Ga_{1.92(1)}$, Figure1.3b, crystallizes with an orthorhombic *Cmcm* space group and is isostructural with $BaZn_5$ and $LaAl_3Ni_2$. In this structure, Au and Ga build the polyanionic tunnels where the eleropositive K atoms are placed in between. In contrast to $K_{0.55(2)}Au_2Ga_2$ structure, the polyanionic networks are not linear, and potassium atoms form two-dimentional zigzag chains. This peculiar packing is relatively dense; thus, it leaves no large voids in the structure. $KAu_{2+x}Ga_{4-x}$ ($KAu_{2.23}Ga_{3.77(2)}$), Figure 1.3c, represents a new

body-centered orthorhombic structure type with *Immm* space group. The polyanionic network of this structure is a 20-vertex K-centered $Au_{8+1.5x}Ga_{12-1.5x}$ (x = 0.23(1)) polyhedron with D_{2h} symmetry. In terms of tunnels, this compound can be defined as an average variant of $K_{0.55(2)}Au_2Ga_2$ and $KAu_{3.08}Ga_{1.92(1)}$: the tunnels are linear as in $K_{0.55(2)}Au_2Ga_2$, but with cations surrounded by Au/Ga cages, as observed in $KAu_{3.08}Ga_{1.92(1)}$.

1.2.2 Crystal Growth of Intermetallic Compounds

Extremely high-temperature and lack of liquid solvents in solid-state synthetic routes lead to difficulties growing high-quality single crystal. High-quality single crystals are essential for measuring the magnetic, physical, and electronic properties of intermetallics.[36] Flux growth is one of the more common techniques for producing large single crystal because of the methods simplicity and low cost.[4] For intermetallic reactions, low melting point metals from group 13-15 or an excess of a reactant (called a self-flux) are used as a molten solvent.[35] All the starting metals are weighed out in the desired stoichiometric ratios and placed in the inert crucible with metals the with higher melting temperatures are placed underneath the lower melting point metals, as shown in Figure 1.4.[36] The crucible is then sealed in a fused silica tube and placed in a furnace programmed with the desired temperature profile.[36] Reaction profile including heating/cooling rates, the dwell times at high/low temperatures, and the dwell temperatures can dictate the phase formation as well as the crystal sizes.[35] After the reaction has run, the crystals can be separated from the excess flux either by centrifugation or chemical etching process. Centrifugation process can be performed by using the plug of quartz wool above the crucible that acts as a filter during the flux removal. After crystals grow, while the temperature is still above the melting point of the flux, the ampoule is placed in the cup of a centrifuge and quickly spun, leading to

separation of liquid flux with crystals.[36] Care must be taken; centrifugation can be carried out for the reactions which there is no seeding problem caused by the presence of the quartz wool dust. Differently, chemical etching is another practical approach for the separation of crystals. For instance, the surface of single-crystal in many Al-flux growth can be cleaned by NaOH solution, and Ga and In flux can be eaten by diluted acid such as HCl.[28] Figure 1.4 illustrates an example of a flux reaction profile to prepare Ce-Pd-Ga ternary compounds where different cooling rates and dwell times results in the formation of different crystal structures.[37–39] The temperature profile is not the only variable that can control crystal structure formation. In some cases, it is possible to relate the stoichiometric ratio of flux reactives with the resulting crystal structures. For example, by increasing the In amount as a molten solvent in the metal fluxes of Eu-In-Sb ternary phase system, the size of crystals as well as the crystal structures' preference.[4,40]

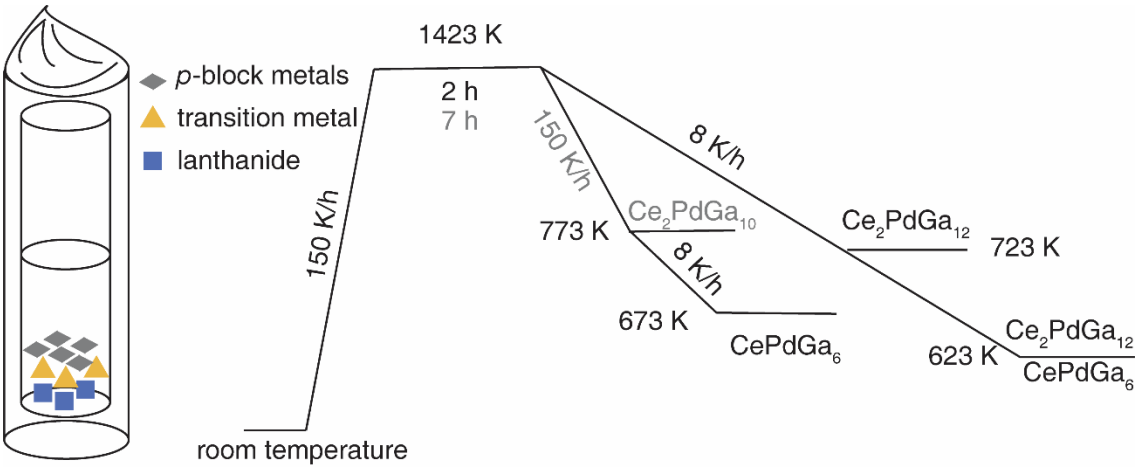

Figure 1.4. Schematic of a reaction container and temperature profile indicating the single crystal growth of $CePdGa_6$, Ce_2PdGa_{10}, and Ce_2PdGa_{12}. This figure is adopted from reference 34.

Although flux techniques are well established and have led to numerous intermetallic discoveries, the size of crystal grown by this method are still generally too

small for certain experiments where very large crystals are needed, like inelastic neutron scattering. There are other suitable methods for the growth of intermetallic single crystals such as chemical vapor transporter (CVT) and the Czochralski method.[41–44]

Despite decades of success on discovering new intermetallic compounds using this approach, phase space searching is laborious and challenging.[45] Difficulties in crystal growth, the lower thermodynamic stability of intermetallics in comparison with oxides and chalcogenides, and complex phase diagrams remain significant obstacles for identifying new metal-rich compounds. Thus, more efficient techniques that combine classic exploratory synthesis with computational-based approaches might prove beneficial to the field.

1.3 DFT-Based Intermetallics "Design" Approaches

Predicting new inorganic solids solely from their chemical composition has been a long-standing challenge in solid-state chemistry. The hope has been to improve the efficiency of materials discovery by reducing the number of synthetic attempts required to produce a new compound. Fortunately, using first-principles calculations has become a promising approach to predict the likely formation of new compounds.

1.3.1 Crystal Structure Prediction, Formation Energy Prediction, and Convex Hull Analysis

Computational efforts for intermetallic discovery have primarily focused on predicting the crystal structure for a given composition, then determining the formation energy from first-principles, and in some cases, constructing complete phase diagrams using convex hull calculations. Evolutionary algorithms like particle swarm optimization (PSO)[46], genetic

algorithms (GA),[47] and *ab initio* random structure search (AIRSS)[48] have each been paired with density functional theory (DFT) codes to create an effective methodology to predict crystal structure without previous knowledge of structure types. There are numerous implementations of these algorithms used for intermetallic with the most common codes for GA being Universal Structure Predictor Evolutionary Xtallography (USPEX),[49] Global Space-Group Optimization (GSGO),[50] XtalOpt,[51] and EVO[52] whereas the code Crystal Structure Analysis by Particle Swarm Optimization (CALYPSO)[53] employs a PSO. In each case, these algorithms generate crystal structures following the PSO or GA algorithm, and DFT is used to calculate the total internal energy of the phases. The crystal structure with the lowest total energy (local or global) is suggested to be the most probable structure type for a given composition. The convex hull for each binary or ternary system can also be constructed using these computational data to identify the most thermodynamically stable phase for a composition space (at least at zero Kelvin). There are numerous imaginable applications where using such a crystal structure prediction algorithm would be advantageous; however, the most common use has been in the high-pressure community, which has driven the development of these codes. Only more recently have these approaches been applied to the identification of new functional materials.

1.3.2 Intermetallic Crystal Chemistry under High-Pressure

High-pressure synthesis and materials characterizations are incredibly complex, rigorous, and generally limited because it requires extensive synthetic resources and specialized techniques such as high-pressure presses or a diamond anvil set-up. Crystal structure prediction algorithms, in conjunction with DFT, are a practical alternative to discover crystal structures under non-ambient pressure. Indeed, computational crystal structure

prediction lessens the high-pressure synthesis efforts necessary to develop a fundamental understanding of high-pressure chemistry. DFT paired with crystal structure prediction algorithms have been successfully employed for the discovery of novel materials at non-ambient conditions such as metal hydrides, oxides, nitrides, and noble gases.[54–59] There are fewer examples reported in the literature for intermetallic crystal structure prediction using DFT, although there are some notable examples. CsAu, with a CsCl-type structure, is a classic Zintl phase. Interestingly, applying high-pressure to the semiconducting CsAu through the program CALYPSO revealed that this composition is expected to undergo a crystal structure transformation and that the resulting high-pressure phase should be a poor metal.[60] As illustrated in Figure 1.5, the cubic crystal structure of CsAu with no metallic bonding transform orthorhombic space group *Cmcm* with metallic bonding. In a similar vein, first-principles calculations were employed to predict the formation of binary intermetallic compounds under high-pressure even though they do not form under ambient conditions; for example, the existence of A_3Ir (A = K, Rb, Cs) above 10 GPa was suggested using CALYPSO.[61,62] In each of these examples, computational modeling was essential due to difficulties in the high-pressure synthesis of alkali and alkali earth metals compounds. However, many questions regarding how intermetallics behave under pressure including crystal structure preference, the mechanisms governing phase transformations, and changes in the ensuing chemical bonding, remain unanswered; clearly, this is one field where additional research could lead to a unique understanding of high-pressure intermetallic crystal chemistry.

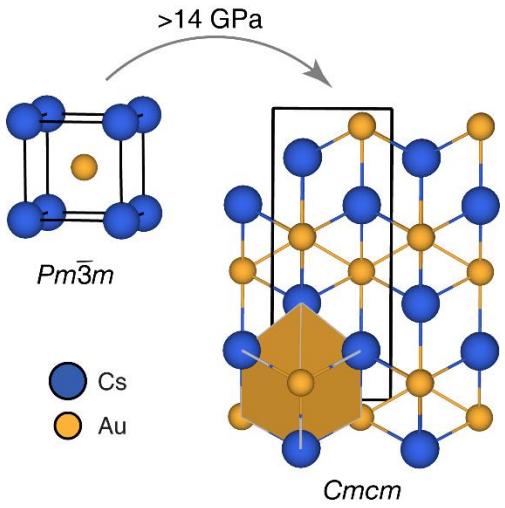

Figure 1.5. View of CsAu crystal structure at ambient pressure and pressure more than 14 GPa. CsAu forms a cubic CsCl-type structure at 0 GPa, while the crystal structure transforms *Cmcm* space group by applying pressure more than 14 GPa. Cs and Au are shown in blue and yellow, respectively. This figure is adapted from reference 59.

1.3.3 Functional Intermetallics

A compound's crystal structure is central for unlocking superior properties. As a result, predicting the structure of solid *a priori* has been a critical focus of researchers striving to find new functional materials. Computational chemists often focus on the prediction of interesting intermetallics with a wide range of industrial applications such as superconductors,[63] high hardness materials,[64,65] and intermetallics for lithium-ion batteries anodes,[66] among numerous other uses. For example, stable superconducting phases of $BaGe_3$ have been studied under normal and high pressure by using structural analogies and the evolutionary algorithm implemented in XtalOpt.[67] In this study, the predicted phases are suggested to be possibly superconducting from the calculated electron–phonon coupling strength. In another report, the stable and metastable binaries in Li-Sn and Li-Sb systems have been discovered with the aid of *ab initio* random structure searching (AIRSS).[68] Here, computational modeling was used to determine the trends in the lithiation process by

calculating the theoretical average voltage for predicted structures, which was not considered in the original experimental work. In the investigation for superhard materials, the crystal structure of ZrB_4 was predicted and proved to be thermodynamically and dynamically stable.[69] According to this research, the calculated bulk and shear moduli of ZrB_4 predicted structures are close to the experimentally reported CrB_4, WB_4, and FeB_4. This work highlighted the importance of using CALYPSO to predict a superhard response in ZrB_4, although experimental confirmation is needed.

1.3.4 DFT-Directed Intermetallic Synthesis

The ultimate aim of employing computation in chemistry is to guide the experimental efforts. In the last decade, DFT has been deployed to simplify experimental obstacles where the success in some syntheses would be impossible without computational accompaniment. Again, high-pressure chemistry is one of the research areas that DFT implementation has significantly aided the experimental attempts. For example, during the systematic search for heavy fermion and superconductor materials, $YbMn_2Ge_2$ has been examined under high pressure.[70] $YbMn_2Ge_2$, with the general composition RET_2X_2 (RE = rare earth, T = transition metal, and X = Ge or Si), crystallizes in the body-centered tetragonal space group $I4/mmm$ with a $ThCr_2Si_2$-type structure. The experimental investigation of $YbMn_2Ge_2$ under high pressure indicates the existence of a new pressure-induced phase, where the USPEX evolutionary algorithm has been applied for identifying the structural transition. Their calculations demonstrate a $P1$ structure with lower enthalpy, while the Le Bail fitting confirms both phases with similar cell parameters.

The creation of these crystal structure prediction algorithms combined with advances in highly parallel DFT-level calculations has also allowed researchers to

investigate unexplored ternary phase spaces efficiently. For example, theoretical calculations have been applied to investigate the crystal structure of $SrPtBi_2$, the only ternary composition in the Sr-Pt-Bi phase space, as illustrated in Figure 1.6.[71] In this research, an adaptive genetic algorithm (AGA), without any assumptions on the Bravais lattice type, atom basis, or unit cell dimensions, predicted an orthorhombic crystal structure for $SrPtBi_2$ (space group *Pnma*). The prediction was then proved by synthesizing the compound and analyzing the product using single-crystal X-ray diffraction. Further, the AGA methodology has assisted scientists in solving the puzzle of structural complexity in polymorphic structures. Zr_2Co_{11} is one example of this idea. Prior studies showed that rapid quenching of the composition produced numerous metastable phases, which could not be distinguished using X-ray diffraction. However, AGA implemented in the POTFIT code allowed the researchers to determine each Zr_2Co_{11} polymorph and understand their magnetic properties.[72]

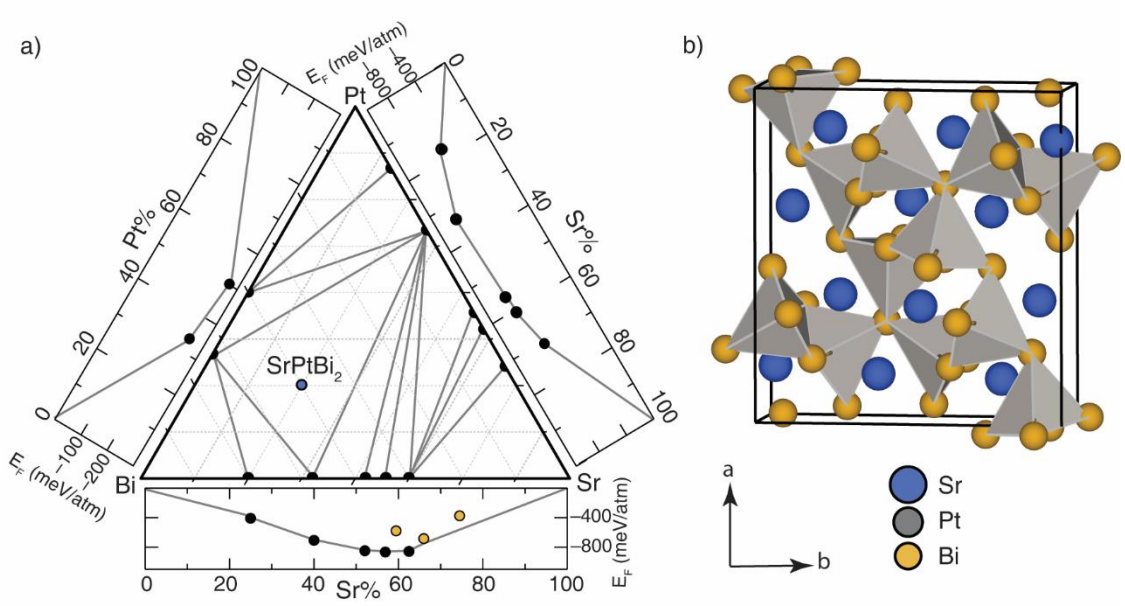

Figure 1.6. a) Sr-Pt-Bi convex hull. Black dots indicate the stable phases, while the yellow dots are the metastable phases. According to the DFT calculation, $SrPtBi_2$ is thermodynamically stable that was identified using computation. b) Crystal structure of the synthesized $SrPtBi_2$. Sr, Pt, and Bi are shown in blue, grey, and yellow, respectively. The convex hull and crystal structure are adapted from reference 70.

1.4 Materials Informatics for the Discovery of Intermetallic Compounds

First-principles computational modeling has played a significant role in uncovering novel crystal structures. Developments in high throughput electronic structure calculations have also resulted in the creation of massive databases containing crystal-chemical information. Multiple DFT databases (The Materials Project,[73] AFLOW,[74], and OQMD[75]) have been produced, while CITRINE INFORMATICS[76] has accumulated both experimental and DFT data. Researchers are now creating procedures to utilize this information for the development of new materials. In particular, materials informatics and machine-learning techniques have provided the ability to use the trove of information in these data sets to rapidly and often accurately predict the inorganic compound's preferred crystal structure or physical properties.[77]

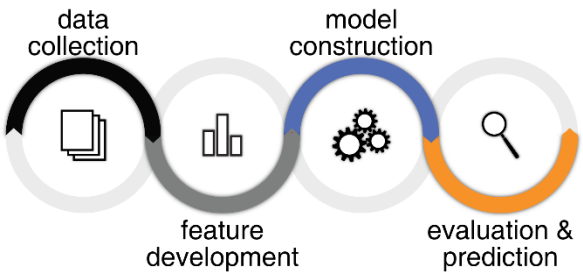

Figure 1.7. Schematic of a machine learning procedure flow. This figure is adapted from reference 64.

The general procedure of machine learning models consists of three integral components: (i) Data collection, (ii) Data representation, (iii) Model construction. Figure 1.7 indicates the schematic of the machine-learning process. The initial step is to select an appropriate resource for training data. Since the data in chemistry and materials science is not as well-developed as other research communities like biology and computer science, this step requires additional attention.[78] Primarily, chemistry databases were restricted to crystal structure experimental-based, such as Inorganic Crystal Structure Database (ICSD)[79] and Pearson's Crystal Data (PCD). However, with growing of computational capability, DFT databases (The Materials Project, AFLOW, and OQMD) have been introduced, while CITRINE INFORMATICS has accumulated both experimental and DFT data. Once a set of data is collected, features (descriptors/attributes) need to be created. In chemistry framework, they are generally based on physical/chemical properties and crystal structures. Finally, the last part of the ML process is model construction, where an appropriate ML algorithm for learning a function is chosen. Broadly, the learning process can be supervised (labeled) and unsupervised (unlabeled), relying on whether the prediction outputs are qualitative or quantitative. In chemistry and materials science, the most common algorithms are supervised ones. Support vector machine (SVM),[80] support vector regression (SVR),[81] and random forest algorithms[82] are the perfect example of this case, which is used mostly for

predicting the novel crystal structures, formation energies, and energy of convex hull. Machine learning guided studies for uncovering new materials are categorized into two subgroups, as outlined here.

1.4.1 Data-Driven Formation-Energy Prediction

Formation energy is vital for identifying novel compositions since this property is directly related to the energetic stability of a compound with respect ot the starting materials. The more negative the value of formation energy, the more stable the phase is expected to be with respect to decomposition to competing phases. This is further revealed by determining the convex hull of a compound, which shows phase relationships at equilibrium. Machine learning has been mostly applied to predict both the formation energy as well as calculate the convex hull for specific crystal structure types. For example, novel quaternary Heusler compounds ($F\bar{4}3m$, XX'YZ) were identified by predicting the favorable formation of energy and convex hull distances. These materials show superior properties such as ultralow thermal conductivity and high dielectric constant, therefore identifying new compositions of potential interest.[83,84] Kim *et al*.[85] applied the 462,148 crystalline compounds contained in the OQMD database as a training set for a Random Forest algorithm. The formation energies and convex hull of each composition were then used to predict the existence of 55 previously unknown quaternary Heusler compounds. It is suggested that novel, stable compounds could be discovered at a rate of 30 times faster than undirected search. Machine learning models have also been created based on predicting the formation energy of compounds using DFT training data, producing a model that can suggest compositions that are likely to form new compounds. For example, the Y-Ag-In ternary system is one of the phase spaces where energetically favorable areas in the phase diagram were identified by

machine learning the formation energies. This allowed the researchers to target compositions with a high probability of forming new compounds.[86] The successful outcomes from each of these examples highlight the power of machine learning guided synthesis as a general methodology for materials discovery.

1.4.2 Crystal Structure Prediction from Big Data

Predicting the crystal structure of intermetallics is a multidimensional problem because adopting a specific crystal structure type relies on a combination of number intrinsic factors like elemental properties as well as extrinsic factors such as synthetic conditions. Recently, machine learning has been successfully applied to overcome some of these barriers and predict the most likely crystal structure for any given chemical composition.[87,88] Indeed, the capability for machine learning to address the crystal structure prediction problem has led to the discovery of thermoelectric, semiconductor, photovoltaic, and battery materials.[89–94] The success of applying machine learning to crystal structure prediction has also assisted in solving inherent experimental synthesis and characterization issues. For example, CsCl-type, Heusler, and inverse Heusler structures are extremely difficult to distinguish by X-ray diffraction, as illustrated in Figure 1.8, because the superstructure peaks (111, 311, 331) are generally very weak, even with synchrotron radiation. To address this issue, machine learning was applied to predict the most likely Heusler structure with AB_2C compositions.[95] The prediction engine was constructed using random forest algorithms and contained almost 400,000 compounds for the training set. Subsequently, a series of 12 predicted gallides with the general composition $M\mathrm{Ru_2Ga}$ and $\mathrm{Ru}M_2\mathrm{Ga}$ (M = Ti−Co) were synthesized to confirm the crystal structure prediction.

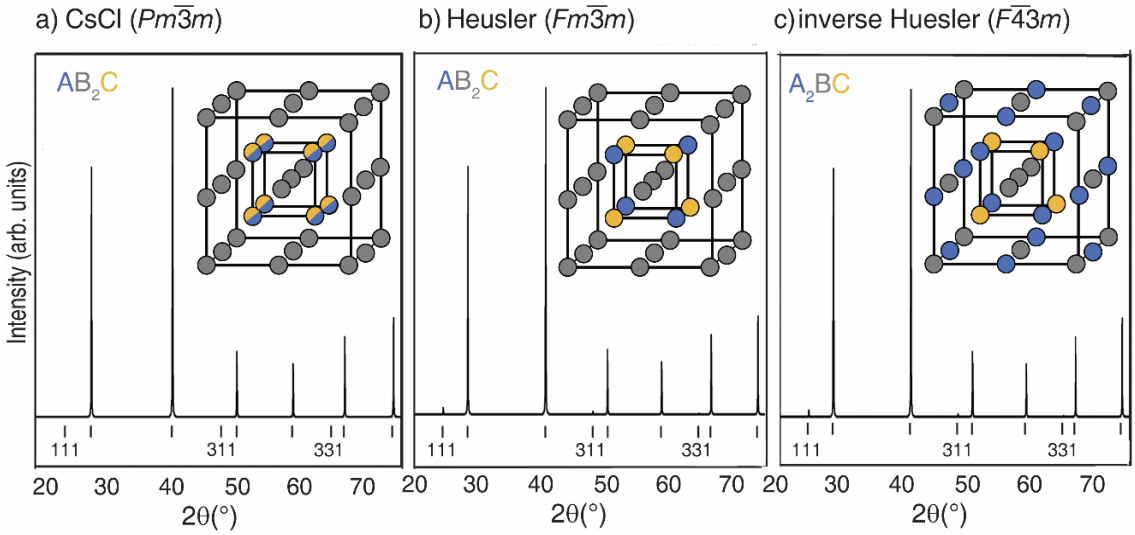

Figure 1.8. a) Simulated powder X-ray diffraction of CsCl-type, Heusler (Cu_2MnAl-type), and inverse Heusler (Hg_2CuTi-type) crystal type structure for $LiAg_2Al$. b) Powder X-ray diffraction for $TiRu_2Ga$, illustrating the weak superstructure reflections for a Heusler structure. c) Crystal structure of $TiRu_2Ga$. The small diffraction peaks labeled by their Miller indices highlight the difficulty confirming the correct structure type. This figure is adapted from reference 94.

The idea of using materials informatics and machine learning for crystal structure prediction has been expanded to also simplify structure determination and refinements for extended solids. Viswanathan *et al.* developed a model, single-crystal automated refinement (SCAR), using data mining and machine learning to indicate the most acceptable crystal structure.[96] In this study, the accuracy of this model was confirmed by solving the crystal structures of two unreported, novel intermetallic phases ($ZrAu_{0.5}Os_{0.5}$ and $Nd_4Mn_2AuGe_4$). Manually refined single crystal and the SCAR refinement of $ZrAu_{0.5}Os_{0.5}$ are compared in Table 1.1, indicating similar refinement.

Table 1.1. Comparing manually refined and SCAR refinement of $ZrAu_{0.5}Os_{0.5}$

	Manually-Refined	*SCAR*-Refined
Formula	$ZrAu_{0.5(1)}Os_{0.5(1)}$	$ZrAu_{0.5(1)}Os_{0.5(1)}$
Formula mass (g mol^{-1})	284.80	
Space group	$Pm\bar{3}m$ (No. 221)	
a (Å)	3.318(9)	
V (Å^3)	36.5(2)	
Z	1	
ρ_{calc} (g cm^{-3})	12.952	
T (K)	273	
μ(Mo $K\alpha$) (mm^{-1})	100.014	
No. of variables	5 (6)	6
$R(F)$ for $F_o^2 > 2\sigma(F_o^2)$ [a]	0.0258 (0.0254)	0.0253
$R_w(F_o^2)$ [b]	0.0258 (0.0254)	0.0253
Goodness of fit	1.359 (1.357)	1.793
$(\Delta\rho)_{max}$, $(\Delta\rho)_{min}$ (e Å^{-3})	1.369, −1.273	1.364, −1.028

Finally, there is a long history of searching for equiatomic binary intermetallic compounds with the general composition *AB*. In a recent study, the exis tence of a new 1:1 stoichiometric intermetallic compound RhCd along with its crystal structure was first predicted by employing machine learning, following by synthesis.[97] Machine learning was instrumental in the discovery of this new phase because it is the only reported compound in Rh-Cd binary system and had not been reported even though nearly all simple binary phases were presumably discovered.

Over the last three centuries, chemists have endeavored to understand the crystal structure and chemical behavior of intermetallic compounds. Although a massive number of

compounds have been discovered and a dramatic improvement in our fundamental chemical understanding of these systems developed during this time, these achievements have primarily stemmed from serendipitous discovery or extensive trial-and-error synthesis. Nowadays, the ever-increasing industrial demand for these types of phases has made scientists strive to develop more efficient techniques for materials discovery. Indeed, the paradigm has shifted from exploratory synthesis to DFT assisted synthesis and has continued to materials discovery using machine learning.[98] Despite the reliability of each method, their real power is realized when all three techniques are combined. However, the computation and data-driven methodologies are still comparatively in their early stages, and improvements are needed. Firstly, there are intrinsic complexities in real extended solids, such as local structure distortions and structural defects that are not necessarily accounted for in computational models. This is especially true for intermetallics, where the nature of the chemical bond in these metallic systems allows the formation of extremely complex crystal structures. For example, the binary HfIn structure was predicted by both machine learning and CALYPSO to adopt the tetragonal CuAu-type structure.[99] After experimental investigation, the structure of the bulk sample was γ-brass (Cu_5Zn_8-type), which can be viewed as a superstructure of the CsAu-type structure. This discovery was also surprisingly different from the crystals picked from the surface of the product ($CuPt_7$-type). The apparent failure of DFT and machine learning to predict the structure of HfIn highlights the complexity observed in intermetallic compounds. Moreover, while the implementation of machine learning in natural sciences has been dramatically increased during the past years, utilizing machine learning to accelerate materials discovery, chemistry, and materials, science has not necessarily experienced the same progress. This is primarily because the size of the databases available for training is limited, and the data

available tend to be sparse and inconsistent. Therefore, increasing database ability and diversity of crystalline structures will remain an essential and active field indefinitely. Nevertheless, there are ample computational and informatics resources available today that can assist in the identification of new intermetallic compounds. Researchers simply need to find creative ways to merge these approaches with solid-state synthesis to allow the unprecedented discovery of new metal-rich solids.

1.5 Research Goals

The goals of the research presented in this thesis are to discover novel intermetallic phases and understand their captivating crystal structures as well as their complex bonding behavior using a combination of solid-state synthesis, first-principle calculations, and machine-learning. Merging these traditionally disparate research approaches has allowed chemists to understand the intermetallic structure-composition-property relationship better and accelerate solid-state inorganic materials discovery. For example, this research combines the exploratory synthesis of ternary intermetallics in the *RE*-Au-Sn (*RE* = La, Ce, Pr, Nd) phase system with DFT *ab initio* computations to investigate the origin of gold's polyanionic bonding network. In this research, a series of compounds with the general composition of $RE\mathrm{Au}_{1.5}\mathrm{Sn}_{0.5}$ (*RE* = La, Ce, Pr, Nd) were discovered, and their structural preference, as well as the existence of the desired polyanionic bonding network that stabilizes the crystal structure, were confirmed using DFT calculations. This idea has been expanded to the other rare-earth gold ternaries like *RE*-Au-Ge (*RE* = La, Ce, Pr, Nd) ternary phase system, where six novel compositions have been identified experimentally, and their electronic structure was studied using DFT calculation.

This research also goes beyond the experimental identification of crystal structures of intermetallics. Using an *ab initio* approach within the DFT framework coupled with a state-of-the-art structure-search algorithm, thermodynamically stable phases with the general composition A_nIr_m (A = Rb, Cs and n = 1-3, m = 1-3) are studied under the high-pressure. Furthermore, a method is established in this thesis to combine solid-state experimental synthesis, DFT calculation, and machine learning for efficient discovery of intermetallic phases. Here, a machine-learning model is developed to predict the formation energies of compounds with a training set based on the DFT calculation formation energies of compounds compiled in the Materials Project and OQMD databases. This approach screens 313,965 formation energies data and predicts formation energy of 253 compounds per system in the *Tr*-Ag-In (*Tr* = B, Al, Ga, In). The resulting tool allows locating the fruitful areas in the phase diagram, leading to the directed-synthesis of $YAg_{0.65}In_{1.35}$. The success of this work highlights the potential of deploying machine-learning methods that can predict the formation for any new compounds to speed up the discovery of novel materials by directing synthesis efforts.

1.6 Organization of the Thesis

Chapter 1 features a minireview on the discovery of novel intermetallics through synthesis, computation, and data-driven analysis. This section discusses recent research efforts where experimental, computational, and data-driven inorganic chemistry has been used to produce novel intermetallics as well as understand their complex crystal chemistry.

[S. Lotfi, J. Brgoch, Establishing the Complex Crystal Chemistry of Intermetallic Phases through Synthesis and Data-driven Analysis, *Chem.: Eur. J*, **2020** DOI: 10.1002/chem.202000742]

Chapter 2 describes the solid-state experimental, first-principles computational, and machine-learning methods explored in the research presented in this thesis.

Chapter 3 combines experimental synthesis and first-principle computation for a better understanding of gold's polyanionic bonding in the gold-rich polar intermetallic phases. Here, a series of compounds with the general composition of $REAu_{1.5}Sn_{0.5}$ (RE = La, Ce, Pr, Nd) were discovered, and their chemical bonding was examined.

[S. Lotfi, A. Oliynyk, J. Brgoch, Polyanionic Gold–Tin Bonding and Crystal Structure Preference in *RE*$Au_{1.5}Sn_{0.5}$ (*RE* = La, Ce, Pr, Nd), *Inorg. Chem*. **2018**, 57 (17), 10736–10743]

Chapter 4 is a computational approach to investigate the formation of alkali metals Iridides under high-pressure. Using an ab initio approach within the density functional theory framework coupled with the PSO structure-search algorithm reveals the existence of binaries A_3Ir (A = Rb, Cs) above 10 GPa. Further, their electronic structures and chemical bonding was then studied in this research.

[S. Lotfi, J. Brgoch, Predicting Pressure-Stabilized Alkali Metal Iridides: A–Ir (A = Rb, Cs). *Comput. Mater. Sci.* **2019**, 158, 124–129]

Chapter 5 develops a framework to merge machine-learning methodology, first-principle computation, and solid-state experimental synthesis. In this research, a machine-learning model was developed to predict the formation energy of metal-rich solids with 95% accuracy using support vector regression combined with high-throughput DFT computational data. Subsequently, the experimental synthesis based on the predictive model revealed the novel compound in the Y-Ag-In ternary phase with the general composition of $YAg_{0.65}In_{1.35}$.

[S. Lotfi, Z Zhang, G. Viswanathan, K. Fortenberry, A. Mansouri Tehrani, J. Brgoch, Targeting Productive Composition Space through Machine-learning Directed Inorganic Synthesis, *Matter*, accepted, **2020**.]

Chapter 6 investigates the exploratory synthesis in the RE-Au-Ge (RE = La, Ce, Pr, Nd] ternary system. The existence of La_3Au_3Ge, $LaAu_2Ge_2$, and RE_2AuGe_3 (RE = La, Ce, Pr, Nd) composition were confirmed with single-crystal X-ray analysis. Here, the structural preference and electronic structure calculation of La_2AuGe_3 was studied by first-principle computation.

Chapter 7 presents conclusions derived from the research presented in this thesis as well as providing an outlook for future research directions.

Chapter 2

Experimental Techniques, Computational Procedure, and Machine Learning Methods

This chapter includes an overview of the main experimental, computational, and data science techniques used throughout this thesis. More detailed descriptions are included in each of the following chapters.

2.1 Experimental Synthesis

2.1.1 Starting Materials

All starting materials for syntheses (presented in Table 2.1) were used as purchased. Unless specified to the contrary, chemicals were stored in closed containers in ambient conditions in the Brgoch Laboratory. Air sensitive starting materials and compounds were stored in an argon atmosphere glovebox (O_2 < 0.1 ppm; H_2O < 0.1 ppm).

Table 2.1 Starting materials used for all synthesis

Compound	Form	Source	Purity
La	filings	HEFA Rare Earth	99.8%
Ce	filings	HEFA Rare Earth	99.8%
Pr	filings	HEFA Rare Earth	99.8%
Nd	filings	HEFA Rare Earth	99.8%
Au	splatter	Materion Advanced Chemicals	99.999%
Sn	powder	Alfa Aesar	99.985%
Y	filings	HEFA Rare Earth	99.8%
Ag	powder	Alfa Aesar	99.9%
In	pieces	Alfa Aesar	99.99%
B	crystalline pieces	Alfa Aesar	99.5%
Ge	powder	Alfa Aesar	99.999%

2.1.2 Glovebox

Since rare-earth metals are air-sensitive, all product compounds are stored in an argon atmosphere glovebox from MBRAUN. The total O_2 and H_2O content are maintained at less than 0.1 ppm by continuous cycling through a copper-based catalyst. The glovebox is regenerated every eight months, and the level of moisture is monitored regularly by the glovebox sensors as well as performing the classic light bulb test. 5% hydrogen/95% argon gas from Matheson Trigas Company is utilized for the regeneration.

2.1.3 Solid-state synthesis via Arc-Melting

All compounds were first synthesized using arc-melting (Centorr Furnace). Arc-melting is a practical technique for intermetallic synthesis due to its inherent advantages, including high temperature, non-contact method, and extremely fast procedure. However, arc-melting does not always yield high-quality single crystals. Thus, it is essential to anneal the product after arc melting. This also helps ensure that near thermodynamic ground state compounds are obtained. For this process, the starting materials were first weighed out in the desired stoichiometric ratios targeting a total mass of ~0.2 g to 0.3 g. These reagents were pressed (up to 2500 psi) into a 5 mm pellet to promote better contact between the starting elements. This pellet was placed on a water-cooled copper hearth along with a Ti ingot or sponge. To generate an inert atmosphere, the arc-melter chamber was purged with argon gas at least eight times before the melting process started. The Ti was melted before the sample to act as a getter and ensure an oxygen-free environment The samples were all reacted by striking an arc between the thoriated tungsten electrode and the copper hearth using a current of ~35 A to 55 A. To ensure the homogeneity, the sample was flipped over and re-melted at least three times. The weight loss for each sample was measured after arc-melting to determine if the approximate composition remained constant during synthesis.

The arc-melted ingots were sealed in fused silica tubes under vacuum (2×10^{-3} mbar) and annealed within the temperature range of 700-850°C using Lindberg/Blue™ furnaces. Annealing lasted for one week, followed by cooling to warrant near-equilibrium phases are present in the product. All of the furnaces used in this work are programmable with a maximum operating temperature of 1200°C. The temperature is monitored by a K-type thermocouple as well as SiC heating elements (I Squared R

Element Co., Inc.) as the primary source of heating. Lastly, all products were stored in the glovebox for further characterization.

2.2 Characterization

2.2.1 Powder X-ray Diffraction

To confirm the phase purity of all synthesized compounds, they were first characterized by powder X-ray diffraction. Since the majority of compounds are sensitive to moisture and air, the sample preparation for powder diffraction was performed in the glovebox with an inert argon atmosphere. The products were ground using an agate mortar and pestle until small and evenly distributed particles (≈10 μm) were obtained. The homogenous powders were placed on a zero-background silicon stage, ensuring the sample is distributed as evenly as possible. The silicon stage was placed in an aluminum ring and covered with a Kapton film to prevent oxidation of the samples. X-ray powder diffraction analysis was performed using a PANalytical X'Pert Pro powder diffractometer with Cu Kα (λ = 1.54183 Å). The powder diffractogram was obtained by scanning from 10 2θ to 80 2θ in the step size of 0.008° over 14 minutes or 28 minutes. The powder X-ray diffractorgrams were subsequently indexed manually by comparing the collected dataset against known patterns assisted by the software X'pert Highscore Plus 2.2 software loaded with the International Center for Diffraction Data (ICDD) powder diffraction database.[100,101] Lastly, the calculated X-ray pattern from single-crystal measurement was used for Le Bail refinement to confirm phase purity and obtain accurate lattice parameters.[102] Le Bail refinements were performed using the EXPGUI interface for the General Structure Analysis System (GSAS).[103–105] The background was fit with a shifted-Chebyshev function by using seven parameters, and peak shapes were described using a Psuedo-Voigt function.

2.2.2 Single-Crystal X-ray Diffraction

Single-crystal X-ray diffraction is the most useful experimental technique to identify the atomic arrangement and crystal structure of unknown compounds. Due to the air sensitivity of these samples, the well-faceted crystals were picked from crushed samples in the glovebox with the aid of an optical microscope. The idea crystal size is in the size range of 0.1 to 0.01 mm, which is a compromise on maximizing scattering intensity while lowering absorption. The most suitable crystals were floated in Paratone-N oil, and then placed on dual thickness MiTeGen MicroLoops LD, and immediately mounted onto the goniometer under nitrogen flow to minimize oxidation. The single-crystal X-ray diffraction measurement was carried out using a Bruker APEX II platform diffractometer equipped with a 4K CCD APEX II detector, and a Mo Kα radiation source (λ = 0.71073 Å).[106] The data was collected at a 6-cm detector distance by taking four sets of 726 frames with 0.3° scans in ω and an exposure time of 30-50 s per frame at a temperature of 213 K or room temperature. The data were integrated using the Bruker-Nonius SAINT program, with the intensities corrected for Lorentz factor, polarization, air absorption, and absorption due to variation in the path length through the detector faceplate. The absorption correction was applied using TWINABS for twinned crystals or SADABS for one domain crystal based on the entire data sets.[106,107] XPREP program was utilized to carry out for unit cell reduction as well as the determination of possible space groups according to systematic absences and the internal R-value of the data.[108] The crystal structures were subsequently solved by employing direct methods and refined using full-matrix least-squares calculations on F_0^2.[109,110] The atomic positions for all elements were easily identified by using direct methods, and the thermal parameters were considered anisotropically for all crystals. All

crystallographic calculations were performed using the SHELXTL program package (version 6.12).[111]

In the structure solution, the atomic coordinates, atomic displacement parameters, scale, weighting, and extinction factors are refined. The accuracy of the structural solution is evaluated by the residual factors R_1 and wR_2 and goodness of fit where they are calculated by the following equation:

$$R_1 = \frac{\sum \left| |F_o| - |F_c| \right|}{\sum |F_o|} \tag{2.1}$$

$$wR_2 = \sqrt{\frac{\sum w(F_0^2 - F_c^2)^2}{\sum w(F_0^2)}} \tag{2.2}$$

$$GooF = \sqrt{\frac{\sum w(F_0^2 - F_c^2)^2}{n - p}} \tag{2.3}$$

where, F_o is the measured structure amplitude, F_c is the calculated structure amplitude. The weighting factor is defined as $w = (\sigma^2 F_o^2 + a^2 P^2 + b^2 P^2)^{-1}$, where $P = \frac{1}{3} F_o^2 + \frac{2}{3} F_c^2$, n is number of independent reflections, and p is number of refined parameters. The residual values should be as small as possible, while the goodness of fitness value should slightly deviate from one for an acceptable refinement. All the crystal structures visualized in this thesis were created using Visualization for Electronic and Structural Analysis (VESTA) software.[112]

2.2.3 Scanning Electron Microscopy (SEM) and Energy Dispersive X-ray Spectroscopy (EDS)

Scanning electron microscopy (SEM) is a powerful magnification method for analyzing the external morphology of solid specimens. The significant advantage of this electron microscopy over optical microscopy is the high spatial resolution down to tens of angstroms. If the electron dispersive X-ray spectroscopy (EDX) is combined with SEM, the chemical composition can also be determined. A high-resolution image of the surface can be generated by detecting secondary or backscattered electrons emitted as a result of incident beam electrons interacting with the material. Generally, this technique works best for elements with atomic number $Z > 3$. The accuracy of EDX analysis depends on various factors including the nature of sample as well as possible peak overlaps, however, ~2 wt. % for a given element is acceptable. SEM was conducted using a JEOL JSM-6400 to visualize the single crystals and bulk sample at 500X-1200X magnification while electron gun was set to accelerating voltage of 15kV and a constant emission current of 12 μA. The semi-quantitative compositions of the compound were determined by an AMETEK EDAX Octane Pro energy dispersive X-ray spectrometer. Because all the compounds analyzed in this thesis are metals, carbon coating to minimize charging was not required. It is sufficient to stick the single crystals to double-sided carbon tape. The bulk samples were mounted in the epoxy and covered with graphite paste on the surface.

2.3 Electronic Structure Calculation

2.3.1 Vienna *ab initio* Simulation Package (VASP)

Solving the Schrödinger equation is unmanageable for multi-electron systems. A viable alternative is density functional theory (DFT), which suggests valence electrons are primarily responsible for bonding, and core electrons, combined with the nucleus compose an inert core, can be treated as two independent densities by following the Hohenburg-Kohn theorems.[113,114] Using these densities, the wave functions can be approximated by reducing the number of variables from 3N, where N is the number of electrons in a system, to 3 (the *x*, *y*, and *z* directions), simplifying the calculations without sacrificing accuracy.[115,116]

In this work, DFT is implemented within the Vienna *ab initio* Simulation Package (VASP), a computer program, which utilizes pseudopotentials to model exchanges and correlations between the valence electrons and the inert core.[117,118] Throughout this thesis, the projector augmented wave (PAW) pseudopotentials were utilized to improve calculation efficiency while still maintain an accurate description of the valence electrons' behaviors.[119] To simplify calculations and allow for easier convergence, a plane wave basis set with an energy cutoff was utilized to describe the valence electron density. In addition, the exchange-correlation energy was characterized using the generalized gradient approximation (GGA) in the way of Perdew-Burke-Ernzerhof (PBE), which again improves the accuracy of the calculation by better modeling electron-electron correlation.[120,121]

Implementing this method, structure optimizations were performed to determine electronic properties, including bandgap (E_g), the density of states (DOS), and total formation energy ($E_{F,\mathrm{DFT}}$). In this thesis, all the structures have initially been optimized by relaxing all degrees of freedom in the structure, including the cell shape, cell volume, and atomic positions. Also, for accurate calculations of the structure's energetics, total energies are calculated through a static step using the tetrahedron method. Further computational

details, including specific *k*-mesh, energy cut-off ranges, and specific atomic potentials, are presented in the appropriate research chapters.

2.3.2 Particle Swarm Optimization

Particle swarm optimization (PSO) is a stochastic global optimization method, inspired by the collective behavior of social organisms in a group, such as bird flocking, fish schooling, or ant colonies.[46] In PSO, each particle can learn from history and is influenced by its best-achieved positions or the group best position. Thus, the initial position $(x(t))$ and velocity $(v(t))$ of particles are generated randomly. Later, the position of each particle $(x(t+1))$ is generated depending on its former position $(x(t))$ and its velocity $(v(t+1))$. At every step, the position and velocities are calculated according to the Formulae:

$$\big(x(t+1)\big) = x(t) + v(t+1) \tag{2.4}$$

$$v(t+1) = \omega v(t) + c_1 r_1\big(pbest(t) - x(t)\big) + c_2 r_2\big(gbest(t) - x(t)\big) \tag{2.5}$$

Here, ω is inertia weight which can be varied linearly between 0.9 to 0.4; the coefficients c_1 and c_2 are self-confidence factor and swarm confidence factor, respectively; r_1 and r_2 are two random numbers that uniformly varied in the range [0; 1], generated separately for every particle at every step; $pbest(t)$ is considered as best fit of a position (i.e., the lowest enthalpy for individual structure), and $gbest(t)$is the best fit for the entire swarm, as illustrated in Figure 2.1.[122]

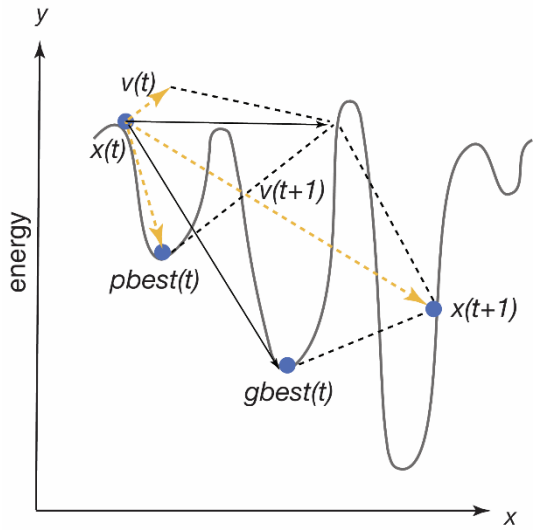

Figure 2.1. The deception of position and velocity updates in particle swarm optimization. The solid grey line approximates a typical energy landscape. Arrows illustrate the velocity at the relative position of a particle. This figure is adapted from reference 24.

In this thesis, the global structure prediction method, particle swarm optimization, as implemented in the Crystal Structure Analysis by Particle Swarm Optimization (CALYPSO) is used.[122,123] This approach employs DFT to optimize CALYPSO generated crystal structures and calculate their total energies. Generally, the CALYPSO process includes four significant steps: (i) random structure generation with the symmetry constraint; (ii) local structural optimization; (iii) post-processing for the identification of unique local minima by bond characterization matrix; (iv) generation of new structures by PSO for iterations. Here, the structure search was carried out on different stoichiometric ratios of the elements, including A_3B, A_2B, AB, AB_2, and AB_3, in a pressure range from 1×10−4 GPa (herein referred to as 0 GPa) to 20 GPa in steps of 5 GPa. Also, the simulation unit cell size was distributed between 2 and 4 formula units (f.u.). Total energy calculations

required for the crystal structure search were performed using DFT within the Vienna *ab initio* Simulation Package (VASP).

2.3.3 Calculating Approximate Structural Thermodynamic Stability

Once the crystal structure of an unknown compound was predicted, the thermodynamical stability of the novel structure can be determined. To compare the phase stability of compositions, the formation energy of each composition should be determined at zero kelvin following Equation 2.6:

$$\Delta H = [H(A_x B_{1-x}) - xH(A) - (1-x)H(B)] \tag{2.6}$$

The convex hull can then be constructed by plotting the formation energy of compounds versus the composition curve. The convex hull distance is calculated as the energy released by decomposing into the stable phases. The structures fall above the hull are thermodynamically unstable, while compositions on the convex hull are considered thermodynamically stable and energetic potential to form. Figure 2.2 indicates the convex hull plot for A-B binary systems, illustrating the blue dots as stable compositions and yellow dots as thermodynamically unstable compounds. To ensure the dynamical stability of a structure, the phonon density of state (phDOS) can be calculated using the PHONOPY package, which employs the modified Parlinski–Li–Kawazoe *ab initio* force constant method.[124,125] Supposing that phDOS indicates imaginary modes, the structure is unstable, even though it is thermodynamically favorable.

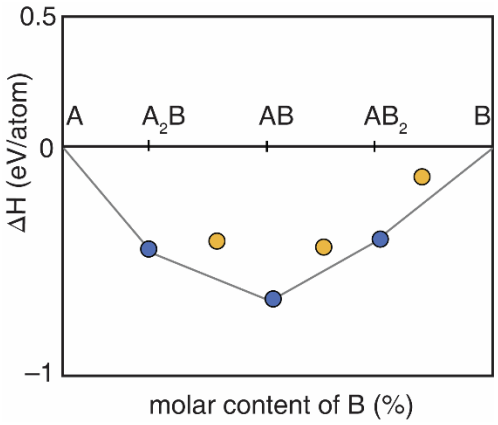

Figure 2.2. The convex hull of binary A-B system. Blue circles show stable compositions on the hull, while the yellow dots are thermodynamically unstable and will decompose to compositions on the convex hull.

2.4 Data-Driven Analysis

2.4.1 Machine Learning Workflow

Data-driven science has been introduced as the 4th paradigm in science, where the first three are empirical, model-based theoretical, and computational science, respectively.[126] Currently, chemistry and materials science have employed informatics, albeit rather later than other natural sciences. The purpose of transition from experiment and computation to machine learning is not just to replace them with predictive models, but rather to alleviate experimental work, resulting in materials accelerated discovery. Machine-learning techniques have provided the ability to rapidly, and often accurately, predict the inorganic compounds preferred crystal structure or physical properties. The general machine-learning procedure is defined as follows: data collection, data representation, and model construction. The first process is required to obtain the known dataset, also called a training set. The data representation, as a set of "features or descriptors set," is required to distinguish the correlations within the data. Lastly, the appropriate predicting model can be

constructed based on the training set and the descriptor set. Herein, the following sections describe the implementation of these procedures that are used in this thesis.

2.4.2 Data Collection

Identifying the appropriate source of the training set is the initial step in the machine-learning approach. The availability of data for a machine-readable format is limited in chemistry and materials science comparing to other research communities such as computer science and biology. The primary reason for insufficient data availability in chemistry is inconsistent formats of literature making extractions laborious. Further, literature more often includes solely successful approaches resulting in a bias. Thus, the organized experimental compiled datasets, such as Crystal Structure Database (ICSD)[79] and Pearson's Crystal Data (PCD), are limited. However, the advance in computational capability has assisted the development of DFT databases like The Materials Project[127], AFLOW[128], and OQMD[75]. In this thesis, the DFT calculated formation energies are extracted from the Materials Project and the OQMD databases and further used as the training set.

2.4.3 Identifying Descriptors

After collecting the set of data, the descriptors (also called features or attributes) need to be developed. In the framework of the inorganic material, there are a variety of descriptors based on property-related compositions, crystal structures, or a combination of both. Physical descriptors are chosen in this thesis, as presented in Table 2.2. In this thesis, there are 35 distinct physical descriptors each further expended to four mathematical expansions, leading to 140 total descriptors. Although there is not a strict rule in choice of descriptors, extreme caution needs to be taken for selecting the descriptors. For example, materials that are very similar (or different) need to characterize very similarly (or different). Another

significant the used descriptor d_i should uniquely characterize the material i.[129] Finally, a set of suitable descriptors should readily available, easily calculable, as well as universal.

Table 2.2. Compositional descriptors used in machine-learning model

Descriptors		Descriptors	
Atomic number	1-4	Number of valence electrons	73–76
Atomic weight	5–8	Gilman number of valence electrons	77–80
Period number	9–12	Number of s electrons	81–84
Group number	13–16	Number of p electrons	85–88
Family number	17–20	Number of d electrons	89–92
Mendeleev number	21–24	Number of outer shell electrons	93–96
Atomic radius	25–28	First ionization energy	97–100
Covalent radius	29–32	Polarizability	101-104
Zunger radius	33–36	Melting point	105–108
Ionic radius	37–40	Boiling point	109-112
Crystal radius	41–44	Density	113-116
Pauling EN	45–48	Specific heat	117-120
Martynov-Batsanov EN	49–52	Heat of fusion	121-124
Gordy EN	53–56	Heat of vaporization	125-128
Mulliken EN	57–60	Thermal conductivity	129-132
Allred-Rochow EN	61–64	Heat atomization	133-136
Metallic valence	65-68	Cohesive energy	137-140
Electron affinity	69-72		

2.4.4 Support Vector Regression (SVR)

Once the descriptor set has been completed, the suitable machine-learning model can be constructed. There are a massive number of machine-learning algorithms available for chemists, including supervised and unsupervised learning. The choice of the machine-learning model relies on the output as well as the number of input data. Given the training dataset, $T = \{(x_i, y_i): i = 1, 2, \dots, N\}$. Where x_i is a multivariate input consisting of all the independent variables, and y_i is the corresponding output, and N is the number of the training dataset. The SVR is defined as a function,

$$y_i = f(x, \omega) = \sum_i^n \omega . \Phi_i(x) + b \tag{2.7}$$

Where ω is the weight vector, $\Phi_i(x)$ is a nonlinear transformation mapping function, and b is a constant threshold. For all the training data, the SVR finds the function that has at most ε deviation from the obtained targets y_i, while being as flat as possible.[81] To seek the flatness, the norm $||\omega||^2 = < \omega, \omega >$ should be minimized, also the slack variables ξ_i, ξ_i^* are introduced to improve the optimizations:

$$\text{Minimize}, \frac{1}{2}||\omega||^2 + C \sum_{i=1}^n (\xi_i + \xi_i^*) \tag{2.8}$$

$$\begin{cases} y_i - F(x_i, \omega) - b \leq \varepsilon + \xi_i \\ F(x_i, \omega) + b - y_i \leq \varepsilon + \xi_i^* \\ \xi_i, \xi_i^* \geq 0 \end{cases} \tag{2.9}$$

where C is defined as a trade-off between the flatness of $\boldsymbol{f}(x)$ and the amount of the allowed deviation, as shown in Figure 2.3. Furthermore, the SVR uses a kernel function to map the

data in high-dimension feature space, such as radius basis function (RBF), which contains a free variable, γ. The optimization of C and γ are carried out using a 10-fold cross-validation (CV) scheme. In 10-fold cross-validation, the model is trained on 9/10 of the data while being tested on the remaining 1/10.

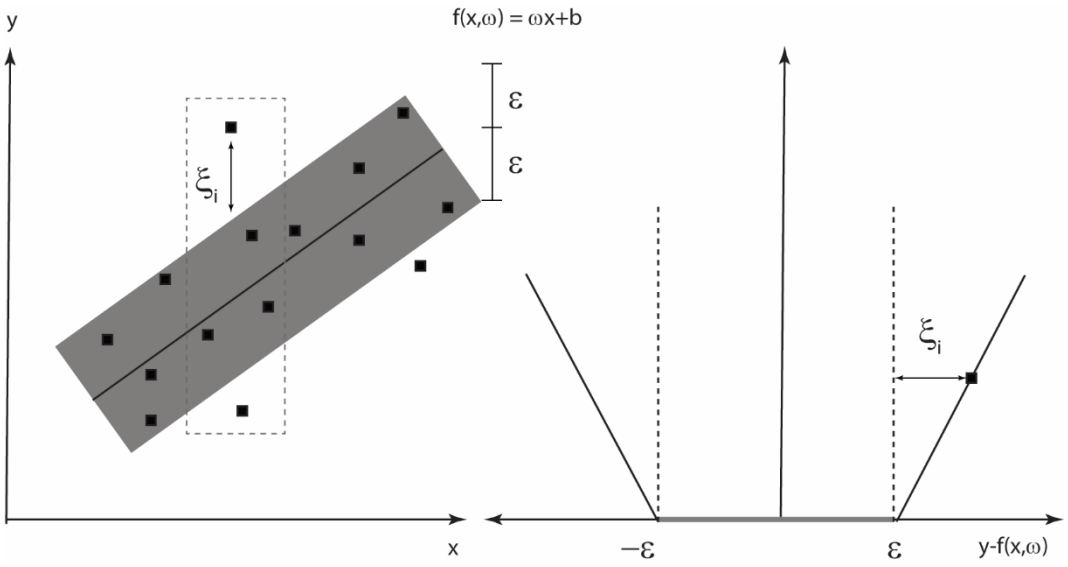

Figure 2.3. A schematic diagram of support vector regression.

Chapter 3

Polyanionic Gold-Tin Bonding and Crystal structure Preference in $RE\text{Au}_{1.5}\text{Sn}_{0.5}$ (*RE* = La, Ce, Pr, Nd)

Reproduced with permission from *Inorganic Chemistry*

(*Inorg. Chem.* 2018, 57, 17, 10736-10743)

DOI: 10.1021/acs.inorgchem.8b01356

Sogol Lotfi, Anton O. Oliynyk, and Jakoah Brgoch*

Department of Chemistry, University of Houston, Houston, Texas 77204, United States

3.1 Introduction

The diverse crystal structures and distinctive bonding patterns of compounds containing gold are often described as Hume-Rothery,[130] Zintl-Klemm,[131,132] or polar intermetallic phases depending on the constituent elements.[6] This simple classification system is governed by the ratio of valence electrons per atom (e/a), where Hume-Rothery compounds are between $1 \leq (e/a) \leq 2$, polar intermetallics fall in the range $2 \leq (e/a) \leq 4$, and Zintl-Klemm compounds have an $(e/a) \geq 4$.[133] Binary gold compounds mostly form Hume-Rothery and polar intermetallic compounds although Au in combination with selected metals from groups 11–14 exclusively adopt Hume-Rothery phases, such as Au_5Zn_8 with 1.6 (e/a) ratio.[134] Increasing the Au content reduces the (e/a) ratio yielding polar intermetallics like $A\text{Au}_2$ (*A* = Na, K) and $AE\text{Au}_2$ (*AE* = Ca, Sr), which tend to contain puckered

hexagonal gold-gold networks.[135,136] Interestingly, a recent investigation of the gold-rich polar intermetallic $NaAu_2$ showed excellent potential as an active catalyst for CO oxidation at a relatively low temperature (400 K) due to the unique chemical bonding in this crystal structure.[137,138]

Binary gold compounds are not readily described by the Zintl-Klemm concept because of electron counting rules; however, some ternary compounds containing gold and electron-rich *p*-block elements can be categorized as Zintl-Klemm compounds. The most prominent gold-based ternary Zintl phase is perhaps Na_2AuBi, which contains planar $[AuBi]^{2-}$ ribbons.[139] Indeed, the combination of gold with *p*-block metals such as In, Sn, and Sb tend to form unique crystal structures with a complex polyanionic backbone. These polyanionic networks have been observed in numerous chemical systems with an array of connectivities including tunnels, diamondoids, and polygonal cages.[140,141] For example, $SrAu_2Sn_2$ adopts the $CaBe_2Ge_2$-type crystal structure which features bonds dominated by Sn–Au interactions forming a $[Au_2Sn_2]^{2-}$ polyanionic network with Sr in a Au_8Sn_8 cage.[142] The EuAuGe-type CaAuSn phase incorporates puckered hexagonal layers of Au and Sn bonds with Au–Au interconnected layers.[143] Gold-rich ternary compounds also tend to show statistical mixing between Au and the main group elements since *p*-block metals such as indium and tin have similar covalent radii to gold. For example, $Ba_2Au_6(Au/T)_3$ (T = In, Sn, Ga) is an example of a gold-rich ternary compound that has Au/T atomic mixing that also features Au–Au bonding.[144] $Ba_2Au_6(Au/T)_3$ adopts trigonal space group $R\bar{3}c$ and also forms hexagonal-diamond-like Au/T bonding.

Although a number of ternary compounds involving alkali or alkaline earth, gold, and *p*-block metals have been discovered, the exploration of the rare-earth *RE*–Au–Sn ternary phase space is limited.[145] In this case, only two ternary phase diagrams, Pr–Au–Sn

and Ce–Au–Sn, have been examined.[146,147] There are also independent reports of *RE*AuSn (*RE* = La–Ho), which crystallizes in space group $P6_3mc$ (No. 186) with the LiGaGe-type structure.[11,148,149] The $[AuSn]^{n-}$ anionic sublattice in this compound features strong polar-covalent bond between Sn–Au and Au–Au, generating a three-dimensional polyanionic backbone. Recently, the compound $RE_3Au_6Sn_5$ (*RE* = La, Ce, Pr, Nd) has been synthesized and found to contain a $[Au_6Sn_5]$ polyanionic network as well as interesting magnetic properties.[150]

In this work, we focus on the synthesis of compounds in the *RE*–Au–Sn (*RE* = La, Ce, Pr, Nd) ternary phase space to further understand the influence and limits of Au in polyanionic bonding networks. In gold-rich polar intermetallic phases, Au often participates in homoatomic bonding; however, the bonding patterns in these compounds are difficult to justify and predict. Exploring the Au-rich region of the *RE*–Au–Sn (*RE* = La, Ce, Pr, Nd) ternary phase space to find polyanionic bonding led us to the existence of $REAu_{1.5}Sn_{0.5}$. Herein, the synthesis and crystal structure of these intermetallic compounds are reported and a topological comparison with binary $REAu_2$ (*RE* = La, Ce, Pr, Nd) is shown.[151,152,153,154] Their structural refinements were performed based on single crystal data, and composition corroborated by SEM-EDX. The chemical bonding networks were then confirmed using DFT calculations on an ordered $LaAu_{1.5}Sn_{0.5}$ model. Finally, the preference for $REAu_{1.5}Sn_{0.5}$ to adopt the observed orthorhombic crystal structure is established. Merging synthetic solid-state chemistry and computational analysis provides a better understanding of gold's chemical behavior when combined with main group elements and rare-earth atoms in polar intermetallics.

3.2 Experimental

3.2.1 Synthesis

The starting metals, gold (99.999%, Materion Advanced Chemical), tin (99.9985%, Alfa Aesar), and the rare-earth elements La, Ce, Pr, and Nd (99.8%, HEFA Rare Earth) were weighted out in the stoichiometric ratio 1 *RE*: 1.5 Au: 0.5 Sn (*RE* = La, Ce, Pr, Nd) with a total weight of 250 mg and pressed into pellets. The samples were first reacted using arc melting (Centorr Furnace). To ensure homogeneity, each sample was melted three times intermittently flipping the button. The weight loss for each sample after arc melting was less than 1%. The arc melted samples were then sealed in fused silica tubes under vacuum (10^{-3} torr) and annealed at 800°C for one week followed by quenching in water. Annealing the samples at different temperatures (700°C and 1000°C) and longer times (up to 3 weeks) did not yield any discernable changes to the product, based on X-ray powder diffraction pattern. The products all had a silver luster, were brittle, and air sensitive. Additionally, the preparation of $LaAu_{2-x}Sn_x$ (x = 0.2, 0.25, 0.35, 0.4, 0.6, 0.65, 0.75, and 0.80) was attempted following the same synthetic procedure; however, the products from these reactions were all multiphase based on powder X-ray diffraction with a substantial number of unindexed peaks, and the single crystal quality was too poor for analysis. Therefore, these compositions were not pursued further. The products were handled and stored in a glovebox with an argon atmosphere (O_2 < 0.1 ppm; H_2O < 0.1 ppm).

3.2.2 Powder X-ray Diffraction

Powder diffraction data were collected using a PanAnalytical X'Pert powder diffractometer and Cu Kα radiation (λ = 1.54183 Å) at room temperature. The samples were prepared for

powder diffraction by grinding the annealed ingots in the glovebox using an agate mortar and pestle and then spreading the fine powder on zero-diffraction silicon plate and covering the sample with Kapton® film. Le Bail refinements were performed to check for phase purity and determine the lattice parameters using the EXPGUI interface for the General Structure Analysis System (GSAS).[103,104] A shifted-Chebyshev function was used to model the background. All crystal structures were visualized using VESTA.[112]

3.2.3 SEM-EDX

Energy-dispersive X-ray spectroscopy (EDX) data were collected on selected crystals and polished bulk samples using a JEOL JSM-6400 scanning electron microscope attached with an AMETEK EDAX Octane Pro energy dispersive X-ray spectrometer and accelerating voltage of 15 eV and an emission current of 12 μA. To avoid the influence of sample tilting for the bulk samples, pieces of the crushed ingots were mounted in epoxy resin and polished using a 1 μm diamond slurry. Selected single crystals were mounted on carbon tape and analyzed by SEM-EDX. In both cases, at least ten independent data points were analyzed on different areas of each compound to determine the average composition.

3.2.4 Single-Crystal X-ray Diffraction

Single crystals were picked from crushed ingots using an optical microscope. The data were collected using a Bruker APEX II platform diffractometer equipped with a 4K CCD APEX II detector and a Mo Kα radiation source. Reflections were collected by taking 4 sets of 726 frames with 0.3° scans in ω and an exposure time of 50 s per frame at a temperature of 213 K. The data were scaled, and an absorption correction was applied using TWINABS.[107] Structure solution and refinement were carried out using the SHELXTL program package (version 6.12),[155] and refined by full-matrix least-squares on F_0^2 including anisotropic

displacement parameters. All crystals were determined to be twins and were therefore integrated as twin crystals with the aid of Bruker-Nonius SAINT. The single crystal data were then solved and refined with two domains. The final crystal structure solutions, in CIF format, have been sent to The Cambridge Crystallographic Data Centre (CCDS), and can be obtained from the CCDC using the depository numbers: CCDC-1840651 (*RE* = La), CCDC-1840655 (*RE* = Ce), CCDC-1841059 (*RE* = Pr), CCDC-1840654 (*RE* = Nd).

3.2.5 Electronic and Chemical Bonding Calculations

First principles calculations on ordered models of $LaAu_{1.5}Sn_{0.5}$ including total energy calculations and chemical bonding analyses were performed using the Vienna *ab initio* simulation package (VASP).[117,118] The calculations employed a plane-wave basis set with projector augmented wave (PAW) potentials,[119] a cutoff energy of 500 eV, a 4×2×2 Γ-centered Monkhorst–Pack *k*-point grid, and a convergence criteria of 1×10^{-8} eV and 1×10^{-6} eV was set for electronic and structure relaxation, respectively. The chemical bonding of $LaAu_{1.5}Sn_{0.5}$ was calculated based on the crystal orbital Hamilton population (–COHP) using the Local-Orbital Basis Suite toward Electronic Structure (LOBSTER).[156,157] The phonon density of states (phDOS) was calculated using the PHONOPY package, which implements the ab initio force constant method[125,124] on 2 × 1 × 1 supercells. The valence electron localization function (ELF), as implemented in VASP,[158,159,160] and Bader charge analysis[161] were used to examine charge redistribution and bonding in the crystal structure.

3.3 Results and Discussion

3.3.1 Crystal structure solution

Preparing $LaAu_{1.5}Sn_{0.5}$, $CeAu_{1.5}Sn_{0.5}$, $PrAu_{1.5}Sn_{0.5}$, and $NdAu_{1.5}Sn_{0.5}$ by arc melting mixtures of the elemental metals produced a poorly crystalline product. Subsequent annealing of the samples at 800°C produced a crystalline product with the resulting diffractogram for $LaAu_{1.5}Sn_{0.5}$ shown in Figure 3.1. The powder diffractograms for the other compositions are shown in Figure S3.1-S3.3. Comparing these data against the compounds complied in the Inorganic Crystal Structure Database (ICSD) did not reveal any possible matches.[79] The products were therefore analyzed using SEM-EDX data on polished surfaces of the crushed ingots to confirm homogenous distribution of the elements and show that no trace impurity elements, such as silicon, were picked up during synthesis (Figure S3.4). A semi-quantitative EDX analysis of the bulk samples indicates the compositions are $La_{1.06(4)}Au_{1.47(6)}Sn_{0.46(6)}$, $Ce_{1.06(4)}Au_{1.49(4)}Sn_{0.45(4)}$, $Pr_{1.04(5)}Au_{1.47(5)}Sn_{0.46(4)}$, and $Nd_{0.99(4)}Au_{1.51(4)}Sn_{0.48(4)}$ agreeing with the nominally loaded composition.

From the crushed bulk ingots, small (≈20 μm) single crystals were selected using an optical microscope. The crystals of $REAu_{1.5}Sn_{0.5}$ (*RE* = La, Ce, Pr, Nd) measured using single crystal X-ray diffraction all appeared to be twinned based on the reciprocal lattice intensities and the single crystal X-ray diffraction patterns. The existence of multi-domains in non-merohedral twinned crystals were further confirmed using "CELL_NOW"[162] and corrected and detwinned with the TWINABS program. The single crystal could then be refined with the resulting crystallographic data for all four compounds given in Table 3.1, 3.2 and the atomic positions and equivalent isotropic displacement parameters provided in Table 3.3. Based on systematic absences, the data set showed a body-centered

orthorhombic lattice with two possibilities, *Imma* or *Ima2*; however, intensity statistics for $NdAu_{1.5}Sn_{0.5}$ (<E^2 – 1>) gave a clear indication of a centrosymmetric space group. The other compositions (*RE* = La, Ce, Pr) were refined using both space groups with the centrosymmetric structure refinement always yielding the best statistics. All four compounds were thus solved in space group *Imma* (No. 74, Z = 4) with the $CeCu_2$-type structure. Interestingly, this is the same space group as the binary $REAu_2$ (*RE* = La, Ce, Pr). Since tin has a larger covalent radius than gold (r_{Au} = 1.34 Å, r_{Sn}= 1.40 Å),[163] the unit cell parameters for $REAu_{1.5}Sn_{0.5}$ from single crystal X-ray diffraction are slightly larger than $REAu_2$. For example, comparing $LaAu_{1.5}Sn_{0.5}$, which has Sn substituted into the structure of $LaAu_2$ increases the a lattice parameter by 1.2%, the b lattice parameter by 2.2%, and c increases 0.5%. The only exception is the c lattice parameter of *RE* = Pr. The single crystal data was then refined for the site occupancies by mixing Au and Sn on a single crystallographic site (Wyckoff 8*h* site) for all the compounds. Mixing on the 8*h* site was required to correctly describe electron density at the position, which also led to the expected composition. Finally, with the crystal structure solved, a Le Bail refinement of the powder X-ray diffraction patterns revealed the major phase is indeed $REAu_{1.5}Sn_{0.5}$ (*RE* = La, Ce, Pr, Nd) with slight impurities of $REAu_2$ as well as a third unidentified phase. All four compounds have similar lattice parameters and unit cell volumes due to the minor differences of the rare-earth atom sizes, as expected.

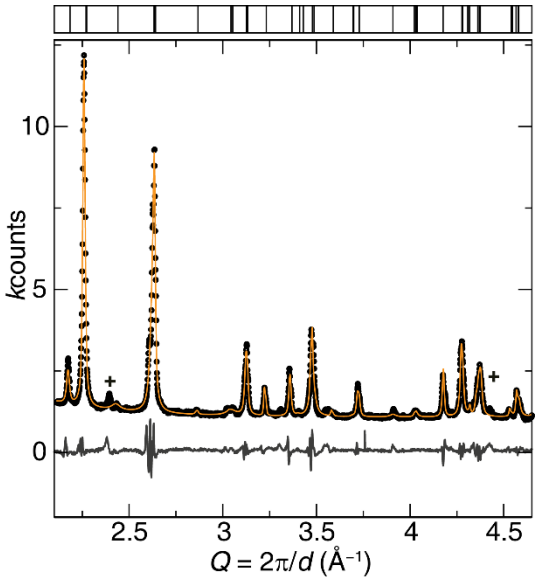

Figure 3.1. Le Bail refinement of X-ray powder diffractogram of $LaAu_{1.5}Sn_{0.5}$. The measured data are shown in black, the fit by the gold line, and the difference between the data and the fit by the gray line. The + indicates the presence of minor unindexed peaks.

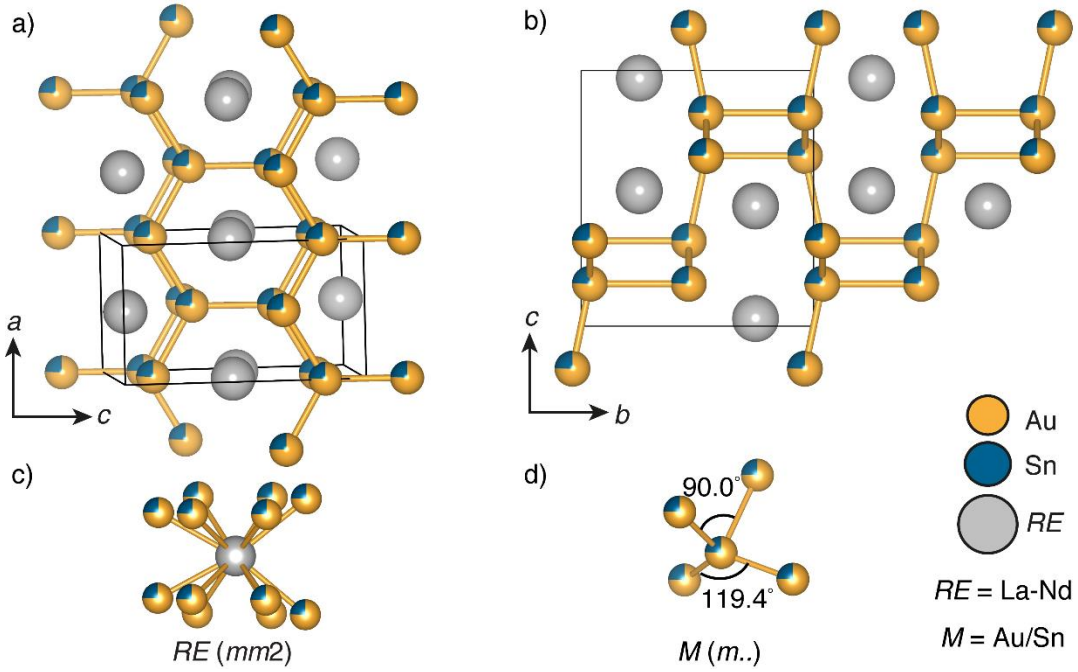

Figure 3.2. a) View of the $REAu_{1.5}Sn_{0.5}$ structure nearly along the *b* axis. b) Stacking along the *a* axis. c) Coordination of *RE* (*RE* = La-Nd) and d) *M* (*M* = Au/Sn) with their site symmetry. Gold, tin, and rare-earth are drawn as yellow, blue, and grey, respectively.

Table 3.1. Crystallographic data for REAu$_{1.5}$Sn$_{0.5}$ (RE = La, Ce) collected at 213 K

Refined formula	LaAu$_{1.50(1)}$Sn$_{0.50(1)}$	CeAu$_{1.48(1)}$Sn$_{0.52(1)}$
Formula mass (g mol^{-1})	493.70	494.91
space group; Z	*Imma* (No. 74); 4	
a (Å)	4.7579(4)	4.7375(7)
b (Å)	7.4546(6)	7.3088(1)
c (Å)	8.1911(7)	8.1890(1)
V (Å^3)	290.52(4)	283.55(7)
ρ_{calc} (g cm^{-3})	11.29	11.60
absorption correction	empirical	
radiation	graphite monochromated; Mo Kα, λ = 0.7107 Å	
μ (mm^{-1})	93.906	97.204
θ range (deg.)	3.70-27.50	3.74-27.46
hkl ranges	0≤ h≤6, 0≤ k≤9, 0≤ l≤10	0≤ h≤6, 0≤ k≤9, 0≤ l≤10
No. reflections; R_{int}	3033; 0.0420	1261;0.0501
No. unique reflections	274	288
No. parameters	13	13
$R(F)$ for $F_o^2 > 2\sigma(F_o^2)$ [a]	0.0273	0.0299
$R_w(F_o^2)$ [b]	0.0651	0.0760
Goodness of fit	1.12	1.15
$(\Delta\rho)_{max}$, $(\Delta\rho)_{min}$ (e Å^{-3})	3.83, –1.83	2.12, –2.05
twin angle, matrix	180, [1 0 $\bar{1}$]	180, [1 0 $\bar{1}$]
BASF value	0.42	0.26

.

Table 3.2. Crystallographic data for REAu$_{1.5}$Sn$_{0.5}$ (RE = Pr, Nd) collected at 213 K

Refined formula	$PrAu_{1.54(2)}Sn_{0.46(2)}$	$NdAu_{1.52(1)}Sn_{0.48(1)}$
Formula mass (g mol^{-1})	495.70	499.81
space group; Z	*Imma* (No. 74); 4	
a (Å)	4.718(3)	4.7143(5)
b (Å)	7.279(4)	7.2444(8)
c (Å)	8.164(4)	8.1586(9)
V (Å^3)	280.4(3)	278.63(5)
ρ_{calc} (g cm^{-3})	11.74	11.91
absorption correction	empirical	
radiation	graphite monochromated; Mo Kα, λ = 0.7107 Å	
μ (mm^{-1})	99.447	101.896
θ range (deg.)	3.75-27.44	3.76-27.54
hkl ranges	$0 \leq h \leq 6$, $0 \leq k \leq 9$, $0 \leq l \leq 10$	$0 \leq h \leq 6$, $0 \leq k \leq 9$, $0 \leq l \leq 10$
No. reflections; R_{int}	2002; 0.0480	4342; 0.0505
No. unique reflections	271	277
No. parameters	13	13
$R(F)$ for $F_o^2 > 2\sigma(F_o^2)$ [a]	0.0370	0.0259
$R_w(F_o^2)$ [b]	0.0883	0.0633
Goodness of fit	1.15	1.10
$(\Delta\rho)_{max}$, $(\Delta\rho)_{min}$ (e Å^{-3})	3.58, – 3.21	1.17, –2.63
twin angle, matrix	180, [1 0 $\bar{1}$]	180, [1 0 $\bar{1}$]
BASF value	0.36	0.45

Table 3.3. Refined atomic coordinates and equivalent isotropic displacement parameters for REAu$_{1.5}$Sn$_{0.5}$ (RE = La, Ce, Pr, Nd)

Compound	atom	Wyck. site	Occ.	x	y	z	U_{eq} (Å^2)[a]
(a) LaAu$_{1.5}$Sn$_{0.5}$							
	La	4*e*	1	0	1/4	0.5299(2)	0.016(1)
	Au	8*h*	0.75(1)	0	0.0375(1)	0.1659(1)	0.012(1)
	Sn	8*h*	0.25(1)	0	0.0375(1)	0.1659(1)	0.012(1)
(b) CeAu$_{1.5}$Sn$_{0.5}$							
	Ce	4*e*	1	0	1/4	0.5294(2)	0.018(1)
	Au	8*h*	0.74(1)	0	0.0353(1)	0.1657(1)	0.014(1)
	Sn	8*h*	0.26(1)	0	0.0353(1)	0.1657(1)	0.014(1)
(c) PrAu$_{1.5}$Sn$_{0.5}$							
	Pr	4*e*	1	0	1/4	0.5284(3)	0.017(1)
	Au	8*h*	0.77(2)	0	0.0356(1)	0.1659(1)	0.012(1)
	Sn	8*h*	0.23(2)	0	0.0356(1)	0.1659(1)	0.012(1)
(d) NdAu$_{1.5}$Sn$_{0.5}$							
	Nd	4*e*	1	0	1/4	0.5283(2)	0.018(1)
	Au	8*h*	0.76(1)	0	0.0341(1)	0.1659(1)	0.014(1)
	Sn	8*h*	0.24(1)	0	0.0341(1)	0.1659(1)	0.014(1)

[a] U_{eq} is defined as one-third of the trace of the orthogonalized U_{ij} tensor.

Table 3.4. Selected bond length [Å] for *RE*$Au_{1.5}Sn_{0.5}$ (*RE* = La, Ce, Pr, Nd)

$LaAu_{1.5}Sn_{0.5}$		$CeAu_{1.5}Sn_{0.5}$		$PrAu_{1.5}Sn_{0.5}$		$NdAu_{1.5}Sn_{0.5}$	
La−*M*[a]	3.2773(9)	Ce−*M*	3.253(1)	Pr−*M*	3.243(2)	Nd−*M*	3.234 (1)
La−*M*	3.287(1)	Ce−*M*	3.2599(8)	Pr−*M*	3.248(2)	Nd−*M*	3.2422(8)
La−*M*	3.376(2)	Ce−*M*	3.3470(7)	Pr−*M*	3.339(2)	Nd−*M*	3.3250(7)
La−*M*	3.3904(7)	Ce−*M*	3.367(2)	Pr−*M*	3.345(3)	Nd−*M*	3.344(1)
La−La	3.7592(5)	Ce−Ce	3.6861(6)	Pr−Pr	3.669(2)	Nd−Nd	3.651(5)
M−*M*	2.7489(8)	*M*−*M*	2.7420(8)	*M*−*M*	2.729(2)	*M*−*M*	2.7271(7)
M−*M*	2.775(2)	*M*−*M*	2.762(1)	*M*−*M*	2.760(3)	*M*−*M*	2.753(1)
M−*M*	3.168(2)	*M*−*M*	3.139(2)	*M*−*M*	3.120 (3)	*M*−*M*	3.127(2)

[a]*M* = Au/Sn

Illustrating the refined crystal structure provides an overview of *RE*$Au_{1.5}Sn_{0.5}$ (*RE* = La, Ce, Pr, Nd). Looking along the *b* direction (Figure 3.2a) shows hexagonal tunnels formed by the polyanionic *M*-*M* (*M* = Au/Sn) interactions stemming from the layers of 6-membered rings. This type of Au–Sn polyanionic bonding was also observed recently in the related LaAuSn system.[11] Based on the crystal structure's symmetry and refined occupancies, there does not appear to be a Au/Sn site preference in *RE*$Au_{1.5}Sn_{0.5}$, which contrasts with LaAuSn where the anions form a fully ordered, alternating Sn–Au polyanionic bonding network. Examining *RE*$Au_{1.5}Sn_{0.5}$ along the *a* direction shows the hexagonal channels are actually puckered rings that are stacked along the *b* direction (Figure 3.2b). This stacking allows for interlayer *M*–*M* (*M* = Au/Sn) contacts to stabilize the anionic hexagonal tunnels. The coordination environments around the rare-earth atoms are a 12-coordiated distorted

hexagonal prism environment with site symmetry *mm*2 (Figure 3.2c). The effective coordination polyhedron for the *M* (Au/Sn) atoms corresponds to a distorted tetrahedron with site symmetry *m*.. (Figure 3.2d).

Examining the crystal chemistry of these compounds by comparing selected bond lengths (Table 3.4) shows the *RE*–*M* bond lengths decrease going from $LaAu_{1.5}Sn_{0.5}$ to $NdAu_{1.5}Sn_{0.5}$, which is consistent with the slight reduction in unit cell volume following the decrease in rare-earth size. The gold-tin contacts are also of interest because in gold containing compounds, the bonding tends to be rather covalent in nature resulting in surprisingly short (for heavy metals) bond lengths. In fact, the *M*–*M* bond lengths in these compounds are ≈2.75 Å making them shorter than the 2.88 Å distance in elemental Au and in agreement with other Au–Sn containing compounds, where the interatomic distances generally range from 2.7-2.8 Å.[164] Finally, the *RE*–*RE* contacts are in the range from 3.6514(5) Å to 3.7593(5) Å, which broadly correspond to the sums of covalent radii of the rare-earth atoms.

3.3.2 Crystal Structure Preference, Electronic structure, and Chemical Bonding in $LaAu_{1.5}Sn_{0.5}$

To understand the crystal chemistry of *RE*$Au_{1.5}Sn_{0.5}$, electronic structure calculations were employed. Knowing that DFT fails at calculating the highly correlated 4*f* electrons present in $CeAu_{1.5}Sn_{0.5}$, $PrAu_{1.5}Sn_{0.5}$, and $NdAu_{1.5}Sn_{0.5}$, electronic structure calculations were focused on $LaAu_{1.5}Sn_{0.5}$. Because the $LaAu_{1.5}Sn_{0.5}$ crystal structure contains a statistically mixed Au/Sn position, ordered models where the Wyckoff 8*h* site is split to contain two Sn atoms and six Au atoms, were created. The possible combinations of placing the two Sn atoms on this originally 8-fold site were then enumerated using "Supercell"[165] generating seven separate

ordered crystal structures (Table S3.1, and Table S3.2). These structural models were each optimized using DFT and the relative total energies (Figure S3.5) calculated to obtain the most favorable distribution of Au and Sn in the structure. The lowest energy structures always contained alternating Sn-Au-Sn contacts, although the energy difference between the models was always <16 meV/atom, supporting the observation of statistical mixing from single-crystal X-ray diffraction.

The lowest DFT energy structural model was then applied to understand the preference for $LaAu_{1.5}Sn_{0.5}$ to adopt the observed orthorhombic crystal structure. Experimentally, it is known that $LaAu_2$ crystallizes in space group *Imma*. Substituting 25 mol% of Sn for Au, forming $LaAu_{1.5}Sn_{0.5}$, shows the compounds remain isostructural; however, increasing the content of tin to 50 mol%, *i.e.*, LaAuSn, causes the crystal structure to change to $P6_3mc$ (LiGaGe-type structure), and the tin and gold order. The origin of this structural change was probed using DFT to calculate formation energy of all three compositions ($LaAu_2$, $LaAu_{1.5}Sn_{0.5}$, and LaAuSn) in both the orthorhombic and hexagonal unit cells. As shown in Table 4, $LaAu_2$ is unexpectedly predicted to slightly (19 meV/atom) prefer the hexagonal space group, which contrasts with the reported crystal structure. Because the energy difference is small, it is possible the structure preference changes at an elevated temperature. Thus, the Helmholtz free energy was also calculated for $LaAu_2$ in both crystal structures. The phonon density of states shows $LaAu_2$ is dynamically stable, *i.e.*, no imaginary phonon modes, in both structure types. The difference in Helmholtz free energy of orthorhombic and hexagonal (Figure S3.6) reveals a switch in the structure preference with the orthorhombic space group becoming more favorable at elevated temperature. Considering $LaAu_2$ was synthesized at 800°C followed by quenching in water the resultant orthorhombic group has a considerably lower free energy compared to an orthorhombic

model of LaAuSn, and has imaginary phonon modes, supporting the experimentally reported hexagonal crystal structure (Figure S3.7).[11] Finally, total energy calculations on $LaAu_{1.5}Sn_{0.5}$ in both space groups confirms the orthorhombic structure type is indeed more energetically favorable, consistent with the crystal structure reported in this work. $LaAu_{1.5}Sn_{0.5}$ in the hexagonal structure also has imaginary phonon modes (Figure S3.8) further bolstering the refinement of an orthorhombic crystal structure.

Table 3.5. The crystal structure preference for $LaAu_{2-x}Sn_x$ (x = 0, 0.5, 1) is determined by calculating the relative total energy of each compound in the orthorhombic (*Imma*) and hexagonal ($P6_3mc$) crystal structures

Compound	E_{ortho} (eV)/atom	E_{hex} (eV)/atom	$\Delta E_{ortho-hex}$ (eV)/atom
$LaAu_2$	–4.600	–4.619	0.019
$LaAu_{1.5}Sn_{0.5}$	–4.711	–4.687 (*i*)[a]	–0.024
LaAuSn	–4.715 (*i*)	–4.859	0.144

[a] (*i*) is defined as existence of imaginary modes in phDOS

Examining the density of states (DOS) for $LaAu_{1.5}Sn_{0.5}$ in the orthorhombic unit cell, illustrated in Figure 3.3a, shows continuous bands across the Fermi level (E_F) indicating metallic nature for $LaAu_{1.5}Sn_{0.5}$. Decomposing the total DOS into its component orbitals show the Au 5*d* orbitals are mainly populated in the range of –6 to –2 eV, similar to most Au-rich polar intermetallic compounds,[33] whereas the *s* and *p* orbitals of Au and Sn are spread across the entire energy range examined. The La orbitals tend to fall primarily above the Fermi level as expected for the most electropositive element in the compound. Using

these electronic structure calculations, the covalent-like chemical bonding can also be extracted based on –COHP analyses using LOBSTER. As plotted in Figure 3.3b, the Au–Au and Au–Sn interactions are over bonded with all bonding orbitals (positive in the plot) full and a number of occupied antibonding orbitals (negative in the plot) falling below E_f. Nevertheless, these contacts show a net positive interaction based on the integrated crystal orbital Hamilton populations (–ICOHP). In fact, the Au–Au contacts are 0.882 eV/bond while Au–Sn is 1.353 eV/bond implying both are a net bonding interaction while the latter is a ≈35% stronger interaction. The La–Au and La–Sn interactions were also calculated and show the La–Sn bonding (1.684 eV/bond) is larger than La–Au (0.909 eV/bond) interaction.

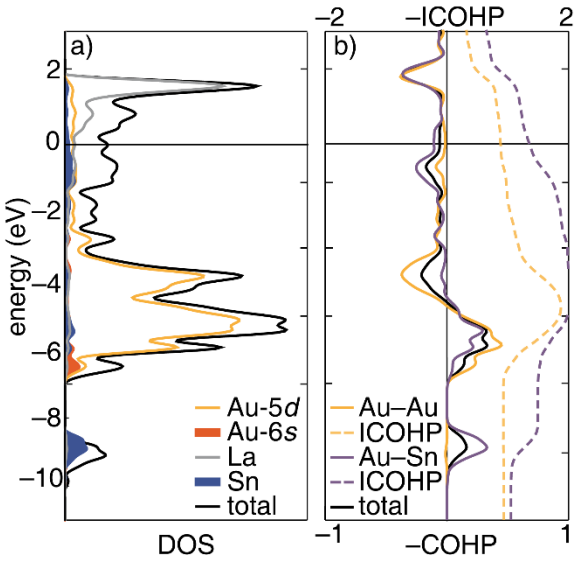

Figure 3.3. a) Calculated density of states (DOS) for $LaAu_{1.5}Sn_{0.5}$. The total DOS is shown by the black line, while the partial DOS is shown for the Au 5*d* states (yellow), the Au 6*s* states (red), the La states (grey), and the Sn states (blue). b) Crystal orbital Hamilton population (–COHP) curves plotting the total average of anionic sublattice interaction (black lines), the average Au–Au interactions (yellow), and the average Au–Sn interactions (purple). The dashed lines are –ICOHP curves for Au–Au (yellow) and Au–Sn (purple) interactions. The positive direction on the abscissa are bonding interactions whereas negative values are antibonding interactions. The Fermi level is set to 0 eV.

Visualizing the atomic interactions in this crystal structure was further achieved by calculating valence ELF. Because even a qualitative interpretations of ELF is relative, the calculations were also conducted for $LaAu_2$ (orthorhombic), $LaAu_{1.5}Sn_{0.5}$ (orthorhombic), and LaAuSn (hexagonal) to identify how the interactions evolve upon adding Sn.[166,167] The ELF plot of $LaAu_2$ (Figure 3.4a) for the (010) plane shows minimal localization between the Au atoms. Substituting Sn for Au in the $LaAu_{1.5}Sn_{0.5}$ causes a redistribution of the electron probabilities in the hexagon network, as illustrated in Figure 3.4b, with a significant increase in the localization of electrons on the (010) plane around the Sn atoms and between the Au–Sn contacts. Inserting more tin when modeling LaAuSn (Figure 3.4c) further enhances the electron localization around Sn. Based on these calculations, the interactions in the anionic sublattice are improved by replacing gold with the tin in the hexagonal bonding network based on the greater localization between Au and Sn.

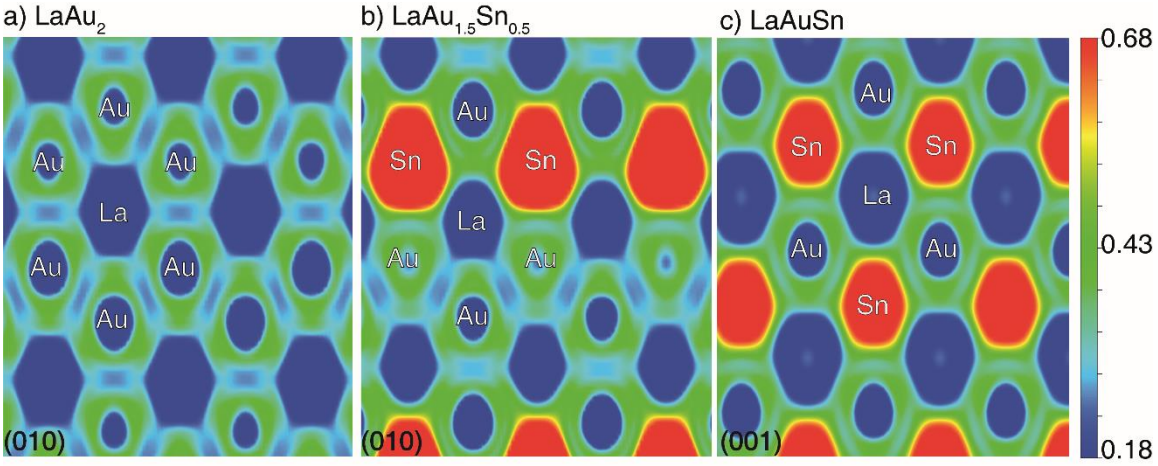

Figure 3.4. a) ELF of $LaAu_2$ near the (010) plane. b) ELF of $LaAu_{1.5}Sn_{0.5}$ near the (010) plane. c) ELF of LaAuSn near the (001) plane. The approximate positions of the La, Au, and Sn atoms are shown for clarity.

COHP and ELF analyses both provide convincing evidence of minimal covalent interactions for $LaAu_{1.5}Sn_{0.5}$. Bader's quantum mechanics atom-in-molecule (QM-AIM) charge analysis was also calculated for $LaAu_2$, $LaAu_{1.5}Sn_{0.5}$, and LaAuSn to approximate the electronic charge on each atom. These results show that $LaAu_2$ has an average charge of +1.59 *e* per La, and –0.79 *e* per gold, whereas $LaAu_{1.5}Sn_{0.5}$ has the average charge of +1.52 *e* per La, –0.94 *e* per Au, and –0.19 *e* per Sn. As tin begins to preferentially occupy a crystallographic site, the negative charge on Au and Sn increase with an average charge of +1.43 *e* per La, –1.13 *e* per Au, and –0.30 *e* per Sn in LaAuSn. These results confirm that $LaAu_2$ contains greatest charge transfer from cation to anion as indicated by the QT-AIM charge on La, *i.e.,* La is the most positive, suggesting $LaAu_2$ is the most ionic in nature. Increasing Sn causes less charge transfer signified by the lower charge on La, suggesting more covalent-like interactions. These calculations emphasize the presence of strong interaction in anionic sublattice for all three compounds, where the electropositive rare-earth atoms donate their electrons to the electronegative $[Au_{2-x}Sn_x]$ polyanionic network.

3.4 Conclusion

The exploratory synthesis in the *RE*–Au–Sn phase space resulted in the discovery of four ternary compounds with the general composition $REAu_{1.5}Sn_{0.5}$ (*RE*= La, Ce, Pr, Nd). The crystal structures were analyzed and solved using single crystal X-ray diffraction analysis and SEM-EDX. $REAu_{1.5}Sn_{0.5}$ (*RE*= La, Ce, Pr, Nd) crystallizes in space group *Imma*, isostructural with $CeCu_2$ and contains a $[Au_{1.5}Sn_{0.5}]$ polyanionic bonding network. Electronic structure and chemical bonding calculations on $LaAu_{1.5}Sn_{0.5}$ reveal the compounds metallic nature and supports the presence of an anionic backbone (Au–Au, Sn–Au). These results support that in systems where gold is combined with electropositive rare-earth metals and

main group elements, like in *RE*–Au–Sn ternary phase space, there is potential to have complex intermetallic bonding including the presence of polyanionic bonding.

3.5 Acknowledgements

The authors thank Prof. Arnold M. Guloy and Dr. James D. Korp for helpful discussions. The authors gratefully acknowledge the generous financial support provided by the National Science Foundation through No. NSF-CMMI 15-62142 and the donors of the American Chemical Society Petroleum Research Fund (55625-DNI10) for supporting this research. AOO gratefully acknowledges the Eby Nell McElrath Postdoctoral Fellowship at the University of Houston for financial support. This research used the Maxwell/Opuntia/Sabine Cluster operated by the University of Houston and the Center for Advanced Computing and Data Systems. Support for this work was also provided by resources of the uHPC cluster managed by the University of Houston and acquired through NSF Award Number 15-31814.

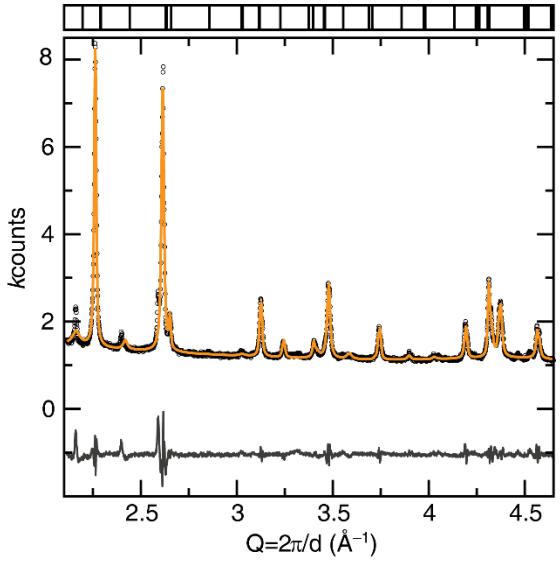

Figure S3.1. Le Bail refinement of X-ray powder diffraction data of $CeAu_{1.5}Sn_{0.5}$. The measured data are shown in black, the fit by the gold line, and the difference between the data and the fit by the gray line.

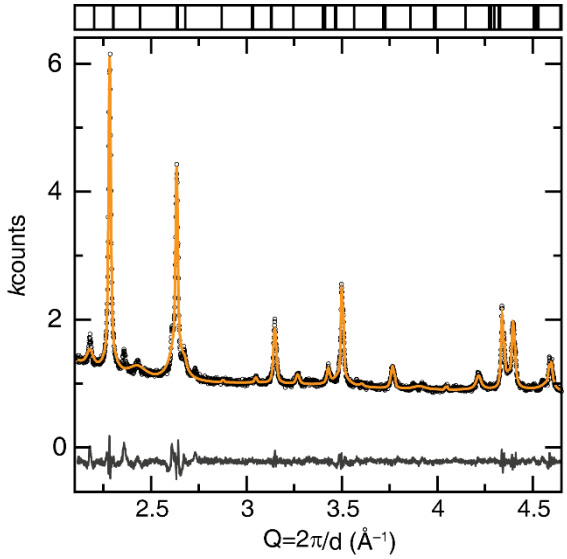

Figure S3.2. Le Bail refinement of X-ray powder diffraction data of $PrAu_{1.5}Sn_{0.5}$. The measured data are shown in black, the fit by the gold line, and the difference between the data and the fit by the gray line.

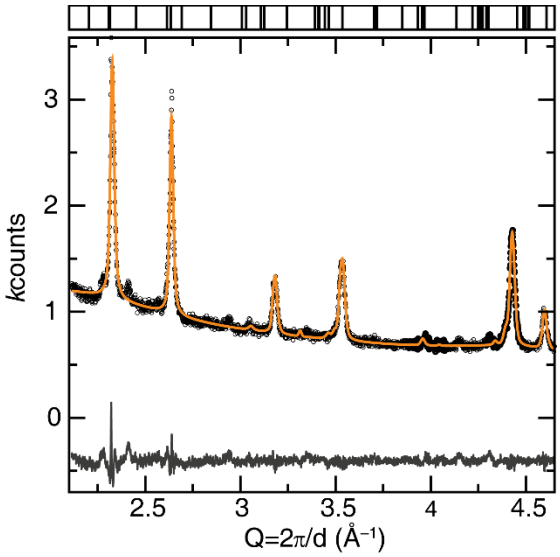

Figure S3.3. Le Bail refinement of X-ray powder diffraction data of $NdAu_{1.5}Sn_{0.5}$. The measured data are shown in black, the fit by the gold line, and the difference between the data and the fit by the gray line.

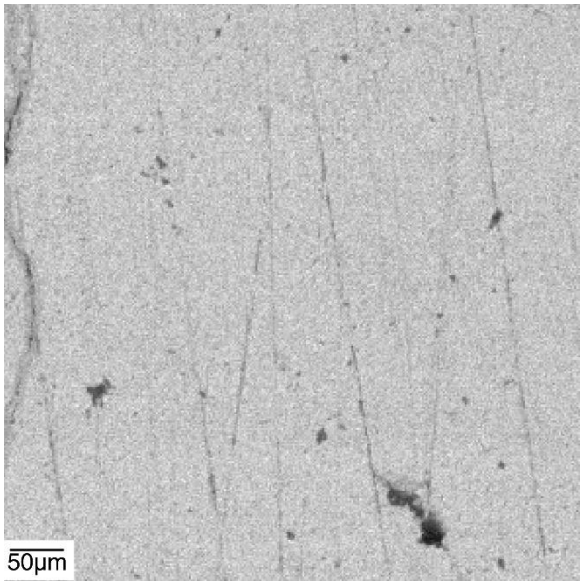

Figure S3.4. SEM-EDX analysis on the bulk sample of $LaAu_{1.5}Sn_{0.5}$

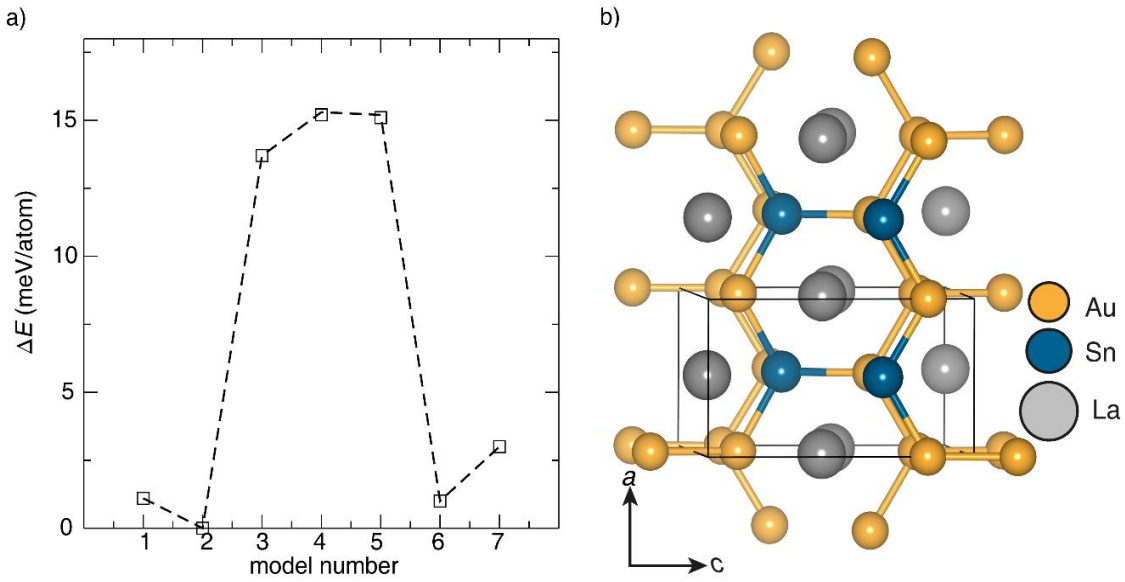

Figure S3.5. a) The ΔE of seven ordered crystal structures generated by Supercell. b) the lowest energy ordered crystal structure.

Table S3.1. Optimize- crystal structure $LaAu_{1.5}Sn_{0.5}$

	Cal. $LaAu_{1.5}Sn_{0.5}$	Exp. $LaAu_{1.5}Sn_{0.5}$	Difference %
a (Å)	4.753	4.758	−0.10%
b (Å)	7.685	7.455	3.08%
c (Å)	8.308	8.191	1.43%
V (Å^3)	303.515	290.520	4.47%

Table S3.2. Atomic coordinates for $LaAu_{1.5}Sn_{0.5}$

	x	y	z
Au	0	0.037	0.166
Au	0	0.463	0.166
Au	0	0.537	0.834
Au	0	0.96251	0.834
Au	1/2	0.537	0.666
Au	1/2	0.037	0.334
Sn	1/2	0.963	0.666
Sn	1/2	0.463	0.334
La	0	1/4	0.530
La	0	3/4	0.470
La	1/2	3/4	0.03
La	1/2	1/4	0.97

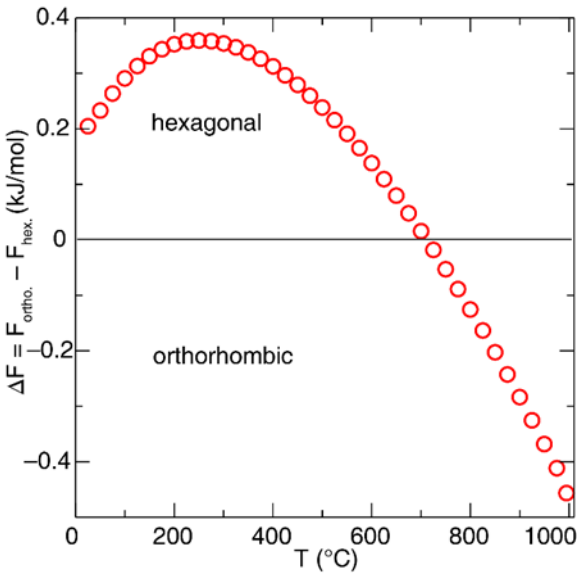

Figure S3.6. Difference in Helmholtz energy of orthorhombic and hexagonal

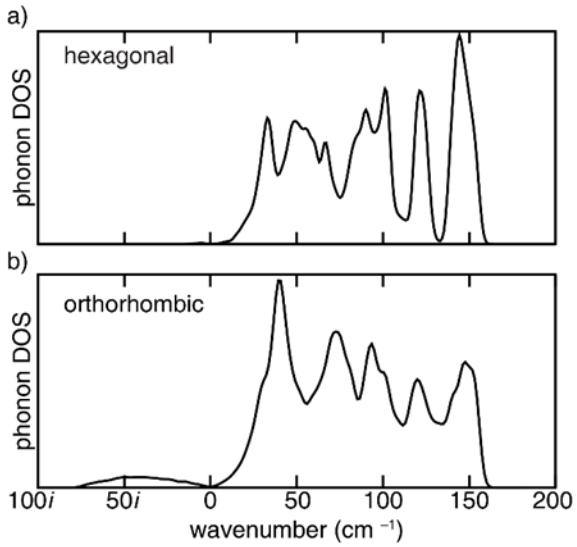

Figure S3.7. a) Calculated phonon density of states of LaAuSn in hexagonal space group shows no imaginary modes and in therefore dynamically stable. b) Calculated phonon density of states of LaAuSn in orthorhombic space group shows large imaginary modes causing structural instability.

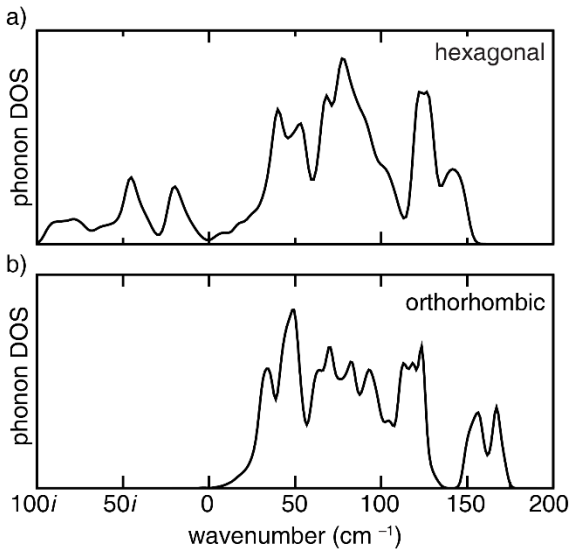

Figure S3.8. a) Calculated phonon density of states of $LaAu_{1.5}Sn_{0.5}$ in hexagonal space group shows large imaginary modes causing structural instability. b) Calculated phonon density of states of $LaAu_{1.5}Sn_{0.5}$ in orthorhombic unit cell shows no imaginary modes and in therefore dynamically stable

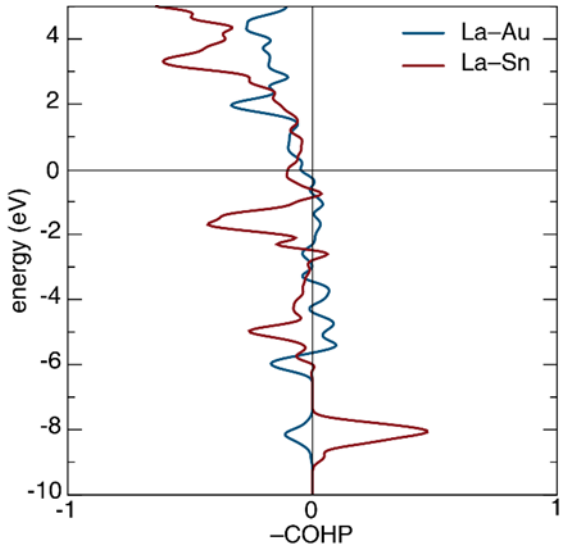

Figure S3.9. Crystal orbital Hamilton population (–COHP) curves plotting the average La–Au interactions (blue), and the average La–Sn interactions (red). The positive direction on the abscissa are bonding interactions, whereas negative values are antibonding interactions. The Fermi level is set to 0 eV.

Table S3.3. Bond angles for *RE*$Au_{1.5}Sn_{0.5}$

Atom	Angle (°)	Atom	Angle (°)
Au(1)#1-RE(1)-Au(1)#2	79.73(5)	Au(1)#3-RE(1)-Au(1)#9	112.192(13)
Au(1)#1-RE(1)-Au(1)#3	133.219(18)	Au(1)#4-RE(1)-Au(1)#9	87.077(15)
Au(1)#2-RE(1)-Au(1)#3	93.877(12)	Au(1)#5-RE(1)-Au(1)#9	167.83(5)
Au(1)#1-RE(1)-Au(1)#4	93.877(12)	Au(1)#6-RE(1)-Au(1)#9	49.40(2)
Au(1)#2-RE(1)-Au(1)#4	133.219(18)	Au(1)#7-RE(1)-Au(1)#9	77.06(3)
Au(1)#3-RE(1)-Au(1)#4	121.30(5)	Au(1)#8-RE(1)-Au(1)#9	90.10(2)
Au(1)#1-RE(1)-Au(1)#5	93.877(12)	Au(1)#1-RE(1)-Au(1)#10	49.073(18)
Au(1)#2-RE(1)-Au(1)#5	133.219(18)	Au(1)#2-RE(1)-Au(1)#10	98.25(4)
Au(1)#3-RE(1)-Au(1)#5	57.56(3)	Au(1)#3-RE(1)-Au(1)#10	87.077(15)
Au(1)#4-RE(1)-Au(1)#5	93.21(3)	Au(1)#4-RE(1)-Au(1)#10	112.192(13)
Au(1)#1-RE(1)-Au(1)#6	133.219(18)	Au(1)#5-RE(1)-Au(1)#10	49.40(2)
Au(1)#2-RE(1)-Au(1)#6	93.877(12)	Au(1)#6-RE(1)-Au(1)#10	167.83(5)
Au(1)#3-RE(1)-Au(1)#6	93.21(3)	Au(1)#7-RE(1)-Au(1)#10	90.10(2)
Au(1)#4-RE(1)-Au(1)#6	57.56(3)	Au(1)#8-RE(1)-Au(1)#10	77.06(3)
Au(1)#5-RE(1)-Au(1)#6	121.30(5)	Au(1)#9-RE(1)-Au(1)#10	141.06(6)
Au(1)#1-RE(1)-Au(1)#7	49.073(18)	Au(1)#1-RE(1)-Au(1)	167.92(4)
Au(1)#2-RE(1)-Au(1)#7	98.25(4)	Au(1)#2-RE(1)-Au(1)	112.354(17)
Au(1)#3-RE(1)-Au(1)#7	167.83(5)	Au(1)#3-RE(1)-Au(1)	48.851(19)
Au(1)#4-RE(1)-Au(1)#7	49.40(2)	Au(1)#4-RE(1)-Au(1)	77.92(4)
Au(1)#5-RE(1)-Au(1)#7	112.192(13)	Au(1)#5-RE(1)-Au(1)	77.92(4)
Au(1)#6-RE(1)-Au(1)#7	87.077(15)	Au(1)#6-RE(1)-Au(1)	48.851(19)
Au(1)#1-RE(1)-Au(1)#8	98.25(4)	Au(1)#7-RE(1)-Au(1)	125.82(3)
Au(1)#2-RE(1)-Au(1)#8	49.073(18)	Au(1)#8-RE(1)-Au(1)	90.259(17)
Au(1)#3-RE(1)-Au(1)#8	49.40(2)	Au(1)#9-RE(1)-Au(1)	90.259(17)
Au(1)#4-RE(1)-Au(1)#8	167.83(5)	Au(1)#10-RE(1)-Au(1)	125.82(3)
Au(1)#5-RE(1)-Au(1)#8	87.077(16)	Au(1)#1-RE(1)-Au(1)#11	112.354(17)
Au(1)#6-RE(1)-Au(1)#8	112.192(13)	Au(1)#2-RE(1)-Au(1)#11	167.92(4)
Au(1)#7-RE(1)-Au(1)#8	141.06(6)	Au(1)#3-RE(1)-Au(1)#11	77.92(4)
Au(1)#1-RE(1)-Au(1)#9	98.25(4)	Au(1)#4-RE(1)-Au(1)#11	48.851(19)
Au(1)#2-RE(1)-Au(1)#9	49.073(18)	Au(1)#5-RE(1)-Au(1)#11	48.851(19)

Table S3.3 Continued from previous page

Au(1)#6-RE(1)-Au(1)#11	77.92(4)	RE(1)#2-RE(1)-RE(1)#12	164.97(9)
Au(1)#7-RE(1)-Au(1)#11	90.259(17)	Au(1)#6-Au(1)-Au(1)#3	119.51(5)
Au(1)#8-RE(1)-Au(1)#11	125.82(3)	Au(1)#6-Au(1)-Au(1)#13	119.66(2)
Au(1)#9-RE(1)-Au(1)#11	125.82(3)	Au(1)#3-Au(1)-Au(1)#13	119.66(2)
Au(1)#10-RE(1)-Au(1)#11	90.259(17)	Au(1)#6-Au(1)-Au(1)#11	90
Au(1)-RE(1)-Au(1)#11	55.57(4)	Au(1)#3-Au(1)-Au(1)#11	90
Au(1)#1-RE(1)-RE(1)#2	137.38(7)	Au(1)#13-Au(1)-Au(1)#11	100.76(3)
Au(1)#2-RE(1)-RE(1)#2	57.65(3)	Au(1)#6-Au(1)-RE(1)#2	67.25(2)
Au(1)#3-RE(1)-RE(1)#2	57.22(2)	Au(1)#3-Au(1)-RE(1)#2	67.25(2)
Au(1)#4-RE(1)-RE(1)#2	114.41(4)	Au(1)#13-Au(1)-RE(1)#2	129.38(5)
Au(1)#5-RE(1)-RE(1)#2	114.41(4)	Au(1)#11-Au(1)-RE(1)#2	129.86(2)
Au(1)#6-RE(1)-RE(1)#2	57.22(2)	Au(1)#6-Au(1)-RE(1)#5	150.997(15)
Au(1)#7-RE(1)-RE(1)#2	131.39(2)	Au(1)#3-Au(1)-RE(1)#5	67.62(3)
Au(1)#8-RE(1)-RE(1)#2	54.972(16)	Au(1)#13-Au(1)-RE(1)#5	66.94(3)
Au(1)#9-RE(1)-RE(1)#2	54.972(16)	Au(1)#11-Au(1)-RE(1)#5	61.220(17)
Au(1)#10-RE(1)-RE(1)#2	131.39(3)	RE(1)#2-Au(1)-RE(1)#5	133.219(18)
Au(1)-RE(1)-RE(1)#2	54.70(3)	Au(1)#6-Au(1)-RE(1)#4	67.62(3)
Au(1)#11-RE(1)-RE(1)#2	110.27(6)	Au(1)#3-Au(1)-RE(1)#4	150.997(15)
Au(1)#1-RE(1)-RE(1)#12	57.65(3)	Au(1)#13-Au(1)-RE(1)#4	66.94(3)
Au(1)#2-RE(1)-RE(1)#12	137.38(7)	Au(1)#11-Au(1)-RE(1)#4	61.220(17)
Au(1)#3-RE(1)-RE(1)#12	114.41(4)	RE(1)#2-Au(1)-RE(1)#4	133.219(18)
Au(1)#4-RE(1)-RE(1)#12	57.22(2)	RE(1)#5-Au(1)-RE(1)#4	93.21(3)
Au(1)#5-RE(1)-RE(1)#12	57.22(2)	Au(1)#6-Au(1)-RE(1)#14	141.194(19)
Au(1)#6-RE(1)-RE(1)#12	114.41(4)	Au(1)#3-Au(1)-RE(1)#14	63.67(2)
Au(1)#7-RE(1)-RE(1)#12	54.972(16)	Au(1)#13-Au(1)-RE(1)#14	63.66(3)
Au(1)#8-RE(1)-RE(1)#12	131.39(2)	Au(1)#11-Au(1)-RE(1)#14	128.530(16)
Au(1)#9-RE(1)-RE(1)#12	131.39(3)	RE(1)#2-Au(1)-RE1)#14	81.75(4)
Au(1)#10-RE(1)-RE(1)#12	54.972(16)	RE(1)#5-Au(1)-RE(1)#14	67.808(13)
Au(1)-RE(1)-RE(1)#12	110.27(6)	RE(1)#4-Au(1)-RE(1)#14	130.60(2)

Table S3.3 Continued from previous page

Au(1)#3-Au(1)-RE(1)#15	141.194(19)	RE(1)#3-Au(1)-RE(1)	63.53(2)
Au(1)#13-Au(1)-RE(1)#15	63.66(3)	RE(1)#13-Au(1)-RE(1)	162.97(5)
RE(1)#11-Au(1)-RE(1)#15	128.530(16)	RE(1)#11-Au(1)-RE(1)	62.22(2)
RE1)#2-Au(1)-RE(1)#15	81.75(4)	RE(1)#2-Au(1)-RE(1)	67.646(17)
RE(1)#5-Au(1)-RE(1)#15	130.60(2)	RE(1)#5-Au(1)-RE(1)	102.08(4)
RE(1)#4-Au(1)-RE(1)#15	67.808(13)	RE(1)#4-Au(1)-RE(1)	102.08(4)
RE(1)#14-Au(1)-RE(1)#15	90.10(2)	RE(1)#14-Au(1)-RE(1)	125.82(3)
RE(1)#6-Au(1)-RE(1)	63.53(2)	RE(1)#15-Au(1)-RE(1)	125.82(3)

Table S3.4. Anisotropic displacement parameters (Å^2) for $LaAu_{1.5}Sn_{0.5}$

Atom	U_{11}	U_{22}	U_{33}	U_{23}	U_{13}	U_{12}
La	0.0199(9)	0.0105(6)	0.0177(9)	0	0	0
Au	0.0063(4)	0.0225(5)	0.0067(5)	0	0	0
Sn	0.0063(4)	0.0225(5)	0.0067(5)	0	0	0

Table S3.5. Anisotropic displacement parameters (Å^2) for $CeAu_{1.5}Sn_{0.5}$

Atom	U_{11}	U_{22}	U_{33}	U_{23}	U_{13}	U_{12}
Ce	0.0212(9)	0.0063(6)	0.0209(8)	0	0	0
Au	0.0063(4)	0.0245(5)	0.0102(4)	0	0	0
Sn	0.0063(4)	0.0245(5)	0.0102(4)	0	0	0

Table S3.6. Anisotropic displacement parameters (Å^2) for $PrAu_{1.5}Sn_{0.5}$

Atom	U_{11}	U_{22}	U_{33}	U_{23}	U_{13}	U_{12}
Pr	0.0223(1)	0.0091(8)	0.0191(1)	0	0	0
Au	0.0071(6)	0.0213(8)	0.0077(6)	0	0	0
Sn	0.0071(6)	0.0213(8)	0.0077(6)	0	0	0

Table S3.7. Anisotropic displacement parameters (Å^2) for $NdAu_{1.5}Sn_{0.5}$

Atom	U_{11}	U_{22}	U_{33}	U_{23}	U_{13}	U_{12}
Nd	0.0245(9)	0.0111(6)	0.0198(8)	0	0	0
Au	0.0072(4)	0.0264(6)	0.0079(4)	0	0	0
Sn	0.0072(4)	0.0264(6)	0.0079(4)	0	0	0

Chapter 4

Predicting Pressure-Stabilized Alkali Metal Iridides: *A*–Ir (*A* = Rb, Cs)

Reproduced with permission from *Computational Materials Science*
(*Comput. Mater. Sci.* 2019, 158, 124-129)

DOI: 10.1016/j.commatsci.2018.11.018

Sogol Lotfi and Jakoah Brgoch*

Department of Chemistry, University of Houston, Houston, Texas 77204, United States

4.1 Introduction

High pressure significantly alters the crystal chemistry of elements complicating our understanding of chemistry's fundamental rules. More specifically, applying high pressure can change a compound's crystal structure and/or bonding pattern resulting in the formation of materials with interesting and unexpected chemical and physical properties.[168–170] One example is the pressure induced crystal structure transformation in high-entropy alloys, which are mostly constrained to face- or body-centered cubic crystal structures. However, applying pressure (starting at ≈14 GPa) can lead to a crystal structure transformation like from *fcc* to *hpc* in CrMnFeCoNi alloys.[171] Exerting external pressure on the Na–Cl binary system provides an excellent example of how chemical bonding patterns and charge transfer can also behave differently in extreme environments. Classically, NaCl is

the only stable binary solid in the Na–Cl system, adopting the archetypal structure type held together by prototype ionic interactions. Subjecting Na and Cl to more than 120 GPa leads to the extraordinary discovery of Na_3Cl with the experimentally confirmed *P*4/*mmm* space group and two-dimensional metallic behavior.[172] Although the capability to conduct high-pressure synthesis has been significantly expanded, these experiments remain complex, limiting the potential to understand the resulting chemistry.

Since high-pressure synthesis and crystal structure analysis are arduous, computational modeling paired with efficient crystal structure prediction algorithms has become a valuable tool for understanding the complex crystal chemistry of inorganic solids at non-ambient conditions.[113,122,123,173–176] For example, elemental cesium is classically considered to react with halogen atoms and oxidize to the +1 state. Yet, recent work in the Cs–F binary phase space under high pressure (>10 GPa) suggests the formation of other compounds following the general formula CsF_n (n>1).[177] These captivating results imply that cesium's oxidation state can differ from the conventionally accepted +1 state due to the participation of the Cs 5*p* orbitals under high pressure. There are numerous other examples of unexpected chemistry at high pressure.[178,179] For example, the Mg–*NG* (*NG* = Xe, Kr, Ar) system forms binary compounds above ~125 GPa, even though noble gasses are virtually inert under normal conditions.[58] The potential for different crystal structures of solid CO_2,[180] binary compounds in the Xe–Fe and Xe–Ni systems,[59] and novel polyhydrides[181] have all been revealed with the aid of computational techniques.

Applying high pressure is sufficient to also influence the chemistry of transition metals. For example, CsAu is one of the simplest gold containing binary compounds adopting the CsCl-type structure containing isolated an Au^- anion. However, applying >14 GPa to the crystal structure is predicted to cause a phase transformation from the cubic

$Pm\bar{3}m$ structure to an orthorhombic *Cmcm* structure with a zigzag Au–Au chain. The pressure shifts the atomic orbital energies of gold, causing sufficient electronic instabilities to drive a crystal structure change. Applying high pressure can also allow this late transition metal to adopt unusual oxidation states. Gold was predicted to achieve unexpected and diverse negative oxidation states in the range of −1 to −3 for Li-rich aurides when squeezed to 25–100 GPa.[182] The surprising observation of an anionic transition metal under pressure is not limited to gold, applying high pressure in the investigation of K–Ir binary system demonstrates that above 10 GPa the formation of K_3Ir becomes favorable.[61] K_3Ir is of great interest not only for being the first suggested compound formed between an alkali metal and iridium, but this compound also was calculated to contain Ir in an anionic oxidation state (−1.64 e^-/Ir) as well as undergo a superconducting transition at low temperature.[61]

In this work, the particle swarm optimization (PSO) method CALYPSO (crystal structure analysis by particle swarm optimization) was employed to identify other examples of anionic iridium in inorganic solids.[46] The PSO algorithm has been proven to perform successfully in many optimization problems.[63] Indeed, PSO's fast learning ability, multidimensional search, simplicity, and a limited number of variables has made it an effective approach to predict crystal structures under high pressure. Here, the research started by constructing convex hulls for Rb–Ir and Cs–Ir using *ab initio* calculations and particle swarm optimization methods to predict the most likely crystal structures at various compositions and elevated pressures. The results indicate that above ≈10 GPa compounds with the formulae A_2Ir and A_3Ir (A = Rb, Cs) are energetically favorable to form, although only the latter is dynamically stable according to phonon calculations. Further analysis of the electronic structure for A_3Ir shows this combination of a highly electropositive alkali metal with iridium results in significant chemical interactions, while the transition metal

once more adopts an unusual anionic oxidation state. These calculations provide further evidence that charge-separated iridides are indeed likely to exist with exotic oxidation states under high pressure.

4.2 Computational Details

The most probable binary crystal structures in the Rb–Ir and Cs–Ir systems were obtained using a particle swarm optimization (PSO) approach, as implemented in the Crystal Structure Analysis by Particle Swarm Optimization (CALYPSO).[53] The structure search was carried out on different stoichiometric ratios of the elements, including A_3Ir, A_2Ir, AIr, AIr$_2$, and AIr$_3$ (A = Rb, Cs) in a pressure range from 1×10^{-4} GPa (herein referred to as 0 GPa) to 20 GPa in steps of 5 GPa. The simulation unit cell size was varied between 2 and 4 formula units (f.u.). Total energy calculations required for the crystal structure search, as well as the ensuing electronic structure calculations for the chemical bonding analyses, were all performed using Density Functional Theory (DFT) within the Vienna *ab initio* Simulation Package (VASP).[117,118] The calculations employed a plane-wave basis set and projector-augment-wave (PAW) potentials.[119] The generalized gradient approximation (GGA) was used with exchange and correlation described by the Perdew–Burke–Ernzerhof (PBE) functional. The basis set for the calculation included Rb (4p, 5s); Cs (5p, 6s); Ir (5d, 6s) wavefunctions. The total energy calculations used a cutoff energy of 500 eV, a 4×4×4 Γ-centered Monkhorst–Pack **k**-point grid, and convergence criteria of 1×10^{-8} eV and 1×10^{-6} eV for the electronic and structure relaxation, respectively. The phonon density of states (PhDOS) was calculated using the PHONOPY package,[124,125] which uses the modified Parlinski–Li–Kawazoe *ab initio* force constant method and 2×2×2 supercells. The band gap of Rb$_3$Ir was additionally evaluated with the Heyd-Scuseria-Ernzerhof screened hybrid exchange and correlation functional, HSE06, which implements a mixture of PBE (75%) and

Hartree-Fock exact exchange (25%) and a range-separation of 0.2 Å^{-1}.[183] The chemical bonding of Rb_3Ir and Cs_3Ir was finally evaluated based on the crystal orbital Hamilton population (−COHP) using the Local-Orbital Basis Suite toward Electronic Structure Reconstruction (LOBSTER) code,[156,157] the electron localization function(ELF),[158,166] and a Bader charge analysis.[161] All crystal structure drawings were visualized using program VESTA.[112]

4.3 Results and Discussion

4.3.1 Particle Swarm Optimization Structure Search

The particle swarm optimization (PSO) algorithm can efficiently predict novel crystal structures without previous knowledge of reported structures types. This approach uses DFT to optimize CALYPSO generated crystal structures and calculate their total energies, which are necessary to determine the formation enthalpies. In these calculations, 60% of the crystal structures with the most favorable enthalpies (lowest energies) from previous generations were employed in the next generation, while the other 40% of the structures were randomly created. For each composition and all pressures probed, between 40 and 50 generations were produced with each generation containing 20 individual structures. Overall, ≈1000 crystal structures were constructed by paring CALYPSO with DFT for each data point on the convex hull.

Once the most favorable crystal structure for each composition was identified by comparing the relative total energies of the CALYPSO generated structures, the formation enthalpy per atom (ΔH) was then calculated using Equation 1,

$$\Delta H = [H(A_3Ir) - 3H(A) - H(Ir)] \quad (4.1)$$

where $H(A_3Ir)$ (A = Rb, Cs) is the enthalpy of A_3Ir per atom, $H(A)$is enthalpy of A (A = Rb, Cs) per atom, and $H(Ir)$ is enthalpy of Ir per atom. Because Rb and Cs both undergo phase transformations at elevated pressures, the crystal structures of the alkali metals (Rb and Cs) were treated differently at each pressure step. For instance, Rb is known to adopt space group $Im\bar{3}m$ from 0 to 7 GPa, then transform to space group $Fm\bar{3}m$ from 7 to 13 GPa, followed by space group $C222_1$ from 13 to 16.8 GPa, and finally space group $I4/mmm$ from 16.8 to 20 GPa.[184–187] For Cs, the known crystal structures are, $Fm\bar{3}m$ from 0 to 4.3 GPa, $C222_1$ from 4.3 to 8 GPa, $I4_1/amd$ from 8 to 12 GPa, $Cmca$ from 12 to 13.3 GPa, $I4_1/amd$ from 13.3 to 18 GPa, and $P4_2/mbc$ from 18 to 20 GPa.[188–190] Iridium maintains its *fcc* crystal structure at all pressures considered in these calculations.[191]

To examine a range of stoichiometries in the binary A–Ir (A = Rb, Cs) systems, the convex hulls were calculated based on ΔH obtained from Equation 1 and plotted in Figure 1 at applied pressures of 0 GPa, 10 GPa, and 20 GPa. The calculated formation enthalpies at 0 GPa show ΔH is positive for every composition, indicating decomposition into the starting materials. This supports the absence of thermodynamically stable compounds reported in these binary systems at ambient pressure. As the pressure increases, the calculated formation enthalpy decreases. Once the pressure increases above 10 GPa, two compositions, A_2Ir and A_3Ir, have negative formation enthalpies revealing the energetic potential to form at elevated pressure. Subsequent phonon calculations were, therefore, conducted to confirm these crystal structures are also dynamically stable, *i.e.*, the crystal structures are not expected to undergo a phase transformation. First, the PhDOS calculations performed for A_2Ir show the presence of imaginary modes for both A = Rb and A = Cs (Figure S1), which means these compositions are not dynamically stable in their respective predicted structure types. Moreover, constructing the convex hulls for both

binary diagrams shows that A_2Ir falls above the hull (Figure 1) signifying these compounds should decompose to A_3Ir and elemental A. Thus, even though A_2Ir (A = Rb, Cs) has a negative formation enthalpy, based on the convex hull and phonon calculations, it is unlikely either compound will form in the pressure ranges examined.

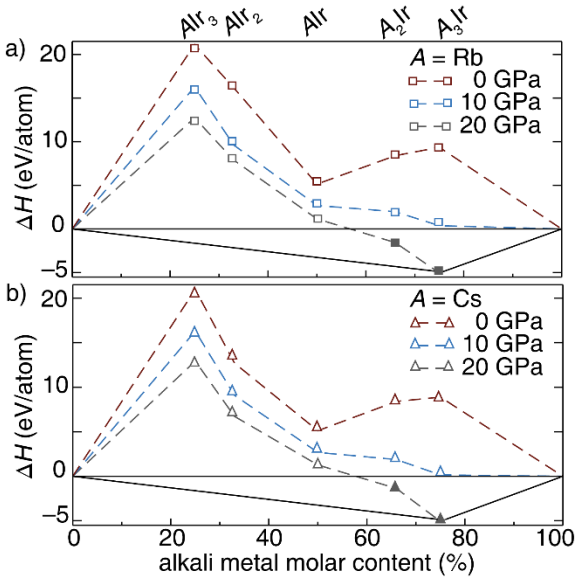

Figure 4.1. The relative enthalpies of formation per atom for a) the binary Rb–Ir system, and b) the binary Cs–Ir system at 0, 10, and 20 GPa. The solid line indicates the convex hull and neighboring points are connected by dotted lines.

Given that A_3Ir (A = Rb, Cs) are the only phases on the convex hull, as illustrated in Figure 1, their probable crystal structures were examined in more detail. Both compositions are predicted to form as two different crystal structures with similar formation enthalpies. For Rb_3Ir, the predicted phases adopt space groups $R\bar{3}m$ and $Pmnm$, whereas Cs_3Ir was predicted to adopt $P2_1/m$ or $P6_3cm$. Plotting the ΔH versus pressure (Figure 2) proves both compounds should decompose into the elements until the pressure is >10 GPa, in agreement with the convex hulls. Above ≈10 GPa, the most favorable crystal structures have a negative ΔH, meaning the compounds will no longer decompose and are expected to form

the products. Investigating each predicted space group shows that Rb_3Ir in the $R\bar{3}m$ and *Pmnm* crystal structures have close formation enthalpies, differing by only ≈19 meV/atom eV at 20 GPa. Therefore, the dynamic stability of both crystal structures was calculated. The PhDOS calculations indicate both structures are also dynamically stable at 20 GPa (Figure 2c). The similar ΔH, which is less than the energy available at ambient temperature (25 meV), along with dynamic stability suggests that both crystal structures may be expected at a reasonably elevated temperature. Care must therefore be taken in any experimental determination of the crystal structure. Nevertheless, for the further investigation here, Rb_3Ir was only considered in the *Pmnm* space group because it has the lowest DFT calculated ΔH. For completeness, the crystal structure information for Rb_3Ir in $R\bar{3}m$ is still provided in Table S4.1, and the structure is illustrated in Figure S4.2.

Likewise, two crystal structures ($P2_1/m$ and $P6_3cm$) with the lowest formation energy were also analyzed for Cs_3Ir composition, as shown in Figure 2b. Again, below ≈10 GPa the compounds are expected to decompose; above 10 GPa the $P2_1/m$ has the lowest ΔH by 21 meV/atom. However, phonon density of state calculations, in this case, shows the $P6_3cm$ structure is dynamically unstable, whereas $P2_1/m$ is dynamical stable, illustrated in Figure 2d. These results support $P2_1/m$ as the most likely crystal structure for Cs_3Ir.

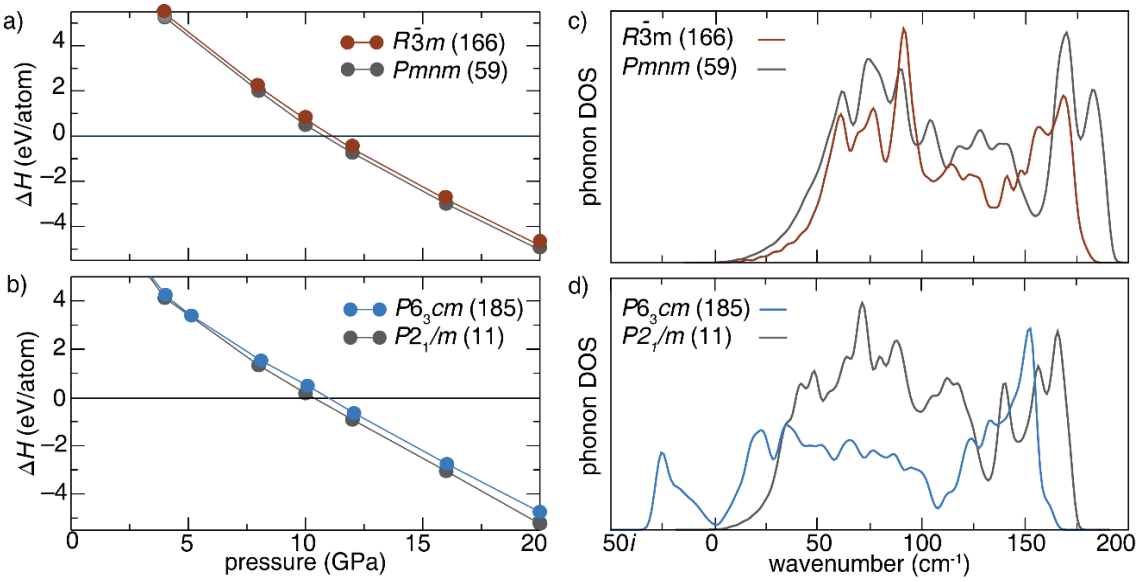

Figure 4.2. Calculated formation enthalpy (ΔH) as a function of pressure between 0 to 20 GPa. Two plausible crystal structures predicted by particle swarm optimization (PSO) for a) Rb_3Ir and b) Cs_3Ir. c) PhDOS for Rb_3Ir at 20 GPa showing that both crystal structures are dynamically stable. d) PhDOS for Cs_3Ir at 20 GPa showing $P2_1/m$ crystal structure is dynamically stable, whereas $P6_3cm$ has imaginary modes.

4.3.2 Crystal Chemistry, Electronic Structure, and Chemical Bonding

An in-depth examination of the lowest energy crystal structures for Rb_3Ir and Cs_3Ir at high pressure shows noteworthy crystal chemistry. Rb_3Ir is predicted to crystallize in space group *Pmnm* (No. 59, Z = 2) with an ordered Cu_3Ti-type crystal structure, as shown in Figure 4.3a. Previously, K_3Ir was also predicted as an isostructural analog, albeit with a slightly smaller unit cell volume compared to Rb_3Ir due to the size difference between K and Rb.[61] This orthorhombic space group of Rb_3Ir has optimized lattice parameters of a = 5.290 Å, b = 5.446 Å, c = 7.075 Å, and a unit cell volume of 203.819 Å^3. The optimized atomic positions for Rb_3Ir are provided in Table 1. In Rb_3Ir, Rb forms a distorted square net that stacks in a $\cdots ABAB \cdots$ arrangement along the c-direction resulting in a three-dimensional face-sharing network of very distorted square prisms. These distorted cubes are centered

by a combination of additional Rb and Ir atoms ([Rb@Ir_8] and [Ir@Rb_8]) in an alternating fashion, as illustrated in Figure 4.3b. Each iridium in the cube has site symmetry *mm*2 and is 8-coordinated by Rb, whereas Rb occupies two crystallographically independent sites with symmetry *m..* (in the square net) and *mm*2 (in the cubes). The interatomic distances for Rb–Ir are in the range 3.22–3.28 Å, and the Rb–Rb bond lengths are 3.155 Å and 3.245 Å. These Rb–Rb distances in the high-pressure phase of Rb_3Ir are significantly shorter compared to the other compounds containing Rb–Rb interactions at ambient pressure (3.66 Å–4.68 Å), as expected.[184,192,193]

Cs_3Ir is predicted to form a different crystal structure (Ni_3Ta-type) adopting space group $P2_1/m$ (No. 11, Z = 2) with lattice parameters of a = 5.705 Å, b = 6.677 Å, c = 5.328 Å, and a unit cell volume of 202.874 $Å^3$. The optimized atomic positions for Cs_3Ir are provided in Table 1. The crystal structure is shown in Figure 3c, and contains two independent crystallographic positions for Cs and one independent position for Ir. Cs_3Ir is constructed of an Ir centered 12-vertex distorted cuboctahedron with a 3-6-3 arrangement of cesium atoms oriented along *c* direction, as illustrated in Figure 3d. Cs1 occupies the general position Wyckoff site 4*f* whereas Cs2 sits at Wyckoff site 2*e* with site symmetry *m*. Probing the optimized bond lengths in this structure shows the Cs–Ir, and Cs–Cs interatomic distances are in the range of 3.21-3.65 Å and 3.20-3.29 Å, respectively. The Cs–Cs bond lengths in this compound are similar to Cs–Cs interactions under pressure (3.25 Å).[190]

Table 4.1. VASP-optimized atomic positions of Rb_3Ir (*Pmnm*; $Z = 2$, $a = 5.290$ Å, $b = 5.446$ Å, and $c = 7.075$ Å) and Cs_3Ir ($P2_1/m$; $Z = 2$, $a = 5.705$ Å, $b = 6.677$ Å, and $c = 5.328$ Å).

	atoms	Wyck.	*x*	*y*	*z*
Rb_3Ir					
	Rb1	4*f*	0	0.1550	1/4
	Rb2	2*b*	1/2	0.3450	0
	Ir1	2*a*	0	0.6550	0
Cs_3Ir					
	Cs1	4*f*	0.67592	0.5001	0.7556
	Cs2	2*e*	0.84601	1/4	0.26042
	Ir1	2*e*	0.81140	3/4	0.2499

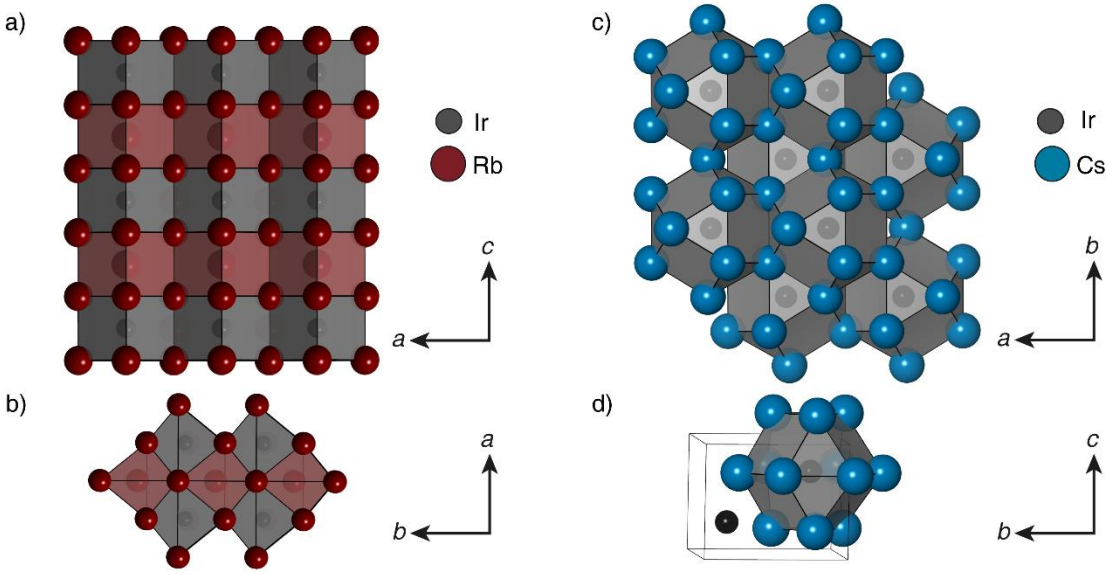

Figure 4.3. a) View of the Rb_3Ir structure along the *b*-axis and b) stacked along the *c*-axis. c) View of the Cs_3Ir structure along the *c*-axis and d) the polyhedral around Ir. Iridium, rubidium, and cesium are shown as grey, red, and blue, respectively.

Calculating the electronic structure of A_3Ir (A = Rb, Cs) at 20 GPa reveals that Rb_3Ir is nonmetallic with the Fermi level falling in a band gap, shown in Figure 4.4a, whereas Fermi level for Cs_3Ir falls into pseudogap (Figure 4b). The calculated band gap (E_g) from PBE function value is approximately 1 eV for Rb_3Ir, which is slightly smaller than for K_3Ir (E_g ≈1.6 eV).[61] A hybrid functional (HSE06) calculation was subsequently performed to

determine a more precise E_g of 1.33 eV for Rb_3Ir. Decomposing the total electronic density of states (DOS) into its component orbitals show the Ir 5*d* orbitals are mainly populated just below the Fermi level in the range of –1 to 0 eV and are entirely filled for both Rb_3Ir and Cs_3Ir. Interestingly, because the 5*d* orbitals of the late transition metals, *e.g.*, Ir, Pt, and Au, reside near the Fermi level, when combined with electropositive elements, the result is the potential for anionic character on the metal sites.[33] For both compounds, 6*s* orbital has fallen below the 5*d* orbital of Ir, and alkali metals' bands are spread across the entire energy range examined.

For a better understanding of the crystal chemistry and chemical bonding in these two compounds, the interatomic interactions were calculated based on a crystal orbital Hamilton population (–COHP) analysis using LOBSTER. As shown in Figure 4, Rb_3Ir contains Rb–Ir interactions with the bonding and half of the antibonding orbitals filled. Examining the integrated COHP (–ICOHP) curves proves that although most of the antibonding orbitals are filled, the Rb–Rb contacts are still favorable with a value of 0.532 eV/bond, while the Rb–Ir interactions are more significant (0.972 eV/bond). The Cs–Cs interactions in Cs_3Ir are mainly optimized in this crystal structure. This contrasts with the Cs–Ir interactions which contain half-occupied antibonding orbitals. The –ICOHP values in Cs_3Ir are still significantly larger compared to Rb_3Ir with values of 2.286 eV/bond for the Cs–Cs contacts and 2.660 eV/bond for the Cs–Ir interactions. Considering that the COHP curves are known to scale with bond strength, comparing the –ICOHP values for both Rb_3Ir and Cs_3Ir provide convincing evidence that the interactions in Cs_3Ir are greater in Rb_3Ir. Stronger interactions are also supported by the DOS calculations that show a gap at Fermi level in the Rb_3Ir crystal structure, while Fermi level falls at pseudogap for Cs_3Ir. More significant bonding

interactions will result in larger band dispersion that can close the band gap, as observed here.

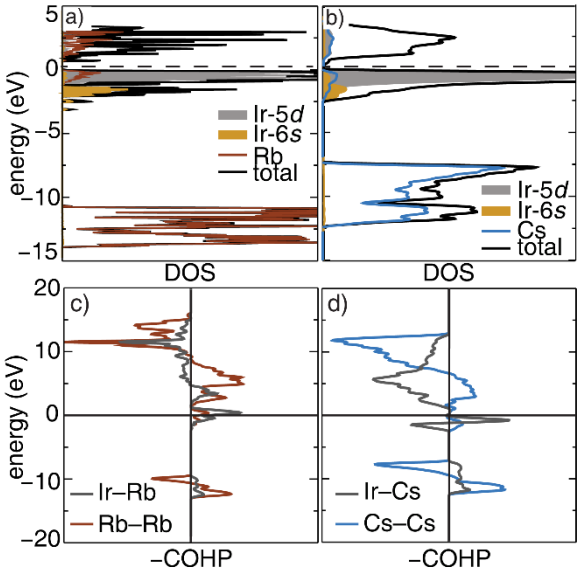

Figure 4.4. a) DOS using PBE functional for Rb_3Ir in *Pmnm* crystal structure. The total density of states is shown in by the black line, while the partial DOS is shown grey, yellow, and red for Ir 5*d*, Ir 6*s*, and Rb, respectively. b) Total and partial DOS using the PBE functional for Cs_3Ir in the $P2_1/m$ crystal structures. Total DOS is shown in by the black line, while the partial DOS is shown grey, yellow, and blue for Ir 5*d*, Ir 6*s*, and Cs, respectively. c) −COHP curves plotting the average Rb–Ir and Rb–Rb interactions. d) −COHP curves plotting the average Cs–Ir, and Cs–Cs interactions. The Fermi level is set to 0 eV in all plots, and in the −COHP curves, the negative directions on the abscissa are antibonding interactions, whereas positive values are bonding interactions.

To understand the difference between the atomic interactions in Rb_3Ir and Cs_3Ir in greater detail, the interactions in the crystal structures were also visualized by calculating the valence electron localization function (ELF). As illustrated in Figure 4.5, the higher values (red color) indicates more electron localization, whereas the lower values (dark blue) correspond to weaker localizations. The ELF plot of Rb_3Ir (Figure 4.5a) suggests weak interactions between Rb and Ir atoms near the (040) plane, implying

nonbonding/noncovalent interactions in Rb_3Ir calculated crystal structure. The ELF plot of Cs_3Ir (Figure 4.5b) illustrates the interactions near the (030) plane in the distorted Cs–Cs hexagon. Based on this calculation, interactions between Cs–Cs, and Cs–Ir atoms display low values of ELF, also indicating weak localization and no significant covalent component to these interactions. The ELF analysis supports the charge transfer and the nominal assignment of A^+ (A = Rb, Cs) and Ir^-.

Finally, Bader's quantum mechanics atom-in-molecule (QM-AIM) charge analysis was performed for Rb_3Ir and Cs_3Ir to approximate the oxidation states and charges on all atoms. Bader charge analysis shows that Rb_3Ir has an average $-1.59e^-$ per Ir and $+0.53e^-$ per Rb atoms whereas Cs_3Ir has an average $-1.39e^-$ per Ir and $+0.46e^-$ per Cs atoms. This comparison gives solid support of charge transfer from the alkali metal to Ir in A_3Ir (A = Rb, Cs), confirming the presence of iridide anion. Although the Bader charge analysis usually underestimates the anticipated charge on atoms, the oxidation state of iridium under applied pressure is beyond −1 for A_3Ir (A = Rb, Cs).

These oxidation states are somewhat surprising considering the lower electronegativity of Cs relative to Rb should promote charge transfer even though the calculations here suggest a greater charge transfer occurs in Rb_3Ir compared to Cs_3Ir. Examining the charge transfer as a function of pressure, plotted in Figure 4.5c and 4.5d, reveals that the average Bader charge on each atom decreases with increasing pressure. This response is similar to other previously reported high-pressure compounds[194], and likely stems from the enhanced metallic character as band dispersion increases under pressure. Also, Rb_3Ir gains more average charge compared to Cs_3Ir, indicating more metallic nature of Cs_3Ir. Interestingly, the DOS calculations indicate larger band gaps for Rb_3Ir, and –

COHP analysis offers less covalent interactions for Rb_3Ir, in support of the Bader charge calculations.

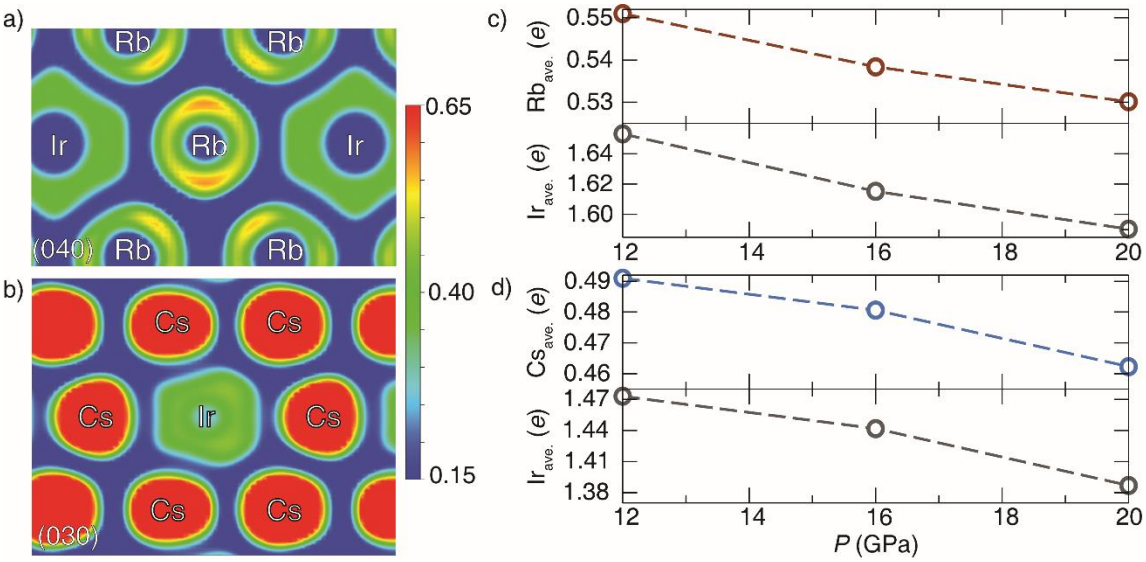

Figure 4.5. a) ELF of Rb_3Ir near (040). b) ELF of Cs_3Ir near (030) plane. c) The average Bader charge of the Rb and Ir atoms in Rb_3Ir and d) Cs and Ir atoms in Cs_3Ir as a function of pressure.

4.4 Conclusion

At ambient pressure, the alkali metals and Ir do not form binary compounds; however, applying high pressure enhances their reactivities and allows the formation of inorganic compounds. In this research, two phases with the general composition of A_3Ir (A = Rb, Cs) are predicted by CALYPSO after constructing the convex hull for the Rb–Ir and Cs–Ir. At high pressure, Rb_3Ir is predicted to adopt the Cu_3Ti-type crystal structure, and Cs_3Ir should form the Ni_3Ta-type structure. Both crystal structures are not only thermodynamically favorable, but they are also dynamically stable from ≈10 GPa until at least 20 GPa, which is the maximum pressure studied here. Electronic structure analysis reveals nonmetallic and semi-metallic nature of Rb_3Ir and Cs_3Ir, respectively, while the chemical bonding in these compounds indicates interactions in Cs_3Ir are likely stronger than Rb_3Ir. In conjunction with

the electronic structure and −COHP analysis, the Bader charge analysis confirms the presence of iridide. These results show that mixing heavy transition metals with electropositive alkali metals, and applying pressure is one route to drive the oxidation state of iridium to be reduced beyond −1 state.

4.5 Acknowledgments

The authors gratefully acknowledge the generous financial support provided by the National Science Foundation through No. NSF-CMMI 15-62142 and the donors of the American Chemical Society Petroleum Research Fund (55625-DNI10) for supporting this research. This research also used the Maxwell/Opuntia/Sabine Cluster operated by the University of Houston and the Center for Advanced Computing and Data Systems. Support for this work was also provided by resources of the uHPC cluster managed by the University of Houston and acquired through NSF Award Number 15-31814.

Supporting Information

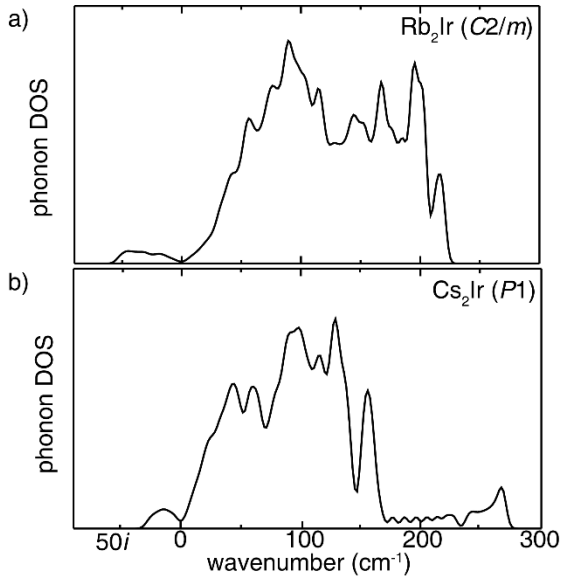

Figure S4.1. PhDOS for a) Rb_2Ir with space group $C2/m$, and b) Cs_2Ir with space group $P1$. There are imaginary modes for both compounds at 20 GPa, imply the instability of crystal structures.

Table S4.1. VASP-optimized atomic positions of $R\bar{3}m$-Rb_3Ir at 20 GPa(a = 4.34 Å, α = 84.95°)

	atoms	Wyck.	x	y	z
Rb_3Ir					
	Rb1	3e	0	1/2	1/2
	Ir1	1a	0	0	0

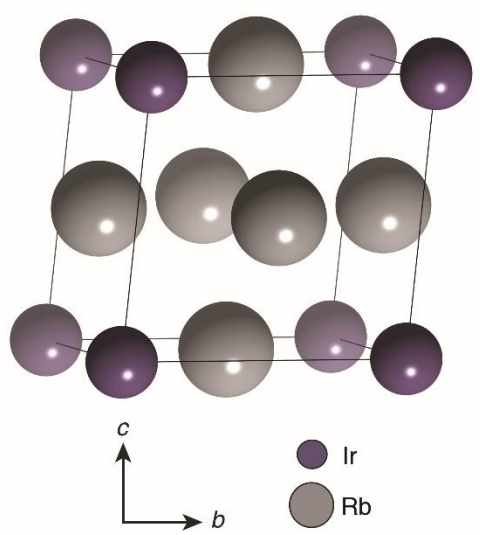

Figure S4.2. View of the $R\bar{3}m$ structure for Rb_3Ir composition along the *a*-axis. Iridium and rubidium are shown as purple and grey, respectively.

Chapter 5

Targeting Productive Composition Space through Machine-Learning Directed Inorganic Synthesis

Reproduced with permission from *ChemRxiv*

DOI:10.26434/CHEMRXIV.11803119.V2

Sogol Lotfi[1‡], Ziyan Zhang[1‡], Gayatri Viswanathan[1], Kaitlyn Fortenberry[1], Aria Mansouri Tehrani[1], and Jakoah Brgoch[1,2]*

[1]*Department of Chemistry, University of Houston, Houston, Texas 77204, United States*

[2]*Texas Center for Superconductivity, Houston 77204, Texas, United States*

5.1 Introduction

There is a continual need to prepare novel, complex inorganic solids with captivating crystal structures and the potential for superior functional properties. This has required researchers to employ a range of inorganic and solid-state synthesis methodologies ranging from direct reaction of the elements using high-temperature furnaces to more elegant molten metal flux reactions.[16] Historically, one of the most straightforward methods to identify new compounds using these synthetic approaches has been through classical exploratory synthesis, where phase diagrams are exhaustively studied. However, the construction of phase diagrams and the identification of new compounds using this traditional idea requires methodical synthesis and thorough thermal analyses,[195] which to

do correctly is exceptionally time-consuming and often costly. Thus, a significant research advance would be to directly pinpoint new compounds *a priori,* thereby reducing the number of experiments required to explore under-studied composition spaces and more rapidly obtain the tremendous number of compounds and crystal structures that remain unreported.

The ability to computationally search for thermodynamically stable phases has long been sought as a way to minimize the number of synthesis attempts for the discovery of new compounds. Most recently, density functional theory (DFT) has become a practical tool for calculating accurate formation energies at zero-Kelvin. When combined with genetic algorithm-based structure search methods this computational approach is capable of predicting unknown crystal structures.[49,63,123] This approach has been widely employed to predict the formation of compounds especially under non-ambient conditions,[62,122,172,182] such as the formation of binary noble gas containing phases or unusual oxidation states on alkali metals at high pressure.[58,196,197] These ideas have been expanded to the construction of convex hulls using DFT calculated formation energies as a way to examine unstudied phase spaces in the search for new compounds. For example, constructing the convex hull using predicted formation enthalpies has led to the discovery of novel superconducting, semiconducting,[198] and superhard materials.[199] Furthermore, the ever-increasing accessibility to high-throughput DFT databases, such as the Materials Project,[73] AFLOW,[74] and OQMD,[75] provides all researchers with massive DFT data sets that contain formation energies, which can be analyzed as a way to discover potential new compounds. Despite the reasonably high-fidelity and access to these calculations, however, it remains often impractical to use only DFT as a predictive screening tool due to its inheret shortcomings,

including difficulty calculating statistical disorder (site-sharing) in a crystal structure, limited unit cell sizes, and limited ability to expand beyond absolute zero.

A common supplement to DFT that has been adopted by the inorganic materials community to address some of these shortcomings is data-centered, machine-learning algorithms. These methods have been widely suggested for rapid materials discovery and have been made possible almost entirely by the prior creation of massive crystal structure databases and the complementary computational (DFT) databases. The content in these databases include crystal structure type, electronic structure information, elastic moduli, and calculated formation energies, and more.[200–204] Recent studies have proven that machine learning can use this information to reliably predict a host of material properties or recommend the most probable structure type for a given composition with accuracies approaching DFT but at a fraction of the computational cost.[205] It is also possible to predict phase formation as well as the formation energies of compounds. For example, a machine-learning model has been created to predict metallic glass-forming ability in the Al-Ni-Zr system by locating favorable compositions on the ternary phase diagram.[206] In another study, the total internal energies (E_{tot}) and formation enthalpies (ΔH_f) were predicted for metal-nonmetals compounds using linear regression.[207] Additionally, a random forest algorithm has been successfully applied to discover novel quaternary Heusler compounds by predicting the stability of crystalline material, while, in the other study, the stability of full-Heusler compounds has been predicted using convolutional neural networks.[85,208] The thermodynamic stability of perovskite and anti-perovskite phases are another example of accelerating materials discovery using machine learning.[202] In each of these studies, the data-driven methods can predict specific crystal structures or compositions in systems where there is sufficient training data. However, extrapolating these ideas to identify new

compounds in unexplored regions of composition space has proven difficult, which is why most of the previous data-centered predictions are restricted to specific composition regions or crystal structure types. Given the fact that researchers have long-established synthetic approaches to skilfully search through composition space and identify new phases, it would be valuable to merge classic solid-state phase space searching with data science to produce a new methodology that can efficiently examine under-explored regions containing new compounds.

In this work, we established a method that combines experimental synthetic inorganic chemistry and machine learning to accelerate the discovery of new inorganic solids by identifying productive regions of composition space using ensemble data mining and machine learning. The model is developed using a support vector regression (SVR) algorithm with a training set based on DFT formation energies, $\Delta E_{f,\mathrm{DFT}}$, data compiled by the Materials Project and OQMD, and a descriptor set based only on chemical composition. This allows the machine-learning model to predict $\Delta E_{f,\mathrm{SVR}}$ of any composition, which can then be used to construct the convex hull and identify the most energetically favorable compounds. Although, strictly speaking, these "phase diagrams" represent a zero-Kelvin isothermal section, the entropy of solid-solid reactions considered in most solid-state chemistry is negligible allowing DFT/machine learning derived $\Delta E_{f,\mathrm{SVR}}$ to still be useful in predicting the formation of compounds at any reasonable temperature at equilibrium. As a result, this approach can sufficiently approximate phase diagrams and provide a new opportunity for data-directed exploratory synthesis.

This new data-centric approach is first used to investigate the Y-Ag-*Tr* (*Tr* = B, Al, Ga, In) ternary composition space, which is likely to contain diverse crystal chemistry but is

mostly unexplored. The machine-learning model suggests regions of the ternary diagram with a high probability for novel compounds depending on the triel element. Reducing the ternary composition space to the most probable regions of the composition diagram allows new compounds to be efficiently targeted. Indeed, high-temperature solid-state synthesis of selected compositions on these approximate phase diagrams subsequently validates the presence of a new intermetallic phase in the Y–Ag–In system. The success of this work highlights the potential of deploying machine-learning methods to speed up the discovery of novel materials by directing synthesis efforts.

5.2 Experimental Details

5.2.1 Machine-learning Model Construction

The machine-learning model was constructed using a Support Vector Regression (SVR) algorithm as implemented in Scikit-learn within Python 3.6 environment.[209] The SVR employed a radial basis function as the kernel function and was optimized using Venetian blinds cross-validation (CV) with 10-fold data splits. Hyper-parameter settings were adjusted with a grid search method, which exhaustively evaluates all parameter combinations. The searching space was defined as cost parameter (C) ranging in [1, 5, 10, 30, 50, 100] and gamma (γ) ranging in [0.001, 0.01, 0.1, 1], where C regulated the tradeoff between minimization of error and maximization of the margins and γ is the kernel parameter that controls the influence of each support vector. The source code and training data are shared in the open source Github repository at https://github.com/BrgochGroup.

5.2.2 Synthesis

The starting metals, silver (powder, 99.9%, Alfa Aesar), indium (pieces, 99.99%, Alfa Aesar), boron (crystalline pieces, 99.5%, Alfa Aesar), and yttrium (filings, 99.8%, HEFA Rare Earth) were weighed out in the desired stoichiometric ratios and ground together to form a uniform sample with a total weight of 250 mg and then pressed into pellets. The pellet size had a diameter of 6 mm and was pressed with an applied pressure of 2500 psi. The pellets were then arc-melted (Centorr Furnace) under argon gas at a current of about 50 A. To confirm homogeneity, each sample was melted at least three times, including intermittently flipping the button. The weight loss for each sample after arc-melting was <2%. The arc-melted samples were then sealed in fused silica tubes under vacuum and annealed at 850°C for ten days, followed by quenching in water. The products all had a silver luster, were brittle, and air-stable.

5.2.3 Powder X-ray Diffraction

Powder diffraction data were collected using a PanAnalytical X'Pert powder diffractometer and Cu Kα radiation (λ = 1.54183 Å) at room temperature. The samples were prepared for powder diffraction by grinding the annealed ingots using an agate mortar and pestle and then spreading the fine powder on a zero-diffraction silicon plate.

5.2.4 Single-Crystal X-ray Diffraction

Single crystals were picked from crushed ingots with the aid of an optical microscope. The data were collected using a Bruker APEX II platform diffractometer equipped with a 4K CCD APEX II detector and a Mo Kα radiation source at 296 K. Reflections were collected by using a narrow-frame algorithm with scan widths of 0.3° in ω and an exposure time of 30 s per

frame (four sets of 726 frames) and a 6 cm detector distance. The data were integrated using the Bruker Apex-II program, with the intensities corrected for Lorentz factor, polarization, air absorption, and absorption due to variation in the path length through the detector faceplate. Structure solution and refinement were carried out using the SHELXTL program package (version 6.12),[155] and refined by full-matrix least-squares on F_O^2, including anisotropic displacement parameters. The final crystal structure solutions, in CIF format, have been sent to The Cambridge Crystallographic Data Centre (CCDS) and can be obtained from the CCDC using the depository numbers: 1980533. All crystal structures were visualized using VESTA.[112]

5.2.5 SEM-EDX

Energy-dispersive X-ray spectroscopy (EDX) data were collected on the polished bulk sample and selected crystals using a JEOL JSM-6400 scanning electron microscope attached with an AMETEK EDAX Octane Pro energy dispersive X-ray spectrometer and an accelerating voltage of 15 eV and an emission current of 12 μA. To prevent the samples from tilting, a portion of the bulk ingots were mounted in epoxy resin and polished using a 1 μm diamond slurry, while the selected single crystals were mounted on carbon tape. In both cases, at least seven independent data points were analyzed on different areas of each crystal to determine the average composition.

5.2.6 Electronic and Chemical Bonding Calculations

First-principles total energy calculations on ordered models of $YAg_{0.65}In_{1.35}$ were performed using the Vienna *ab initio* simulation package (VASP).[117,118] The calculations employed a plane-wave basis set with projector augmented wave (PAW) potentials,[119] a cutoff energy of

500 eV, a 4×4×4 Γ-centered Monkhorst–Pack *k*-point grid, and a convergence criteria of 1 x 10^{-8} eV and 1 x 10^{-6} eV was set for electronic and structure relaxation, respectively.

5.3 Results and Discussion

5.3.1 Constructing Machine-Learning Formation Energy Models

A machine-learning training set was developed using 313,965 formation energies produced from high-throughput DFT calculations and contained in the Materials Project (v2019.11) database[127] and Open Quantum Materials Database (OQMD v1.3)[75]. The data were initially cleaned according to the following criteria: (i) only the lowest $\Delta E_{f,\mathrm{DFT}}$ was considered for each composition because it represents the most energetically favorable compound, (ii) compounds without a $\Delta E_{f,\mathrm{DFT}}$ were eliminated from the training set, and (iii) any compounds containing group 18 elements, Tc, or Z>83 (except for U and Th) were omitted. Additionally, for each composition diagram, any compound related to the specific ternary composition diagram being analyzed was removed from the training set to limit potential bias. After preprocessing, the data set was reduced to 279,943 compounds. This was then randomly split into five independent training (90%) and test (10%) sets. The compounds in the training set were represented with a descriptor set containing 35 distinct compositional variables along with four mathematical expressions including the difference, the average, the maximum value and the minimum value. The complete list of variables is provided in Table S5.1 of the Supporting Information. The training set with 140 total descriptors was normalized, mean-centered and rescaled to the unit variance. The SVR model employed an optimized cost parameter (C) and gamma (γ) functions of 100 and 0.01, respectively.

The model performance on the test set is plotted in Figure 5.1 with the diagonal line representing the ideal fit. After training, the model achieved a coefficient of determination

(r^2) value of 0.94 and a mean absolute error (MAE) of 0.085 eV/atom (~986 K). The most significant error occurs for compounds that have $\Delta E_f > 0$ eV/atom; however, this is not a significant concern here since positive formation energy compounds are highly unlikely to be synthesized, which is the ultimate goal of this work. The error is also comparable with a previous model developed using similar compositional descriptors with reduced-error pruning tree algorithm,[210] which achieved an MAE of 0.088 eV/atom (~1021 K). Given that the model constructed here was reliable, a composition grid containing 253 hypothetical chemical compositions within the $Y_xAg_yTr_{(1-x-y)}$, (*Tr* = B, Al, Ga, In) composition space was created by varying the value of *x* and *y* and then using the machine-learning model to predict their corresponding formation energy ($\Delta E_{f,SVR}$).

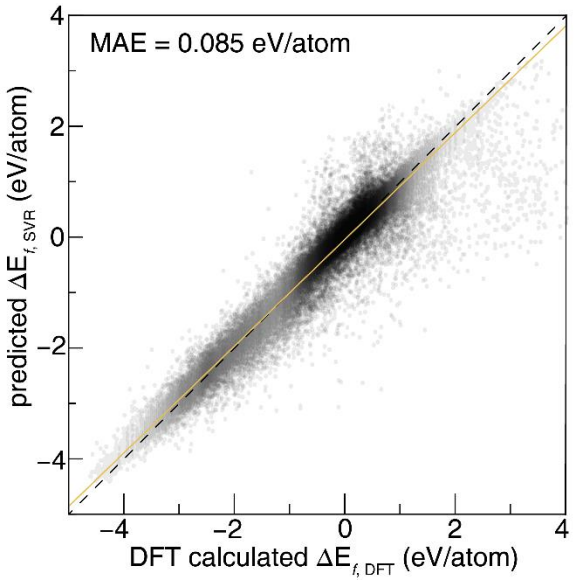

Figure 5.1. Predicted formation energy ($\Delta E_{f,SVR}$) shows excellent agreement with the DFT calculated formation energy ($\Delta E_{f,DFT}$) for 27,994 compounds in the test set (10% of the training set). Darker regions of the plot correspond to overlapping data points. The 1:1 line is shown as the black dashed line and the regression line is shown as the solid yellow line.

5.3.2 Applying Formation Energy Predictions to Identify Under-explored Composition Space

The predicted $\Delta E_{f,SVR}$ for the composition grid containing 253 compositions of each ternary system was plotted in Figure 5.2 as a contour plot. The formation energies range from −0.63 eV/atom to +0.59 eV/atom across all four data sets. To confirm the reliability of using this machine-learning model, the location of every experimentally reported compound in ICSD (Inorganic Crystal Structure Database) and PCD (Pearson's Crystal Data) was also plotted on the ternary diagrams to ensure "real" compounds exist in energetically favorable (negative) regions of the plots. The experimentally reported compounds, shown as black circles in Figure 5.2, indicate there is some correlation between the regions of the most negative formation energies (the redder regions) and the reported existence of compounds, as expected. The only notable exception occurs on the Y-Ag-B diagram for the compound AgB_2, which falls in a positive (blue region) of the composition diagram. Interestingly, this phase was only reported once in 1961, and no experimental details were included in the report.[211] We reexamined AgB_2 for this work by attempting to synthesize the phase but failed to produce any discernible results making the presence of this phase questionable.

Formation energy itself cannot serve as a sufficient criterion to predict phase formation because the more crucial limiting factor of whether a phase will form or not is the thermodynamic stability of the competing compounds. The best method for identifying the most favorable phase is constructing the convex hull.[128] Thus, the ternary convex hull for the Y-Ag-*Tr* (*Tr* = B, Al, Ga, In) systems were constructed using methodologies previously developed[212] using the grids of stoichiometric coordinates and the formation energies predicted by SVR. This is an efficient approach to construct the equilibrium facets, *e.g.*, lines

in two dimensions and triangles in three dimensions, by iteratively partitioning space until no points are outside of the convex hull. The resulting compositions residing immediately on the resulting convex hull represent the lowest formation energy phases in each ternary system at should be observed at equilibrium.

Strictly speaking compounds on a phase diagram at equilibrium should exist only for compositions on the convex hull ($E_{hull} = 0$), whereas positive values of E_{hull} indicate lower stability with respect to nearby compositions occurring on the hull and should result in decomposition to the more energetically favorable compositions. However, there are many examples of experimentally reported compounds with formation energies above E_{hull}. Indeed, this was highlighted by the convex hull analysis of the Sr and Co-doped La-Fe-O system, where $La_{0.375}Sr_{0.625}Co_{0.25}Fe_{0.75}O_3$ as a well-known commercial solid oxide fuel cell cathode material falls +47 meV/atom (~545 K) above the convex hull.[213] This was further emphasized through a previous analysis on the DFT calculated E_{hull} values of compounds contained in ICSD, which have all been experimentally synthesized, showed that more than 80% of the compounds in ICSD do not reside on E_{hull} but fall within 36 meV/atom (~417 K) of E_{hull}.[214] The significant number of materials with $E_{hull} > 0$ that can still be synthesized is likely because the formation energies are calculated at zero-Kelvin, and the experimentally reported compounds can be stabilized by any number of synthetic conditions (entropy). Taking into consideration the high-temperature synthetic routes generally used for solid-state synthesis, we deemed 50 meV/atom (~580 K) as a reasonable energetic upper threshold to determine whether or not a compound from these systems can be prepared. This additional energetic buffer should act as a small correction for making phases near (but not at) equilibrium as well as account for differences in entropy in these systems. The compositions falling in the range $0 \leq E_{hull} \leq 50$ meV/atom were therefore identified and

plotted in Figure 5.2, represented by the gray squares. These points are considered the most energetically favorable compositions and thus should have the highest probability of being experimentally obtained.

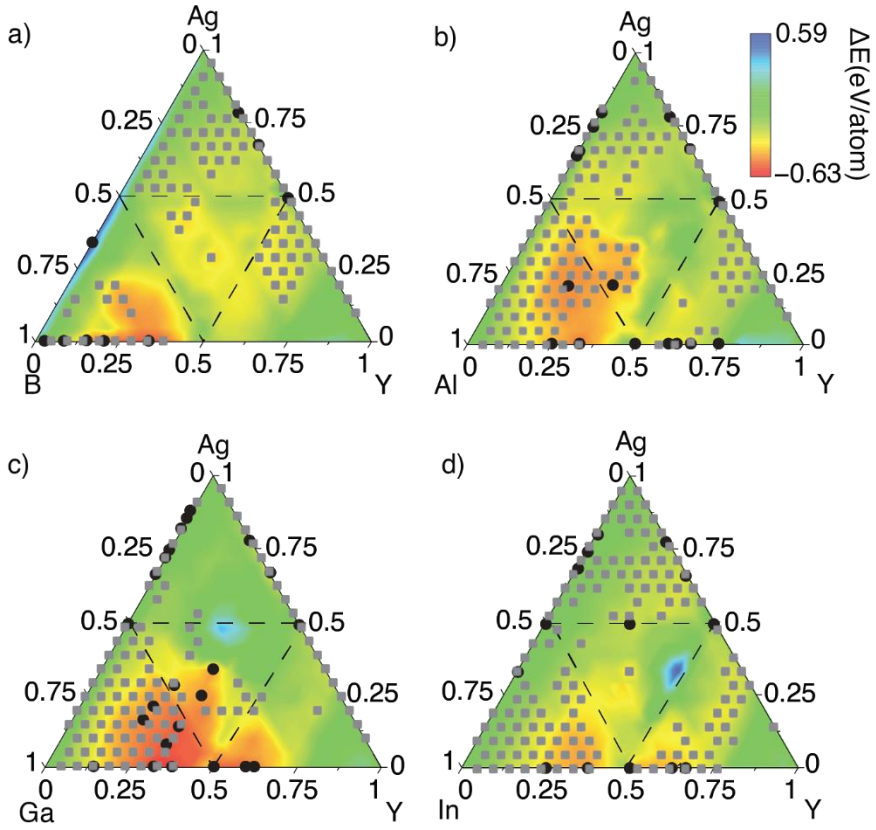

Figure 5.2. The machine learning predicted formation energy for a) Y-Ag-B, b) Y-Ag-Al, c) Y-Ag-Ga, and d) Y-Ag-In ternary systems. The most negative and positive formation energy is represented with red and blue, respectively. The gray squares represent phases with $0 \leq E_{hull} \leq 50$ meV/atom based on the convex hull analysis. All experimentally reported phases in ICSD and PCD are represented with black circles.

Analyzing these convex hull data points revealed a stronger correlation with the experimentally reported compounds compared to the plots based only $\Delta E_{f,SVR}$ alone. For example, in the Y-Ag-In ternary system, the only reported phase YAg_2In did not fall in the most energetically favorable region; however, it was located within the 50 meV/atom

threshold of the hull. Also, the predicted formation energies of the Y-Ag binary phases, including YAg, YAg_2 and $Y_{14}Ag_{51}$ did not fall into the most negative region, but based on the convex hull analysis they were all located within 50 meV/atom above the hull supporting their experimental reports. Finally, AgB_2 does not fall within the 50 meV/atom range, further supporting our difficulty in resynthesizing the phase. These observations substantiate the reliability of using E_{hull} as a criterion to evaluate whether or not a phase can form. Moreover, the results suggest that in search of intermetallic phases, a convex hull analysis is an essential tool to help us identify regions of composition space where new compounds have the highest probability of existing.

5.3.3 Data-Directed Synthesis and Crystal Structure Solution

The success of quickly analyzing composition diagrams is only valuable, provided new compounds can be identified in the unexplored regions of these plots. The prevalence of triel-rich phases in the Al and Ga composition diagrams is in agreement with machine-learning predicted E_{hull} provides strong evidence for the soundness of this approach. However, the lack of reports in the equivalent B and In containing systems, despite the expectation of phases within 50 meV/atom of the convex hull, was somewhat surprising. Therefore, the Y–Ag–B and Y-Ag-In were investigated to validate the suggestion of new compounds in the black dashed line areas. Given the suggested existence of a new phase with the stoichiometry of 1:1:1 on both ternary diagrams, this composition was selected as the first target phase. For YAgB, the arc-melted sample was poorly crystalline based on the powder X-ray diffractogram and showed the presence of binary phases. Singles crystals could not be selected using an optical microscope corroborating the poor crystallinity of the product. Additional synthetic attempts were made for the YAg_2B and Y_2AgB compositions,

where the convex hull dots are focused; however, these reactions also failed to form a ternary compound with the product consisting of only binary phases. The powder X-ray diffraction pattern for some of the loaded compositions in this ternary phase system are shown in Figures S5.1, S5.2, and S5.3. The lack of Y–Ag–B phases is likely stemming from a significant entropy component arising from high-temperature arc melting that is not accounted for in this model. Unfortunately, including entropy is not trivial owing to the computational cost of these calculations but must be addressed in future iterations of the data-driven model.

Examining the Y–Ag–In phase space started by arc-melting a sample of YAgIn, which was suggested by the convex hull, followed by analyzing the product using powder X-ray diffraction. The diffractogram revealed the presence of a minor component that indexed as the YAg_2In as well as a set of intense peaks that could not be indexed to any known phase. Following the lever-rule to avoid forming YAg_2In, subsequent synthesis was carried out moving toward the In-rich region of the composition diagram. Reducing the silver content following YAg_xIn_{2-x} showed the disappearance of the secondary phase, as expected until a pure sample was achieved when $x = 0.65$ (Figure 5.3b). Analyzing the product of $YAg_{0.65}In_{1.35}$ under an optical microscope showed the occurrence of single crystals that could be selected from the crushed bulk ingot for further analysis. The single crystal crystallographic data, refined atomic positions, equivalent isotropic displacement parameters, selected bond lengths, and anisotropic displacement parameters are provided in Table 5.1 and Table S5.2, S5.3, S5.4. According to the systematic absences, the data set indicates a primitive hexagonal lattice with two possibilities, centrosymmetric $P6/mmm$ or noncentrosymmetric $P\bar{6}m2$. Refining the structure using both space groups yielded significantly better statistics for the centrosymmetric space group. As a result, the higher symmetry group was selected,

and the compound was easily solved in the space group *P*6/*mmm* (No. 191; *Z* = 1) with the AlB_2-type structure. The refinement of the structure in $P\bar{6}m2$ is provided for comparison in Table S5.5. This well-known structure type contains two crystallographically independent positions, with Y occupying Wyckoff site 1a and the (Ag/In) statistically mixing on Wyckoff 2*d* site. The site occupancies of the latter position were fixed to reflect the nominally loaded composition $YAg_{0.65}In_{1.35}$ because of the similar X-ray scattering power between Ag and In. A semi-quantitative EDX analysis of both bulk sample and measured single crystal, Figures S5.4 and S5, verifies the composition is $Y_{0.94(4)}Ag_{0.61(9)}In_{1.48(5)}$, which is in agreement with the loaded compositions. The refined crystal structure, illustrated in Figure 5.3c, contains an infinite honeycomb network formed by (Ag/In)—(Ag/In) interactions separated 2.7650(7) Å. These layers stack along the [001] direction, separated by 3.57(6) Å. The Y atoms sit in the center of the hexagonal network with Y—(Ag/In) bonds of 2.07650(4) Å.

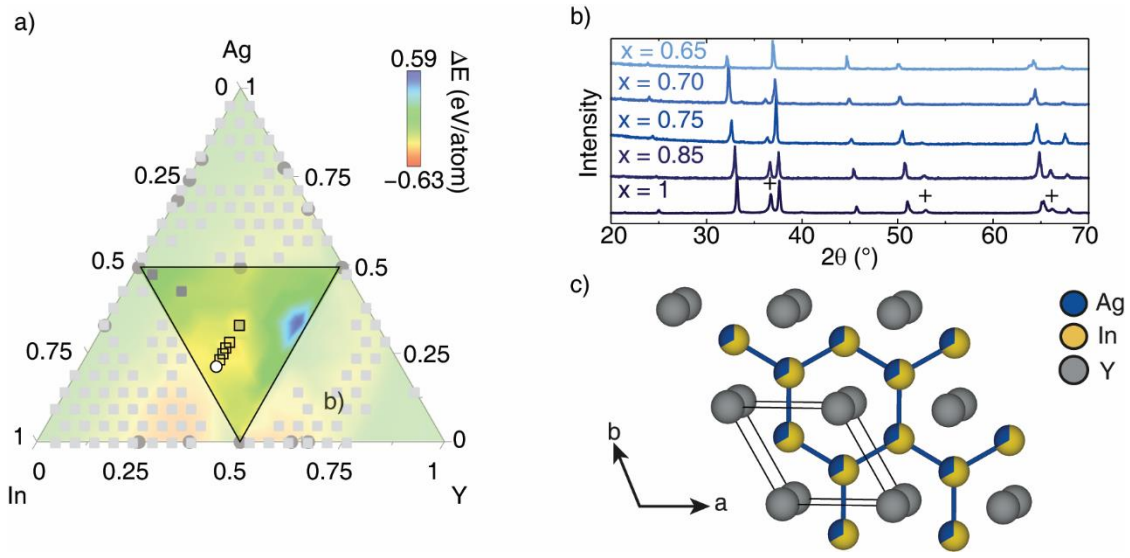

Figure 5.3. a) The predicted formation energy for Y-Ag-In ternary phase and synthesis direction. White squares indicate the compositions experimentally prepared, and the white circle is the composition of the final, phase pure product. b) X-ray powder diffraction for a series of compositions with general formula YAg_xIn_{2-x} (x = 1, 0.85, 0.75, 0.70, 0.65). The "+" sign indicates the presence of YAg_2In as the second phase. c) View of the $YAg_{0.65}In_{1.35}$ crystal structure nearly along c axis. Y, Ag, and In are shown in gray, blue, and yellow, respectively.

Table 5.1. Crystallographic data for $YAg_{0.65}In_{1.35}$ collected at 296 K

Formula	$YAg_{0.65}In_{1.35}$
mass (g mol^{-1})	314.03
space group; Z	*P*6/*mmm*; 1
a (Å)	4.801(2)
c (Å)	3.576(1)
V (Å^3)	71.38(4)
ρ_{calc} (g cm^{-3})	7.306
absorption correction	empirical
μ (mm^{-1})	35.02
θ range (deg.)	4.92-27.28
hkl ranges	-3≤ *h*≤6,
	-5 ≤ *k*≤6,
	-4≤ *l*≤3
no. reflections; R_{int}	285, 0.0120
no. unique reflections	47
no. parameters	5
$R(F)$ for $F_o^2 > 2\sigma(F_o^2)$ [a]	0.0132
$R_w(F_o^2)$ [b]	0.0282
goodness of fit	1.24
$(\Delta\rho)_{max}$, $(\Delta\rho)_{min}$ (e Å^{-3})	0.0397, –0.536

5.3.4 Crystal Structure Preference and Atomic Ordering in $YAg_{0.65}In_{1.35}$

To understand the crystal chemistry of $YAg_{0.65}In_{1.35}$, electronic structure calculations were employed, as described in the Supporting Information. Since the $YAg_{0.65}In_{1.35}$ crystal structure contains statistically mixed Ag/In position on Wyckoff 2*d* site, ordered supercell

models were created using the program "Supercell."[165] A 2x2x2 supercell was necessary to achieve the approximate chemical composition of the compound resulting in 68 separate ordered crystal structures with different distributions of Ag/In in the model. The most favorable ordered model of "$YAg_{0.65}In_{1.35}$" was then computationally determined by optimizing the hypothetical structure using DFT and comparing the relative total energies of each model. The energy differences are plotted in Figure S5.6 and show all models have remarkably similar total energies differing by <7 meV/atom, which supports statistical mixing between Ag and In.[215,216] The three lowest DFT energy structural models were then examined in greater detail to substantiate the lack of site preference in this structure further, known as the coloring problem.[217] Single crystal refinement indicates *P*6/*mmm* and $P\bar{6}m2$ are both possible space groups and differ based on the Ag and In order. First, it is possible that atoms statistically mix on all possible sites of the hexagonal network (*P*6/*mmm*). Alternatively, two possible crystallographic sites can be produced in the AlB_2-like structure with inequivalent statistically mixing on each site, where one position is filled with In and the other is filled with Ag/In ($P\bar{6}m2$). These different possibilities are clearly visualized in Figure S5.7. Analyzing the distribution among the different models shows that there is no specific site preference for the Ag or In atoms, which implies the random distribution of In and Ag in the honeycomb layer. This supports the fact centrosymmetric space group, *P*6/*mmm*, is preferred, as recommended by single crystal refinement. In addition to the ordered Supercell model calculation, the ratio of Ag/In was studied by examining the electronic structure of the parent compound, YAg_2. As plotted in Figure S5.8, YAg_2 in a hypothetical *P*6/*mmm* crystal structure (note that YAg_2 is experimentally reported in *I*4/*mmm*)[218] has 33 valence electrons causing the Fermi level to fall on a peak in the density of states. However, there is a notable pseudogap above the Fermi level falling at

35.7 valence electrons. The additional electrons necessary to shift the Fermi level to this position can be obtained by substititon an more electron-rich element like In. Calculating the ideal composition to place the Fermi level into the pseudogap results in the approximate composition, $YAg_{0.65}In_{1.35}$, which is in excellent agreement with our experimental results. This classic electronic structure analysis provides further evidence for the formation of this new compound.

5.4 Conclusion

The ever-increasing application of machine learning to materials chemistry has been proposed on numerous occasions as a viable option for novel materials discovery. In this research, a machine-learning model is developed to predict the formation energy of ternary compounds as well as constructing convex hull in the Y-Ag-*Tr* (*Tr* = B, Al, Ga, In) ternary composition space. Correlating the location of predicted compounds and the experimentally reported phases show excellent agreement indicating that the zero-kelvin machine-learning derived phase diagrams are generally reliable. Although it may not be possible to targe exact compositions that will form new crystal structures, the ability to reduce the size of a composition diagram and hone in on regions where new compounds are likely to be present is a significant advance. In this work, we use this new idea to specifically investigate ternary compounds by predicting the regions where Y-Ag-In compounds are likely to exist, leading to the discovery of a new phase, $YAg_{0.65}In_{1.35}$. This compound had not been previously reported, and by using machine learning to highlight its likely existence, the phase could be prepared using a minimal number of reactions. First-principle calculations were then carried out to identify the site preference Ag/In as well as support the refined space group

(*P*6/*mmm*). The success of this work is to present a predictive machine-learning paradigm that can be employed to screen the other ternary phase systems for novel compounds.

Author Contributions

‡ (S.L and Z.Z.) These authors contributed equally

5.5 Acknowledgments

The authors would like to thank Prof. Arnold M. Guloy and Dr. James D. Korp for their helpful discussion. The authors gratefully acknowledge the generous financial support provided by the R.A. Welch foundation (E-1981) and the Texas Center for Superconductivity at the University of Houston (TcSUH) for supporting this research. This research used the Maxwell/Opuntia/Sabine cluster(s) operated by the Research Computing Data Core at the University of Houston.

Supporting Information

Table S5.1. Compositional descriptors for predicting the formation energy (ΔE)

Atomic number	Number of valence electrons
Atomic weight	Gilman number of valence electrons
Period number	Number of s electrons
Group number	Number of p electrons
Family number	Number of d electrons
Mendeleev number	Number of outer shell electrons
Atomic radius	First ionization energy
Covalent radius	Polarizability
Zunger radius	Melting point
Ionic radius	Boiling point
Crystal radius	Density
Pauling EN	Specific heat
Martynov-Batsanov EN	Heat of fusion
Gordy EN	Heat of vaporization
Mulliken EN	Thermal conductivity
Allred-Rochow EN	Heat atomization
Metallic valence	Cohesive energy
Electron affinity	

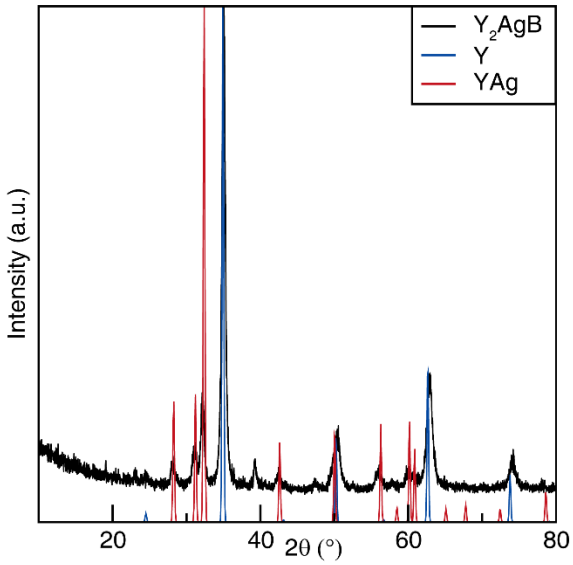

Figure S5.1. The powder X-ray diffraction pattern of Y_2AgB composition. The black lines, red lines, and blue lines indicate Y_2AgB, YAg, and Y, respectively.

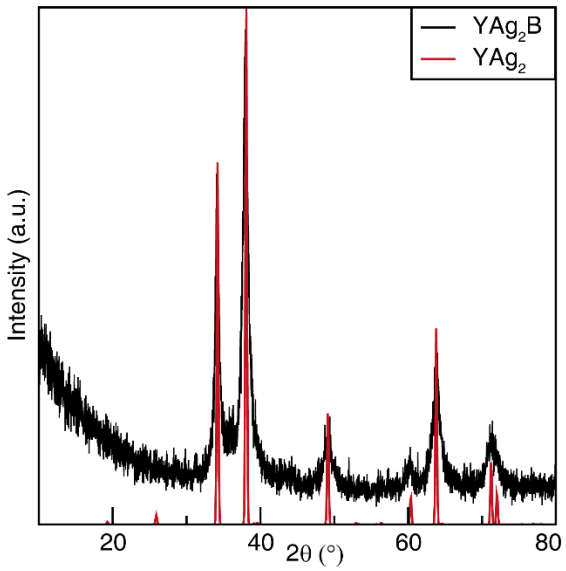

Figure S5.2. The powder X-ray diffraction pattern of YAg_2B composition. The black lines and red lines indicate YAg_2.

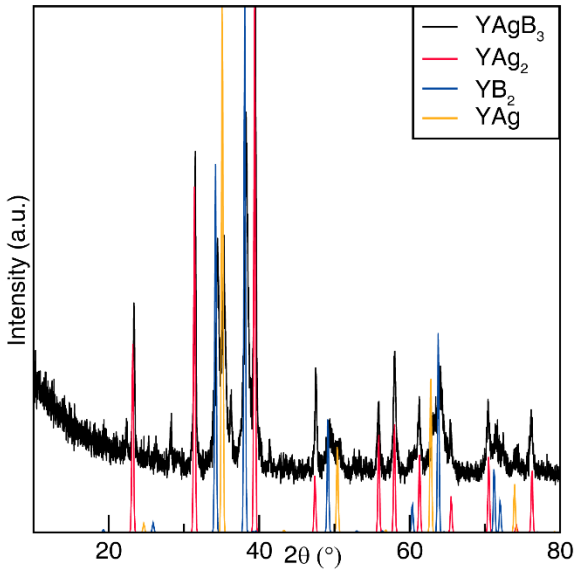

Figure S5.3. The powder X-ray diffraction pattern of $YAgB_3$ composition. The black lines, red lines, yellow lines, and blue lines indicate $YAgB_3$, YAg_2, YAg, and YB_2, respectively.

Table S5.2. Equivalent isotropic displacement parameters for $YAg_{0.65}In_{1.35}$

atom	Wyck. site	Occ.	x	y	z	U_{eq} (Å^2)[a]
Y	1a	1	0	0	0	0.0108(4)
Ag	2d	0.325	0.666	0.333	0.5	0.0222(4)
In	2d	0.675	0.666	0.333	0.5	0.0222(4)

[a] U_{eq} is defined as one-third of the trace of the orthogonalized U_{ij} tensor.

Table S5.3. Selected bond length for $YAu_{0.65}In_{1.35}$

	$YAg_{0.65}In_{1.35}$
Y−*M*[a]	3.2984(9) Å
M−*M*	2.772(1) Å
Y−Y	3.576(3) Å
M−*M*	2.7489(8) Å

[a]*M* = Ag/In

Table S5.4. Anisotropic displacement parameters (Å^2) for $YAu_{0.65}In_{1.35}$

Atom	U_{11}	U_{22}	U_{33}	U_{23}	U_{13}	U_{12}
Y	0.0124(4)	0.0124(4)	0.0077(7)	0	0	0.0062(2)
Ag	0.0078(3)	0.0078(3)	0.0509(7)	0	0	0.0039(2)
In	0.0078(3)	0.0078(3)	0.0509(7)	0	0	0.0039(2)

Table S5.5. Crystallographic data for $YAg_{0.65}In_{1.35}$ collected at 296 K

Formula	$YAg_{0.65}In_{1.35}$
mass (g mol^{-1})	314.03
space group; Z	$P\bar{6}m2$; 1
a (Å)	4.801(2)
c (Å)	3.576(1)
V (Å^3)	71.38(4)
ρ_{calc} (g cm^{-3})	7.306
absorption correction	empirical
μ (mm^{-1})	35.02
θ range (deg.)	4.92-27.28
hkl ranges	$-3 \leq h \leq 6$, $-5 \leq k \leq 6$, $-4 \leq l \leq 3$
no. reflections; R_{int}	350, 0.0116
no. unique reflections	80
no. parameters	8
$R(F)$ for $F_o^2 > 2\sigma(F_o^2)$ [a]	0.0155
$R_w(F_o^2)$ [b]	0.0363
goodness of fit	0.0774
$(\Delta\rho)_{max}$, $(\Delta\rho)_{min}$ (e Å^{-3})	0.0447, –0.561

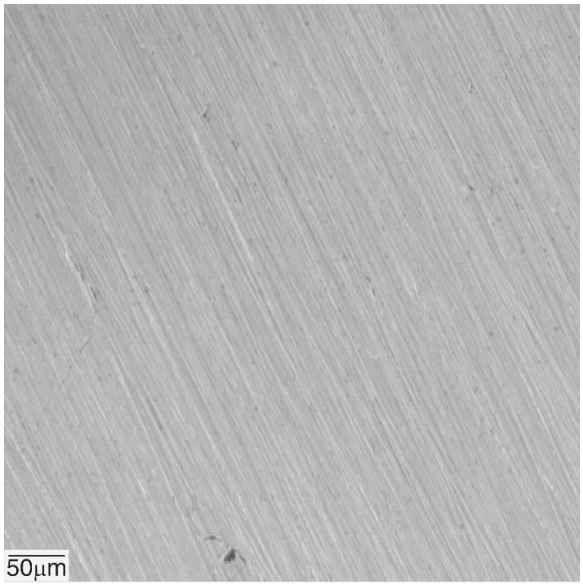

Figure S5.4. SEM-EDX analysis on the bulk sample of $YAg_{0.65}In_{1.35}$

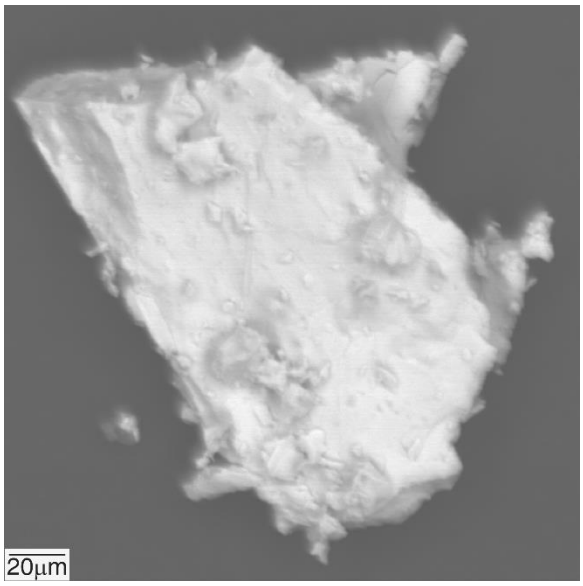

Figure S5.5. SEM-EDX analysis on the single crystal of $YAg_{0.65}In_{1.35}$

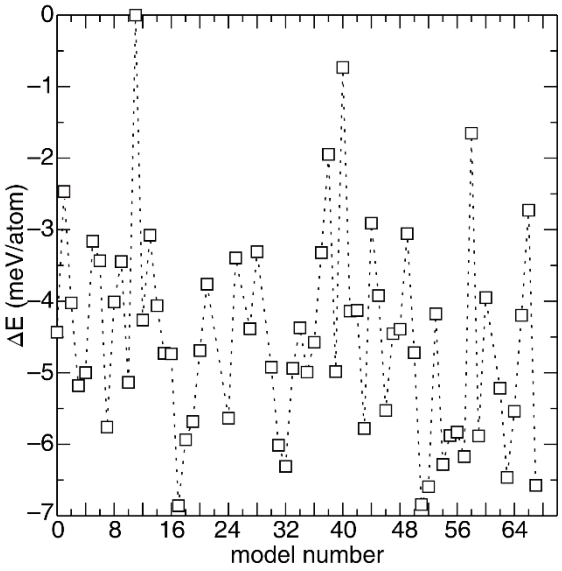

Figure S5.6. The ΔE of 68 ordered crystal structures generated by Supercell

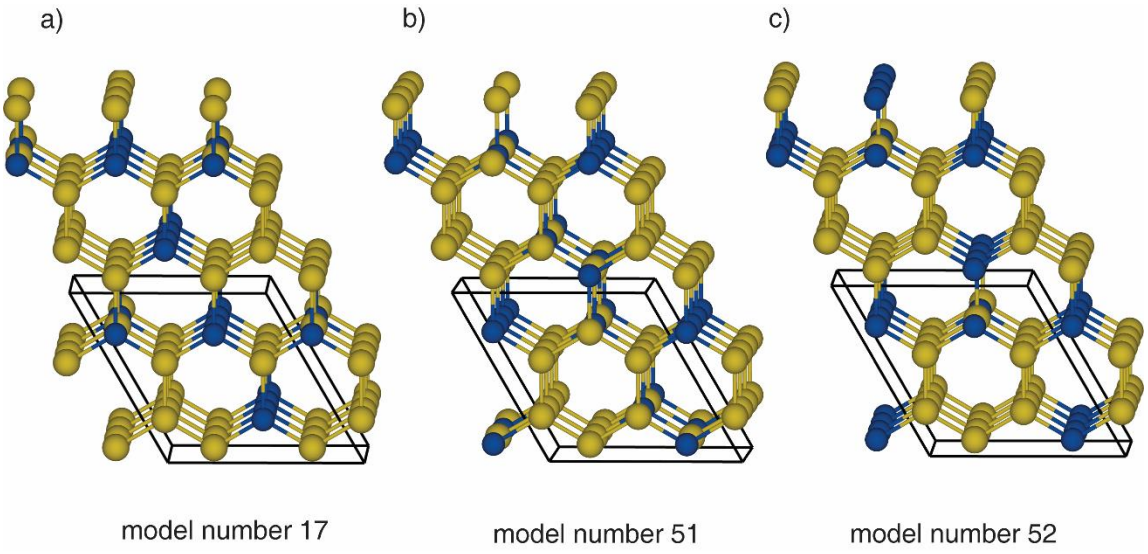

Figure S5.7. The three lowest total energy models for $YAg_{0.65}In_{1.35}$. In and Ag are drawn with yellow and blue, respectively.

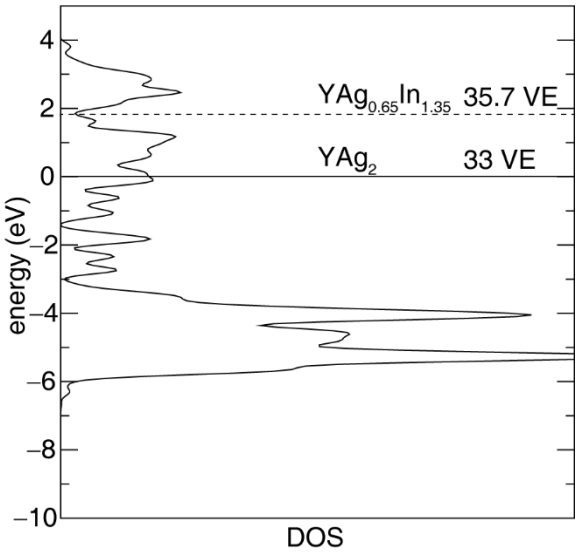

Figure S5.8. The DOS of YAg_2 with *P*6/*mmm* crystal structure. The Fermi level is set at 0 eV. By adding In to the structure ($YAg_{0.65}In_{1.35}$), the Fermi level moves up and falls into the psuedogap (the dashed line).

Table S5.6. Machine-learning predicted formation energy versus compositions for Y-Ag-B ternary phase system

composition	energy	composition	energy	composition	energy
Y0Ag1B20	0.3317844	Y1Ag19B1	-0.05137	Y4Ag0B17	-0.579864
Y0Ag2B19	0.3709617	Y1Ag20B0	-0.077122	Y4Ag1B16	-0.42279
Y0Ag3B18	0.4336028	Y2Ag0B19	-0.292813	Y4Ag2B15	-0.488747
Y0Ag4B17	0.6244142	Y2Ag1B18	-0.256488	Y4Ag3B14	-0.50075
Y0Ag5B16	1.3241507	Y2Ag3B16	-0.277473	Y4Ag5B12	-0.396551
Y0Ag6B15	1.0510089	Y2Ag4B15	-0.352006	Y4Ag6B11	-0.307871
Y0Ag7B14	0.7332951	Y2Ag5B14	-0.333801	Y4Ag7B10	-0.181074
Y0Ag8B13	0.7712275	Y2Ag6B13	-0.244715	Y4Ag8B9	-0.174999
Y0Ag9B12	0.9059931	Y2Ag7B12	-0.234497	Y4Ag9B8	-0.244652
Y0Ag10B11	0.9340268	Y2Ag8B11	-0.197284	Y4Ag10B7	-0.177085
Y0Ag11B10	0.7110436	Y2Ag9B10	-0.09235	Y4Ag11B6	-0.220141
Y0Ag12B9	0.6668837	Y2Ag10B9	-0.085212	Y4Ag12B5	-0.174543
Y0Ag13B8	0.5577221	Y2Ag11B8	-0.197459	Y4Ag13B4	-0.210746
Y0Ag14B7	0.50476	Y2Ag12B7	-0.156391	Y4Ag14B3	-0.19643
Y0Ag15B6	0.4814413	Y2Ag13B6	-0.150995	Y4Ag15B2	-0.180936
Y0Ag16B5	0.6452752	Y2Ag14B5	-0.121935	Y4Ag16B1	-0.179912
Y0Ag17B4	0.4232955	Y2Ag15B4	-0.140644	Y4Ag17B0	-0.135663
Y0Ag18B3	0.3676468	Y2Ag16B3	-0.126927	Y5Ag0B16	0.1119208
Y0Ag19B2	0.3460414	Y2Ag17B2	-0.127279	Y5Ag1B15	-0.434794
Y0Ag20B1	0.3284547	Y2Ag18B1	-0.106481	Y5Ag2B14	-0.508128
Y0Ag21B0	0	Y2Ag19B0	-0.095058	Y5Ag3B13	-0.479326
Y1Ag0B20	-0.227355	Y3Ag0B18	-0.448526	Y5Ag4B12	-0.466086
Y1Ag2B18	-0.185277	Y3Ag1B17	-0.43224	Y5Ag6B10	-0.211076
Y1Ag3B17	-0.163453	Y3Ag2B16	-0.416962	Y5Ag7B9	-0.204449
Y1Ag4B16	-0.104633	Y3Ag4B14	-0.479871	Y5Ag8B8	-0.122343
Y1Ag5B15	-0.172548	Y3Ag5B13	-0.393014	Y5Ag9B7	-0.220065
Y1Ag6B14	-0.171596	Y3Ag6B12	-0.321099	Y5Ag10B6	-0.204256
Y1Ag7B13	-0.161104	Y3Ag7B11	-0.31624	Y5Ag11B5	-0.199508
Y1Ag8B12	-0.158526	Y3Ag8B10	-0.122807	Y5Ag12B4	-0.222828
Y1Ag9B11	-0.162586	Y3Ag9B9	-0.135916	Y5Ag13B3	-0.213093
Y1Ag10B10	-0.14158	Y3Ag10B8	-0.170961	Y5Ag14B2	-0.214924
Y1Ag11B9	-0.147765	Y3Ag11B7	-0.21819	Y5Ag15B1	-0.241615
Y1Ag12B8	-0.133487	Y3Ag12B6	-0.177647	Y5Ag16B0	-0.190551
Y1Ag13B7	-0.128847	Y3Ag13B5	-0.162134	Y6Ag0B15	-0.498344
Y1Ag14B6	-0.10814	Y3Ag14B4	-0.175052	Y6Ag1B14	-0.515796
Y1Ag15B5	-0.063175	Y3Ag15B3	-0.171821	Y6Ag2B13	-0.491963
Y1Ag16B4	-0.04996	Y3Ag16B2	-0.152785	Y6Ag3B12	-0.452426
Y1Ag17B3	-0.096811	Y3Ag17B1	-0.122044	Y6Ag4B11	-0.373413
Y1Ag18B2	-0.066951	Y3Ag18B0	-0.119569	Y6Ag5B10	-0.235532

Table S5.6. continued from previous page

Y6Ag7B8	-0.21354	Y9Ag6B6	-0.316612	Y13Ag4B4	-0.303762
Y6Ag8B7	-0.261328	Y9Ag7B5	-0.325425	Y13Ag5B3	-0.280793
Y6Ag9B6	-0.234706	Y9Ag8B4	-0.278323	Y13Ag6B2	-0.264308
Y6Ag10B5	-0.200091	Y9Ag10B2	-0.1542	Y13Ag7B1	-0.241924
Y6Ag11B4	-0.253086	Y9Ag11B1	-0.186395	Y13Ag8B0	-0.265361
Y6Ag12B3	-0.241543	Y9Ag12B0	-0.231492	Y14Ag0B7	-0.130643
Y6Ag13B2	-0.225059	Y10Ag0B11	-0.153258	Y14Ag1B6	-0.23806
Y6Ag14B1	-0.184065	Y10Ag1B10	-0.115374	Y14Ag2B5	-0.191829
Y6Ag15B0	-0.209545	Y10Ag2B9	-0.207978	Y14Ag3B4	-0.251299
Y7Ag0B14	-0.593587	Y10Ag3B8	-0.29594	Y14Ag4B3	-0.251675
Y7Ag1B13	-0.483368	Y10Ag4B7	-0.224003	Y14Ag5B2	-0.223697
Y7Ag2B12	-0.452962	Y10Ag5B6	-0.227757	Y14Ag6B1	-0.206108
Y7Ag3B11	-0.403855	Y10Ag6B5	-0.266407	Y14Ag7B0	-0.262361
Y7Ag4B10	-0.14464	Y10Ag7B4	-0.297085	Y15Ag0B6	-0.070166
Y7Ag5B9	-0.198184	Y10Ag8B3	-0.333367	Y15Ag1B5	-0.125222
Y7Ag6B8	-0.216947	Y10Ag9B2	-0.289264	Y15Ag2B4	-0.183806
Y7Ag8B6	-0.300022	Y10Ag11B0	-0.238713	Y15Ag3B3	-0.192959
Y7Ag9B5	-0.246626	Y11Ag0B10	-0.019317	Y15Ag4B2	-0.157714
Y7Ag10B4	-0.160337	Y11Ag1B9	-0.243929	Y15Ag5B1	-0.133235
Y7Ag11B3	-0.232814	Y11Ag2B8	-0.297688	Y15Ag6B0	-0.126888
Y7Ag12B2	-0.201992	Y11Ag3B7	-0.300648	Y16Ag0B5	0.3710955
Y7Ag13B1	-0.163375	Y11Ag4B6	-0.315478	Y16Ag1B4	0.1070082
Y7Ag14B0	-0.301607	Y11Ag5B5	-0.316156	Y16Ag2B3	0.0441176
Y8Ag0B13	-0.505091	Y11Ag6B4	-0.333374	Y16Ag3B2	0.0183147
Y8Ag1B12	-0.416443	Y11Ag7B3	-0.342711	Y16Ag4B1	0.0154432
Y8Ag2B11	-0.379377	Y11Ag8B2	-0.341986	Y16Ag5B0	0.0384906
Y8Ag3B10	-0.231413	Y11Ag9B1	-0.260222	Y17Ag0B4	0.241084
Y8Ag4B9	-0.231013	Y11Ag10B0	-0.331543	Y17Ag1B3	0.0609128
Y8Ag5B8	-0.265072	Y12Ag0B9	-0.075956	Y17Ag2B2	0.0457896
Y8Ag6B7	-0.35021	Y12Ag1B8	-0.234133	Y17Ag3B1	0.0437291
Y8Ag7B6	-0.368737	Y12Ag2B7	-0.271329	Y17Ag4B0	0.0333603
Y8Ag9B4	-0.190148	Y12Ag3B6	-0.29502	Y18Ag0B3	0.1491086
Y8Ag10B3	-0.201702	Y12Ag4B5	-0.286178	Y18Ag1B2	0.0450083
Y8Ag11B2	-0.223654	Y12Ag5B4	-0.323839	Y18Ag2B1	0.0563918
Y8Ag12B1	-0.182615	Y12Ag6B3	-0.322442	Y18Ag3B0	0.0636208
Y8Ag13B0	-0.223503	Y12Ag7B2	-0.292204	Y19Ag0B2	0.1615488
Y9Ag0B12	-0.344179	Y12Ag8B1	-0.25607	Y19Ag1B1	0.2333899
Y9Ag1B11	-0.287847	Y12Ag9B0	-0.319636	Y19Ag2B0	0.0730766
Y9Ag2B10	-0.194199	Y13Ag0B8	-0.119521	Y20Ag0B1	0.2490385
Y9Ag3B9	-0.271525	Y13Ag1B7	-0.25868	Y20Ag1B0	0.1667479
Y9Ag4B8	-0.294756	Y13Ag2B6	-0.265022	Y21Ag0B0	0
Y9Ag5B7	-0.294439	Y13Ag3B5	-0.243433	Y0Ag0B21	0

Table S5.6. continued from previous page

Y1Ag1B19	-0.151818	Y5Ag5B11	-0.359509	Y9Ag9B3	-0.334225
Y2Ag2B17	-0.312663	Y6Ag6B9	-0.232818	Y10Ag10B1	-0.223783
Y3Ag3B15	-0.460768	Y7Ag7B7	-0.089846		
Y4Ag4B13	-0.461991	Y8Ag8B5	-0.258812		

Table S5.7. Machine-learning predicted formation energy versus compositions for Y-Ag-Al ternary phase system

composition	energy	composition	energy	composition	energy
Y0Ag1Al20	0.0155712	Y1Ag19Al1	-0.159679	Y4Ag0Al17	-0.362298
Y0Ag2Al19	-0.05245	Y1Ag20Al0	-0.064501	Y4Ag1Al16	-0.400418
Y0Ag3Al18	-0.049994	Y2Ag0Al19	-0.221541	Y4Ag2Al15	-0.451224
Y0Ag4Al17	-0.064353	Y2Ag1Al18	-0.271077	Y4Ag3Al14	-0.502892
Y0Ag5Al16	-0.034411	Y2Ag3Al16	-0.340574	Y4Ag5Al12	-0.481321
Y0Ag6Al15	-0.126426	Y2Ag4Al15	-0.393407	Y4Ag6Al11	-0.475336
Y0Ag7Al14	-0.111883	Y2Ag5Al14	-0.406939	Y4Ag7Al10	-0.431139
Y0Ag8Al13	-0.115772	Y2Ag6Al13	-0.424131	Y4Ag8Al9	-0.451396
Y0Ag9Al12	-0.105177	Y2Ag7Al12	-0.421069	Y4Ag9Al8	-0.419774
Y0Ag10Al11	-0.08452	Y2Ag8Al11	-0.43227	Y4Ag10Al7	-0.392138
Y0Ag11Al10	-0.024682	Y2Ag9Al10	-0.397738	Y4Ag11Al6	-0.338942
Y0Ag12Al9	-0.056162	Y2Ag10Al9	-0.308157	Y4Ag12Al5	-0.323742
Y0Ag13Al8	-0.073233	Y2Ag11Al8	-0.33956	Y4Ag13Al4	-0.274616
Y0Ag14Al7	-0.079048	Y2Ag12Al7	-0.33319	Y4Ag14Al3	-0.29035
Y0Ag15Al6	-0.084421	Y2Ag13Al6	-0.298898	Y4Ag15Al2	-0.272423
Y0Ag16Al5	-0.047853	Y2Ag14Al5	-0.279838	Y4Ag16Al1	-0.240855
Y0Ag17Al4	-0.045899	Y2Ag15Al4	-0.217802	Y4Ag17Al0	-0.197014
Y0Ag18Al3	-0.006554	Y2Ag16Al3	-0.222041	Y5Ag0Al16	-0.439103
Y0Ag19Al2	-0.00187	Y2Ag17Al2	-0.203791	Y5Ag1Al15	-0.44932
Y0Ag20Al1	0.0247846	Y2Ag18Al1	-0.188188	Y5Ag2Al14	-0.486194
Y0Ag21Al0	0	Y2Ag19Al0	-0.111048	Y5Ag3Al13	-0.501901
Y1Ag0Al20	-0.109351	Y3Ag0Al18	-0.312731	Y5Ag4Al12	-0.500137
Y1Ag2Al18	-0.233189	Y3Ag1Al17	-0.354613	Y5Ag6Al10	-0.45541
Y1Ag3Al17	-0.278295	Y3Ag2Al16	-0.393276	Y5Ag7Al9	-0.463546
Y1Ag4Al16	-0.325109	Y3Ag4Al14	-0.484137	Y5Ag8Al8	-0.443886
Y1Ag5Al15	-0.362173	Y3Ag5Al13	-0.468813	Y5Ag9Al7	-0.404837
Y1Ag6Al14	-0.35208	Y3Ag6Al12	-0.45697	Y5Ag10Al6	-0.398823
Y1Ag7Al13	-0.358579	Y3Ag7Al11	-0.462469	Y5Ag11Al5	-0.365434
Y1Ag8Al12	-0.367818	Y3Ag8Al10	-0.402107	Y5Ag12Al4	-0.321062
Y1Ag9Al11	-0.38711	Y3Ag9Al9	-0.406039	Y5Ag13Al3	-0.323098
Y1Ag10Al10	-0.380294	Y3Ag10Al8	-0.342975	Y5Ag14Al2	-0.29085
Y1Ag11Al9	-0.29957	Y3Ag11Al7	-0.350848	Y5Ag15Al1	-0.244745
Y1Ag12Al8	-0.293543	Y3Ag12Al6	-0.315625	Y5Ag16Al0	-0.184518
Y1Ag13Al7	-0.280335	Y3Ag13Al5	-0.304155	Y6Ag0Al15	-0.477122
Y1Ag14Al6	-0.262627	Y3Ag14Al4	-0.257188	Y6Ag1Al14	-0.508405
Y1Ag15Al5	-0.223669	Y3Ag15Al3	-0.249791	Y6Ag2Al13	-0.506156
Y1Ag16Al4	-0.208229	Y3Ag16Al2	-0.246346	Y6Ag3Al12	-0.50128
Y1Ag17Al3	-0.210617	Y3Ag17Al1	-0.228064	Y6Ag4Al11	-0.495643
Y1Ag18Al2	-0.184727	Y3Ag18Al0	-0.122467	Y6Ag5Al10	-0.441029

Table S5.7. continued from previous page

Y6Ag7Al8	-0.45887	Y9Ag6Al6	-0.456408	Y13Ag4Al4	-0.351398
Y6Ag8Al7	-0.399134	Y9Ag7Al5	-0.441116	Y13Ag5Al3	-0.34124
Y6Ag9Al6	-0.406486	Y9Ag8Al4	-0.422017	Y13Ag6Al2	-0.345727
Y6Ag10Al5	-0.405799	Y9Ag10Al2	-0.34469	Y13Ag7Al1	-0.36242
Y6Ag11Al4	-0.332289	Y9Ag11Al1	-0.32731	Y13Ag8Al0	-0.304646
Y6Ag12Al3	-0.331978	Y9Ag12Al0	-0.272951	Y14Ag0Al7	-0.340991
Y6Ag13Al2	-0.317721	Y10Ag0Al11	-0.462641	Y14Ag1Al6	-0.356193
Y6Ag14Al1	-0.290065	Y10Ag1Al10	-0.422301	Y14Ag2Al5	-0.304879
Y6Ag15Al0	-0.183978	Y10Ag2Al9	-0.415217	Y14Ag3Al4	-0.297901
Y7Ag0Al14	-0.533779	Y10Ag3Al8	-0.394716	Y14Ag4Al3	-0.320569
Y7Ag1Al13	-0.498415	Y10Ag4Al7	-0.413661	Y14Ag5Al2	-0.294616
Y7Ag2Al12	-0.492895	Y10Ag5Al6	-0.423575	Y14Ag6Al1	-0.284455
Y7Ag3Al11	-0.48992	Y10Ag6Al5	-0.444861	Y14Ag7Al0	-0.262813
Y7Ag4Al10	-0.393995	Y10Ag7Al4	-0.429697	Y15Ag0Al6	-0.294615
Y7Ag5Al9	-0.457978	Y10Ag8Al3	-0.371379	Y15Ag1Al5	-0.284464
Y7Ag6Al8	-0.467093	Y10Ag9Al2	-0.399777	Y15Ag2Al4	-0.265266
Y7Ag8Al6	-0.39654	Y10Ag11Al0	-0.275404	Y15Ag3Al3	-0.262708
Y7Ag9Al5	-0.39337	Y11Ag0Al10	-0.417059	Y15Ag4Al2	-0.268266
Y7Ag10Al4	-0.363442	Y11Ag1Al9	-0.419276	Y15Ag5Al1	-0.237798
Y7Ag11Al3	-0.348938	Y11Ag2Al8	-0.420091	Y15Ag6Al0	-0.157129
Y7Ag12Al2	-0.327237	Y11Ag3Al7	-0.428981	Y16Ag0Al5	-0.168168
Y7Ag13Al1	-0.319725	Y11Ag4Al6	-0.419608	Y16Ag1Al4	-0.144593
Y7Ag14Al0	-0.309936	Y11Ag5Al5	-0.414385	Y16Ag2Al3	-0.14272
Y8Ag0Al13	-0.489061	Y11Ag6Al4	-0.404279	Y16Ag3Al2	-0.143511
Y8Ag1Al12	-0.484797	Y11Ag7Al3	-0.400521	Y16Ag4Al1	-0.115043
Y8Ag2Al11	-0.478643	Y11Ag8Al2	-0.395536	Y16Ag5Al0	0.0191122
Y8Ag3Al10	-0.406148	Y11Ag9Al1	-0.391907	Y17Ag0Al4	0.3310909
Y8Ag4Al9	-0.419356	Y11Ag10Al0	-0.336094	Y17Ag1Al3	0.0199765
Y8Ag5Al8	-0.487205	Y12Ag0Al9	-0.394787	Y17Ag2Al2	-0.034298
Y8Ag6Al7	-0.450947	Y12Ag1Al8	-0.405155	Y17Ag3Al1	-0.034134
Y8Ag7Al6	-0.440737	Y12Ag2Al7	-0.400923	Y17Ag4Al0	0.0494431
Y8Ag9Al4	-0.380685	Y12Ag3Al6	-0.400226	Y18Ag0Al3	0.2789786
Y8Ag10Al3	-0.329616	Y12Ag4Al5	-0.390903	Y18Ag1Al2	0.0328714
Y8Ag11Al2	-0.336446	Y12Ag5Al4	-0.376731	Y18Ag2Al1	0.0026755
Y8Ag12Al1	-0.31303	Y12Ag6Al3	-0.376789	Y18Ag3Al0	0.0443565
Y8Ag13Al0	-0.284405	Y12Ag7Al2	-0.370883	Y19Ag0Al2	0.2709971
Y9Ag0Al12	-0.465512	Y12Ag8Al1	-0.371063	Y19Ag1Al1	0.0288897
Y9Ag1Al11	-0.466047	Y12Ag9Al0	-0.326838	Y19Ag2Al0	0.0806446
Y9Ag2Al10	-0.415789	Y13Ag0Al8	-0.375565	Y20Ag0Al1	0.2253222
Y9Ag3Al9	-0.42698	Y13Ag1Al7	-0.393771	Y20Ag1Al0	0.0833547
Y9Ag4Al8	-0.44832	Y13Ag2Al6	-0.380507	Y21Ag0Al0	0
Y9Ag5Al7	-0.418747	Y13Ag3Al5	-0.329343	Y0Ag0Al21	0

Table S5.7. continued from previous page

Y1Ag1Al19	-0.213539	Y5Ag5Al11	-0.495458	Y9Ag9Al3	-0.343722
Y2Ag2Al17	-0.30611	Y6Ag6Al9	-0.467716	Y10Ag10Al1	-0.365691
Y3Ag3Al15	-0.449096	Y7Ag7Al7	-0.467734		
Y4Ag4Al13	-0.495969	Y8Ag8Al5	-0.411473		

Table S5.8. Machine-learning predicted formation energy versus compositions for Y-Ag-Ga ternary phase system

composition	energy	composition	energy	composition	energy
Y0Ag1Ga20	0.0211042	Y1Ag19Ga1	-0.095905	Y4Ag0Ga17	-0.368745
Y0Ag2Ga19	0.0027272	Y1Ag20Ga0	-0.092221	Y4Ag1Ga16	-0.381336
Y0Ag3Ga18	-0.006898	Y2Ag0Ga19	-0.227693	Y4Ag2Ga15	-0.457291
Y0Ag4Ga17	-0.020337	Y2Ag1Ga18	-0.237964	Y4Ag3Ga14	-0.479766
Y0Ag5Ga16	-0.004332	Y2Ag3Ga16	-0.29364	Y4Ag5Ga12	-0.491603
Y0Ag6Ga15	-0.02507	Y2Ag4Ga15	-0.318664	Y4Ag6Ga11	-0.478186
Y0Ag7Ga14	-0.034982	Y2Ag5Ga14	-0.333794	Y4Ag7Ga10	-0.371358
Y0Ag8Ga13	-0.043297	Y2Ag6Ga13	-0.301649	Y4Ag8Ga9	-0.387832
Y0Ag9Ga12	-0.025283	Y2Ag7Ga12	-0.2875	Y4Ag9Ga8	-0.368475
Y0Ag10Ga11	-0.003034	Y2Ag8Ga11	-0.269007	Y4Ag10Ga7	-0.330486
Y0Ag11Ga10	0.0203859	Y2Ag9Ga10	-0.229756	Y4Ag11Ga6	-0.325742
Y0Ag12Ga9	-0.02445	Y2Ag10Ga9	-0.205838	Y4Ag12Ga5	-0.304523
Y0Ag13Ga8	-0.050054	Y2Ag11Ga8	-0.23053	Y4Ag13Ga4	-0.296797
Y0Ag14Ga7	-0.046872	Y2Ag12Ga7	-0.242256	Y4Ag14Ga3	-0.309135
Y0Ag15Ga6	-0.041329	Y2Ag13Ga6	-0.24066	Y4Ag15Ga2	-0.290666
Y0Ag16Ga5	-0.02487	Y2Ag14Ga5	-0.213816	Y4Ag16Ga1	-0.240327
Y0Ag17Ga4	-0.007681	Y2Ag15Ga4	-0.195921	Y4Ag17Ga0	-0.202401
Y0Ag18Ga3	-0.016988	Y2Ag16Ga3	-0.163891	Y5Ag0Ga16	-0.342259
Y0Ag19Ga2	-0.015169	Y2Ag17Ga2	-0.14845	Y5Ag1Ga15	-0.472213
Y0Ag20Ga1	0.0066724	Y2Ag18Ga1	-0.107379	Y5Ag2Ga14	-0.499552
Y0Ag21Ga0	0	Y2Ag19Ga0	-0.110863	Y5Ag3Ga13	-0.49954
Y1Ag0Ga20	-0.163951	Y3Ag0Ga18	-0.323434	Y5Ag4Ga12	-0.517243
Y1Ag2Ga18	-0.186709	Y3Ag1Ga17	-0.318512	Y5Ag6Ga10	-0.451163
Y1Ag3Ga17	-0.207931	Y3Ag2Ga16	-0.346509	Y5Ag7Ga9	-0.442734
Y1Ag4Ga16	-0.224447	Y3Ag4Ga14	-0.448893	Y5Ag8Ga8	-0.402224
Y1Ag5Ga15	-0.252589	Y3Ag5Ga13	-0.436707	Y5Ag9Ga7	-0.351016
Y1Ag6Ga14	-0.262674	Y3Ag6Ga12	-0.415365	Y5Ag10Ga6	-0.367526
Y1Ag7Ga13	-0.262322	Y3Ag7Ga11	-0.386446	Y5Ag11Ga5	-0.354683
Y1Ag8Ga12	-0.262046	Y3Ag8Ga10	-0.303041	Y5Ag12Ga4	-0.355241
Y1Ag9Ga11	-0.243392	Y3Ag9Ga9	-0.336269	Y5Ag13Ga3	-0.336834
Y1Ag10Ga10	-0.213732	Y3Ag10Ga8	-0.277174	Y5Ag14Ga2	-0.326735
Y1Ag11Ga9	-0.206809	Y3Ag11Ga7	-0.301621	Y5Ag15Ga1	-0.301887
Y1Ag12Ga8	-0.210375	Y3Ag12Ga6	-0.290233	Y5Ag16Ga0	-0.212324
Y1Ag13Ga7	-0.205291	Y3Ag13Ga5	-0.26229	Y6Ag0Ga15	-0.5209
Y1Ag14Ga6	-0.195662	Y3Ag14Ga4	-0.263907	Y6Ag1Ga14	-0.513599
Y1Ag15Ga5	-0.193899	Y3Ag15Ga3	-0.252589	Y6Ag2Ga13	-0.518126
Y1Ag16Ga4	-0.161149	Y3Ag16Ga2	-0.199023	Y6Ag3Ga12	-0.524777
Y1Ag17Ga3	-0.14778	Y3Ag17Ga1	-0.190075	Y6Ag4Ga11	-0.544253
Y1Ag18Ga2	-0.129401	Y3Ag18Ga0	-0.152665	Y6Ag5Ga10	-0.467141

Table S5.8. continued from previous page

Y6Ag7Ga8	-0.456223	Y9Ag7Ga5	-0.361465	Y13Ag6Ga2	-0.332902
Y6Ag8Ga7	-0.363804	Y9Ag8Ga4	-0.315006	Y13Ag7Ga1	-0.319962
Y6Ag9Ga6	-0.374886	Y9Ag10Ga2	-0.296827	Y13Ag8Ga0	-0.26872
Y6Ag10Ga5	-0.363784	Y9Ag11Ga1	-0.331895	Y14Ag0Ga7	-0.42546
Y6Ag11Ga4	-0.371059	Y9Ag12Ga0	-0.301903	Y14Ag1Ga6	-0.435919
Y6Ag12Ga3	-0.349477	Y10Ag0Ga11	-0.614238	Y14Ag2Ga5	-0.388837
Y6Ag13Ga2	-0.34004	Y10Ag1Ga10	-0.559363	Y14Ag3Ga4	-0.352808
Y6Ag14Ga1	-0.312595	Y10Ag2Ga9	-0.504002	Y14Ag4Ga3	-0.306125
Y6Ag15Ga0	-0.248161	Y10Ag3Ga8	-0.488879	Y14Ag5Ga2	-0.293
Y7Ag0Ga14	-0.63107	Y10Ag4Ga7	-0.476924	Y14Ag6Ga1	-0.309236
Y7Ag1Ga13	-0.555172	Y10Ag5Ga6	-0.480076	Y14Ag7Ga0	-0.238415
Y7Ag2Ga12	-0.55395	Y10Ag6Ga5	-0.44736	Y15Ag0Ga6	-0.356645
Y7Ag3Ga11	-0.534761	Y10Ag7Ga4	-0.423717	Y15Ag1Ga5	-0.320627
Y7Ag4Ga10	-0.464927	Y10Ag8Ga3	-0.40038	Y15Ag2Ga4	-0.310604
Y7Ag5Ga9	-0.449368	Y10Ag9Ga2	-0.396912	Y15Ag3Ga3	-0.285855
Y7Ag6Ga8	-0.448992	Y10Ag11Ga0	-0.294614	Y15Ag4Ga2	-0.267839
Y7Ag8Ga6	-0.38663	Y11Ag0Ga10	-0.579954	Y15Ag5Ga1	-0.250898
Y7Ag9Ga5	-0.367633	Y11Ag1Ga9	-0.551459	Y15Ag6Ga0	-0.137152
Y7Ag10Ga4	-0.355922	Y11Ag2Ga8	-0.532543	Y16Ag0Ga5	-0.237073
Y7Ag11Ga3	-0.358358	Y11Ag3Ga7	-0.500935	Y16Ag1Ga4	-0.192542
Y7Ag12Ga2	-0.36462	Y11Ag4Ga6	-0.467401	Y16Ag2Ga3	-0.188206
Y7Ag13Ga1	-0.342385	Y11Ag5Ga5	-0.434346	Y16Ag3Ga2	-0.189003
Y7Ag14Ga0	-0.330834	Y11Ag6Ga4	-0.42574	Y16Ag4Ga1	-0.163729
Y8Ag0Ga13	-0.61486	Y11Ag7Ga3	-0.40524	Y16Ag5Ga0	0.0418757
Y8Ag1Ga12	-0.561593	Y11Ag8Ga2	-0.38675	Y17Ag0Ga4	-0.076967
Y8Ag2Ga11	-0.543902	Y11Ag9Ga1	-0.369906	Y17Ag1Ga3	-0.126683
Y8Ag3Ga10	-0.469833	Y11Ag10Ga0	-0.330911	Y17Ag2Ga2	-0.120487
Y8Ag4Ga9	-0.462899	Y12Ag0Ga9	-0.560053	Y17Ag3Ga1	-0.111765
Y8Ag5Ga8	-0.445202	Y12Ag1Ga8	-0.519488	Y17Ag4Ga0	0.0223123
Y8Ag6Ga7	-0.400067	Y12Ag2Ga7	-0.478285	Y18Ag0Ga3	-0.064324
Y8Ag7Ga6	-0.395419	Y12Ag3Ga6	-0.446126	Y18Ag1Ga2	-0.067532
Y8Ag9Ga4	-0.364051	Y12Ag4Ga5	-0.393984	Y18Ag2Ga1	-0.099245
Y8Ag10Ga3	-0.303631	Y12Ag5Ga4	-0.380117	Y18Ag3Ga0	0.0038864
Y8Ag11Ga2	-0.338324	Y12Ag6Ga3	-0.384486	Y19Ag0Ga2	0.0225156
Y8Ag12Ga1	-0.35148	Y12Ag7Ga2	-0.392774	Y19Ag1Ga1	-0.030434
Y8Ag13Ga0	-0.306589	Y12Ag8Ga1	-0.370591	Y19Ag2Ga0	0.026778
Y9Ag0Ga12	-0.60733	Y12Ag9Ga0	-0.318198	Y20Ag0Ga1	0.0202192
Y9Ag1Ga11	-0.549752	Y13Ag0Ga8	-0.515199	Y20Ag1Ga0	0.1870537
Y9Ag2Ga10	-0.487178	Y13Ag1Ga7	-0.457784	Y21Ag0Ga0	0
Y9Ag3Ga9	-0.481589	Y13Ag2Ga6	-0.453292	Y0Ag0Ga21	0
Y9Ag4Ga8	-0.451473	Y13Ag3Ga5	-0.369868	Y1Ag1Ga19	-0.144064
Y9Ag5Ga7	-0.398824	Y13Ag4Ga4	-0.337577	Y2Ag2Ga17	-0.265272
Y9Ag6Ga6	-0.399626	Y13Ag5Ga3	-0.349561	Y3Ag3Ga15	-0.399955

Table S5.8. continued from previous page

Y4Ag4Ga13	-0.495749	Y7Ag7Ga7	-0.412557	Y10Ag10Ga1	-0.389458
Y5Ag5Ga11	-0.518444	Y8Ag8Ga5	-0.364018		
Y6Ag6Ga9	-0.466551	Y9Ag9Ga3	-0.356293		

Table S5.9. Machine-learning predicted formation energy versus compositions for Y-Ag-In ternary phase system

composition	energy	composition	energy	composition	energy
Y0Ag1In20	0.0011429	Y1Ag19In1	0.026762	Y4Ag1In16	-0.29667
Y0Ag2In19	-0.002714	Y1Ag20In0	0.025905	Y4Ag2In15	-0.27752
Y0Ag3In18	-0.008571	Y2Ag0In19	-0.0759	Y4Ag3In14	-0.24138
Y0Ag4In17	-0.025429	Y2Ag1In18	-0.08576	Y4Ag5In12	-0.2351
Y0Ag5In16	-0.038286	Y2Ag3In16	-0.09848	Y4Ag6In11	-0.20595
Y0Ag6In15	-0.031143	Y2Ag4In15	-0.15333	Y4Ag7In10	-0.20281
Y0Ag7In14	-0.096	Y2Ag5In14	-0.15419	Y4Ag8In9	-0.14367
Y0Ag8In13	-0.083857	Y2Ag6In13	-0.06105	Y4Ag9In8	-0.25352
Y0Ag9In12	-0.067714	Y2Ag7In12	-0.0659	Y4Ag10In7	-0.31038
Y0Ag10In11	-0.087571	Y2Ag8In11	-0.09276	Y4Ag11In6	-0.21224
Y0Ag11In10	-0.078429	Y2Ag9In10	-0.10162	Y4Ag12In5	-0.2381
Y0Ag12In9	-0.092286	Y2Ag10In9	-0.10048	Y4Ag13In4	-0.19795
Y0Ag13In8	-0.137143	Y2Ag11In8	-0.07233	Y4Ag14In3	-0.18981
Y0Ag14In7	-0.169	Y2Ag12In7	-0.14919	Y4Ag15In2	-0.15367
Y0Ag15In6	-0.051857	Y2Ag13In6	-0.10505	Y4Ag16In1	-0.13752
Y0Ag16In5	-0.017714	Y2Ag14In5	-0.0929	Y4Ag17In0	-0.11238
Y0Ag17In4	-0.014571	Y2Ag15In4	-0.07976	Y5Ag0In16	-0.37076
Y0Ag18In3	0.0385714	Y2Ag16In3	-0.03562	Y5Ag1In15	-0.31662
Y0Ag19In2	0.0377143	Y2Ag17In2	-0.00548	Y5Ag2In14	-0.26448
Y0Ag20In1	0.0048571	Y2Ag18In1	-0.02233	Y5Ag3In13	-0.29633
Y0Ag21In0	0	Y2Ag19In0	-0.03319	Y5Ag4In12	-0.29919
Y1Ag0In20	-0.010952	Y3Ag0In18	-0.22186	Y5Ag6In10	-0.2619
Y1Ag2In18	-0.027667	Y3Ag1In17	-0.17871	Y5Ag7In9	-0.27076
Y1Ag3In17	-0.045524	Y3Ag2In16	-0.16057	Y5Ag8In8	-0.28562
Y1Ag4In16	-0.060381	Y3Ag4In14	-0.17029	Y5Ag9In7	-0.31948
Y1Ag5In15	-0.062238	Y3Ag5In13	-0.17814	Y5Ag10In6	-0.29533
Y1Ag6In14	-0.063095	Y3Ag6In12	-0.167	Y5Ag11In5	-0.31119
Y1Ag7In13	-0.080952	Y3Ag7In11	-0.13286	Y5Ag12In4	-0.25005
Y1Ag8In12	-0.08181	Y3Ag8In10	-0.09471	Y5Ag13In3	-0.2259
Y1Ag9In11	-0.082667	Y3Ag9In9	-0.13057	Y5Ag14In2	-0.21576
Y1Ag10In10	-0.083524	Y3Ag10In8	-0.12443	Y5Ag15In1	-0.19462
Y1Ag11In9	-0.075381	Y3Ag11In7	-0.28929	Y5Ag16In0	-0.17748
Y1Ag12In8	-0.069238	Y3Ag12In6	-0.15714	Y6Ag0In15	-0.42371
Y1Ag13In7	-0.155095	Y3Ag13In5	-0.11	Y6Ag1In14	-0.41557
Y1Ag14In6	-0.110952	Y3Ag14In4	-0.10986	Y6Ag2In13	-0.32943
Y1Ag15In5	-0.04581	Y3Ag15In3	-0.10771	Y6Ag3In12	-0.32229
Y1Ag16In4	-0.015667	Y3Ag16In2	-0.06057	Y6Ag4In11	-0.29414
Y1Ag17In3	0.0034762	Y3Ag17In1	-0.07543	Y6Ag5In10	-0.291
Y1Ag18In2	0.032619	Y3Ag18In0	-0.06429	Y6Ag7In8	-0.34871

Table S5.9. continued from previous page

Y6Ag8In7	-0.326571	Y9Ag5In7	-0.39986	Y13Ag1In7	-0.33524
Y6Ag9In6	-0.335429	Y9Ag6In6	-0.31671	Y13Ag2In6	-0.2631
Y6Ag10In5	-0.316286	Y9Ag7In5	-0.32257	Y13Ag3In5	-0.25095
Y6Ag11In4	-0.288143	Y9Ag8In4	-0.26043	Y13Ag4In4	-0.20681
Y6Ag12In3	-0.276	Y9Ag10In2	-0.28014	Y13Ag5In3	-0.22567
Y6Ag13In2	-0.270857	Y9Ag11In1	-0.281	Y13Ag6In2	-0.25952
Y6Ag14In1	-0.252714	Y9Ag12In0	-0.28186	Y13Ag7In1	-0.24538
Y6Ag15In0	-0.261571	Y10Ag0In11	-0.45652	Y13Ag8In0	-0.22324
Y7Ag0In14	-0.453667	Y10Ag1In10	-0.45038	Y14Ag0In7	-0.33433
Y7Ag1In13	-0.427524	Y10Ag2In9	-0.41624	Y14Ag1In6	-0.28319
Y7Ag2In12	-0.434381	Y10Ag3In8	-0.3951	Y14Ag2In5	-0.24805
Y7Ag3In11	-0.348238	Y10Ag4In7	-0.34795	Y14Ag3In4	-0.2219
Y7Ag4In10	-0.307095	Y10Ag5In6	-0.23381	Y14Ag4In3	-0.25176
Y7Ag5In9	-0.348952	Y10Ag6In5	-0.25867	Y14Ag5In2	-0.20362
Y7Ag6In8	-0.38381	Y10Ag7In4	-0.28152	Y14Ag6In1	-0.20048
Y7Ag8In6	-0.321524	Y10Ag8In3	-0.27238	Y14Ag7In0	-0.19133
Y7Ag9In5	-0.264381	Y10Ag9In2	-0.29324	Y15Ag0In6	-0.25929
Y7Ag10In4	-0.266238	Y10Ag11In0	-0.28495	Y15Ag1In5	-0.27314
Y7Ag11In3	-0.259095	Y11Ag0In10	-0.42048	Y15Ag2In4	-0.239
Y7Ag12In2	-0.275952	Y11Ag1In9	-0.42633	Y15Ag3In3	-0.20086
Y7Ag13In1	-0.27381	Y11Ag2In8	-0.42919	Y15Ag4In2	-0.16971
Y7Ag14In0	-0.278667	Y11Ag3In7	-0.30905	Y15Ag5In1	-0.18257
Y8Ag0In13	-0.439619	Y11Ag4In6	-0.2449	Y15Ag6In0	-0.13243
Y8Ag1In12	-0.434476	Y11Ag5In5	-0.20476	Y16Ag0In5	-0.22024
Y8Ag2In11	-0.427333	Y11Ag6In4	-0.27962	Y16Ag1In4	-0.2271
Y8Ag3In10	-0.37919	Y11Ag7In3	-0.28648	Y16Ag2In3	-0.15195
Y8Ag4In9	-0.371048	Y11Ag8In2	-0.30933	Y16Ag3In2	-0.12881
Y8Ag5In8	-0.442905	Y11Ag9In1	-0.29419	Y16Ag4In1	-0.13567
Y8Ag6In7	-0.388762	Y11Ag10In0	-0.28805	Y16Ag5In0	-0.13952
Y8Ag7In6	-0.332619	Y12Ag0In9	-0.42543	Y17Ag0In4	-0.17419
Y8Ag9In4	-0.252333	Y12Ag1In8	-0.35229	Y17Ag1In3	-0.14105
Y8Ag10In3	-0.26919	Y12Ag2In7	-0.33714	Y17Ag2In2	-0.1159
Y8Ag11In2	-0.282048	Y12Ag3In6	-0.292	Y17Ag3In1	-0.11976
Y8Ag12In1	-0.282905	Y12Ag4In5	-0.28986	Y17Ag4In0	-0.07662
Y8Ag13In0	-0.281762	Y12Ag5In4	-0.22371	Y18Ag0In3	-0.10814
Y9Ag0In12	-0.447571	Y12Ag6In3	-0.29157	Y18Ag1In2	-0.131
Y9Ag1In11	-0.483429	Y12Ag7In2	-0.28243	Y18Ag2In1	-0.05686
Y9Ag2In10	-0.470286	Y12Ag8In1	-0.27529	Y18Ag3In0	-0.07271
Y9Ag3In9	-0.420143	Y12Ag9In0	-0.25114	Y19Ag0In2	-0.0801
Y9Ag4In8	-0.429	Y13Ag0In8	-0.38038	Y19Ag1In1	-0.04095

Table S5.9. continued from previous page

Y19Ag2In0	-0.02581	Y1Ag1In19	-0.02281	Y6Ag6In9	-0.273857
Y20Ag0In1	-0.023048	Y2Ag2In17	-0.089619	Y7Ag7In7	-0.356667
Y20Ag1In0	-0.001905	Y3Ag3In15	-0.141429	Y8Ag8In5	-0.256476
Y21Ag0In0	0	Y4Ag4In13	-0.246238	Y9Ag9In3	-0.272286
Y0Ag0In21	0	Y5Ag5In11	-0.272048	Y10Ag10In1	-0.297095

Table S5.10. Bond angles for $YAg_{0.65}In_{1.35}$

Atom	Angle (°)	Atom	Angle (°)
In(1)#1-Y(1)-In(1)#2	130.308(8)	In(1)#3-Y(1)-In(1)#8	86.599(18)
In(1)#1-Y(1)-In(1)#3	49.692(8)	In(1)#4-Y(1)-In(1)#8	93.401(18)
In(1)#2-Y(1)-In(1)#3	180	In(1)#5-Y(1)-In(1)#8	86.599(18)
In(1)#1-Y(1)-In(1)#4	65.64(3)	In(1)#6-Y(1)-In(1)#8	130.307(8)
In(1)#2-Y(1)-In(1)#4	93.402(18)	In(1)#7-Y(1)-In(1)#8	49.693(8)
In(1)#3-Y(1)-In(1)#4	86.598(18)	In(1)-Y(1)-In(1)#8	49.693(8)
In(1)#1-Y(1)-In(1)#5	114.36(3)	In(1)#1-Y(1)-In(1)#9	86.599(18)
In(1)#2-Y(1)-In(1)#5	86.598(18)	In(1)#2-Y(1)-In(1)#9	49.693(8)
In(1)#3-Y(1)-In(1)#5	93.402(18)	In(1)#3-Y(1)-In(1)#9	130.307(8)
In(1)#4-Y(1)-In(1)#5	180	In(1)#4-Y(1)-In(1)#9	49.693(8)
In(1)#1-Y(1)-In(1)#6	93.402(18)	In(1)#5-Y(1)-In(1)#9	130.307(8)
In(1)#2-Y(1)-In(1)#6	65.64(3)	In(1)#6-Y(1)-In(1)#9	86.599(18)
In(1)#3-Y(1)-In(1)#6	114.36(3)	In(1)#7-Y(1)-In(1)#9	93.401(18)
In(1)#4-Y(1)-In(1)#6	130.308(8)	In(1)-Y(1)-In(1)#9	93.402(18)
In(1)#5-Y(1)-In(1)#6	49.692(8)	In(1)#8-Y(1)-In(1)#9	114.36(3)
In(1)#1-Y(1)-In(1)#7	86.598(18)	In(1)#1-Y(1)-In(1)#10	93.401(18)
In(1)#2-Y(1)-In(1)#7	114.36(3)	In(1)#2-Y(1)-In(1)#10	130.307(8)
In(1)#3-Y(1)-In(1)#7	65.64(3)	In(1)#3-Y(1)-In(1)#10	49.693(8)
In(1)#4-Y(1)-In(1)#7	49.692(8)	In(1)#4-Y(1)-In(1)#10	130.307(8)
In(1)#5-Y(1)-In(1)#7	130.308(8)	In(1)#5-Y(1)-In(1)#10	49.693(8)
In(1)#6-Y(1)-In(1)#7	180	In(1)#6-Y(1)-In(1)#10	93.401(18)
In(1)#1-Y(1)-In(1)	180	In(1)#7-Y(1)-In(1)#10	86.599(18)
In(1)#2-Y(1)-In(1)	49.692(8)	In(1)-Y(1)-In(1)#10	86.598(18)
In(1)#3-Y(1)-In(1)	130.308(8)	In(1)#8-Y(1)-In(1)#10	65.64(3)
In(1)#4-Y(1)-In(1)	114.36(3)	In(1)#9-Y(1)-In(1)#10	180
In(1)#5-Y(1)-In(1)	65.64(3)	In(1)#1-Y(1)-In(1)#11	49.693(8)
In(1)#6-Y(1)-In(1)	86.598(18)	In(1)#2-Y(1)-In(1)#11	86.599(18)
In(1)#7-Y(1)-In(1)	93.402(18)	In(1)#3-Y(1)-In(1)#11	93.401(18)
In(1)#1-Y(1)-In(1)#8	130.307(8)	In(1)#4-Y(1)-In(1)#11	86.599(18)
In(1)#2-Y(1)-In(1)#8	93.401(18)	In(1)#5-Y(1)-In(1)#11	93.401(18)

Table S5.10. continued from previous page

In(1)#5-Y(1)-In(1)#11	93.401(18)	Y(1)#5-Y(1)-Y(1)#12	180
In(1)#6-Y(1)-In(1)#11	49.693(8)	In(1)#2-In(1)-In(1)#13	120
In(1)#7-Y(1)-In(1)#11	130.307(8)	In(1)#2-In(1)-In(1)#8	120
In(1)-Y(1)-In(1)#11	130.307(8)	In(1)#13-In(1)-In(1)#8	120
In(1)#8-Y(1)-In(1)#11	180	In(1)#2-In(1)-Y(1)#14	147.179(13)
In(1)#9-Y(1)-In(1)#11	65.64(3)	In(1)#13-In(1)-Y(1)#14	65.153(4)
In(1)#10-Y(1)-In(1)#11	114.36(3)	In(1)#8-In(1)-Y(1)#14	65.153(4)
In(1)#1-Y(1)-Y(1)#5	57.179(13)	In(1)#2-In(1)-Y(1)#15	147.179(13)
In(1)#2-Y(1)-Y(1)#5	122.821(13)	In(1)#13-In(1)-Y(1)#15	65.153(4)
In(1)#3-Y(1)-Y(1)#5	57.179(13)	In(1)#8-In(1)-Y(1)#15	65.153(4)
In(1)#4-Y(1)-Y(1)#5	122.821(13)	Y(1)#14-In(1)-Y(1)#15	65.64(3)
In(1)#5-Y(1)-Y(1)#5	57.179(13)	In(1)#2-In(1)-Y(1)	65.154(4)
In(1)#6-Y(1)-Y(1)#5	57.179(13)	In(1)#13-In(1)-Y(1)	147.179(13)
In(1)#7-Y(1)-Y(1)#5	122.821(13)	In(1)#8-In(1)-Y(1)	65.154(4)
In(1)-Y(1)-Y(1)#5	122.821(13)	Y(1)#14-In(1)-Y(1)	93.402(18)
In(1)#8-Y(1)-Y(1)#5	122.821(13)	Y(1)#15-In(1)-Y(1)	130.307(8)
In(1)#9-Y(1)-Y(1)#5	122.821(13)	In(1)#2-In(1)-Y(1)#16	65.154(4)
In(1)#10-Y(1)-Y(1)#5	57.179(13)	In(1)#13-In(1)-Y(1)#16	65.154(4)
In(1)#11-Y(1)-Y(1)#5	57.179(13)	In(1)#8-In(1)-Y(1)#16	147.179(13)
In(1)#1-Y(1)-Y(1)#12	122.821(13)	Y(1)#14-In(1)-Y(1)#16	130.307(8)
In(1)#2-Y(1)-Y(1)#12	57.179(13)	Y(1)#15-In(1)-Y(1)#16	93.402(18)
In(1)#3-Y(1)-Y(1)#12	122.821(13)	Y(1)-In(1)-Y(1)#16	130.307(8)
In(1)#4-Y(1)-Y(1)#12	57.179(13)	In(1)#2-In(1)-Y(1)#12	65.154(4)
In(1)#5-Y(1)-Y(1)#12	122.821(13)	In(1)#13-In(1)-Y(1)#12	147.179(13)
In(1)#6-Y(1)-Y(1)#12	122.821(13)	In(1)#8-In(1)-Y(1)#12	65.154(4)
In(1)#7-Y(1)-Y(1)#12	57.179(13)	Y(1)#14-In(1)-Y(1)#12	130.307(8)
In(1)-Y(1)-Y(1)#12	57.179(13)	Y(1)#15-In(1)-Y(1)#12	93.402(18)
In(1)#8-Y(1)-Y(1)#12	57.179(13)	Y(1)-In(1)-Y(1)#12	65.64(3)
In(1)#9-Y(1)-Y(1)#12	57.179(13)	Y(1)#16-In(1)-Y(1)#12	93.402(18)
In(1)#10-Y(1)-Y(1)#12	122.821(13)	In(1)#2-In(1)-Y(1)#17	65.154(4)

Table S5.10. continued from previous page

In(1)#11-Y(1)-Y(1)#12	122.821(13)	In(1)#13-In(1)-Y(1)#17	65.154(4)
In(1)#8-In(1)-Y(1)#17	147.179(13)	Y(1)#15-In(1)-Y(1)#17	130.307(8)
Y(1)#14-In(1)-Y(1)#17	93.402(18)	Y(1)-In(1)-Y(1)#17	93.402(18)

Chapter 6

Exploratory synthesis in the ternary *RE*-Au-Ge (*RE* = La, Ce, Pr, Nd) system

6.1 Introduction

Polar intermetallic compounds, a subset of metal-rich solids, have received much interest in academic laboratories as well as industrial research and development settings owing to their complex crystal structures and fascinating physical properties. Strictly defined, polar intermetallics are compounds that have the ratio of valence electrons per atoms between $1.2 \leq (e/a) \leq 4$ whereas Hume-Rothery and Zintl phases contain $1 \leq (e/a) \leq 2$ and $(e/a) \geq 4$, respectively.[6,130,131,133] For example, the e/a ratios for the well-known polar intermetallics AAu$_2$ (A = Na, K) and AAu$_5$ (A = K, Rb) can be calculated as 1.5 and 1.2 using 1 as the number of valence electrons for alkali metals and gold; 2 and 5 are considered as the number of anionic atoms per unit cell in AAu$_2$ and AAu$_5$, respectively.[6,219] Varying the e/a ratio and chemical composition subsequently yields a diversity of crystal structures and distinct chemical bonding that range from networks to clusters and even a quasicrystal.[7,220] The structural complexity of polar intermetallics can be justified because these compounds contain structural and bonding features from both Hume-Rothery and Zintl type compounds.[7] Unfortunately, there are no straightforward approaches to unambiguously count electrons or assign strict oxidation states in polar intermetallic phases. More compounds are therefore needed to unravel the intricacies of polar intermetallics, understand the structural tendencies, and interpret the chemical bonding behavior.

Ternary rare-earth (*RE*) transition-metal (*M*) germanides, *RE*–*M*–Ge, are one compositions space that form a large number of polar intermetallics. Ternary rare-earth transition metal germanides can be quickly reacted by arc-melting of the.[221] The products crystallize easily, and numerous ternary compounds have been identified and characterized. Indeed, these compounds are of great interest owing to their fascinating structural chemistries as well as physical properties, including superconductivity (*e.g.*, $RE_2Pt_3Ge_5$, $RE_2Ir_3Ge_5$)[222], magnetocaloric effects (*e.g.*, $GdRu_2Ge_2$)[223], and complex magnetic ordering (e.g., *RE*$CrGe_3$).[224] The magnetic properties stem from the interaction between the localized *f* electrons of a rare-earth atom and the *d* electrons of transition metal.[225] However, there are no obvious mechanisms for controlling magnetism in these compounds, even though some systems like *RE*-Ni-Ge have a been exhaustively studied.[226–228]

The exploration of the rare-earth *RE*–Au–Ge ternary phase space is far more limited. There is only one reported compound, *RE*AuGe (*RE* = La-Lu, except for Pm and Eu), which crystallizes in space group $P6_3mc$ (No. 186) with the LiGaGe-type structure.[229–231] The $[AuGe]^{n-}$ anionic sublattice in this compound features a strong polar-covalent bond between Ge–Au, and Au–Au, generating a three-dimensional polyanionic backbone. This crystal structure type is common among the rare-earth gold ternaries. For example, *RE*AuSn also adopts LiGaGe-type structure with a slightly smaller unit cell.[146,147,150] Furthermore, $REAu_2Ge_2$ has been identified in some RE systems like Ce and Pr, and their magnetic properties were studied.[232,233] $CeAu_2Ge_2$ and $PrAu_2Ge_2$ adopt $ThCr_2Si_2$-type crystal structure with $I4/mmm$ space group; they also are reported to order antiferromagnetically with the Néel temperature 16 and 11.9K.[228] The remaining rare-earth systems have not been extensively studied.

In this work, compounds in the *RE*–Au–Ge (*RE* = La, Ce, Pr, Nd) ternary phase space are identified though a systemic examination of these phase spaces. Ten compositions were prepared in each phase space, producing six new compounds adopting two different types of crystal structures. The synthesis and crystal structures of these new intermetallic compounds, La_3Au_3Ge and RE_2AuGe_3 (*RE* = La, Ce, Pr, Nd), are reported. In addition, $LaAu_2Ge_2$, which is isostructural and isotypic with the known Ce and Nd analogs, is confirmed.[228,232] Interestingly, in the RE_2AuGe_3 system, the La analog forms a more complex crystal structure compared to the other rare-earth systems. Therefore, the crystal structural preference was examined using DFT calculations by comparing the total energies of the two crystal structure types. Further, the density of state (DOS) was calculated to indicate the metallic nature of these compounds, and a bonding analysis was carried out. The results of this work helped further the fundamental understanding of gold-containing polar intermetallic phases.

6.2 Experimental

6.2.1 Synthesis

The starting metals, gold (splatter, 99.999%, Materion Advanced Chemical), germanium (powder, 99.99%, Alfa Aesar), and the rare-earth elements La, Ce, Pr, and Nd (filings, 99.8%, HEFA Rare Earth) were weighed out in the desired stoichiometric ratios and ground together with an agate mortar and pestle to form a uniform sample with a total weight of 200 mg. The samples were pressed into 6 mm pellets using a maximum pressure of 2500 psi. The samples were reacted using arc-melting (Centorr Furnace) under inert argon gas with the current around 45 A. All samples were arc-melted at least three times, including intermittently flipping the button to ensure homogeneity. The weight loss for each sample

after arc-melting was less than 2%. The arc-melted samples were then sealed in fused silica tubes under vacuum (10^{-3} torr) and annealed at 850°C for nine days. The samples were slowly cooled to room temperature over 24 hours. The products all had a silver luster, were brittle, and air-stable for approximately one week suggesting slow oxidation. The products were therefore handled and stored in a glovebox with an argon atmosphere (O_2 < 0.1 ppm; H_2O < 0.1 ppm). The preparation of $LaAuGe_3$, $LaAuGe_2$, $La_4Au_5Ge_{11}$, $LaAu_2Ge$, $LaAu_3Ge$, La_2AuGe, and La_2Au_2Ge was also attempted following the same synthetic procedure; however, the products from these reactions were all multiphase based on powder X-ray diffraction. Thus, these compositions were not studied further.

6.2.2 Powder X-ray Diffraction

X-ray powder diffractograms were collected using a PANalytical X'Pert powder diffractometer and Cu Kα radiation (λ = 1.54183 Å) at room temperature. The samples were prepared by grinding the annealed ingots in the glovebox using an agate mortar and pestle. The fine powder was then spread on a zero-diffraction silicon plate and covered with Kapton® film to prevent oxidation. Le Bail refinements were carried out to check for phase purity and determine the lattice parameters using the EXPGUI interface for the General Structure Analysis System (GSAS).[103,104] A shifted-Chebyshev function was used to model the background. All crystal structures were visualized using VESTA.[112]

6.2.3 Single-Cystal X-ray Diffraction

Single crystals for $LaAu_2Ge_2$, La_2AuGe_3, and Nd_2AuGe_3 compositions were picked from crushed ingots using an optical microscope. The data collection performed using a Bruker APEX II platform diffractometer equipped with a 4K CCD APEX II detector and a Mo Kα radiation source (λ = 0.71073 Å). Reflections were collected by taking three sets of 726

frames with 0.3° scans in ω and an exposure time of 40-50 seconds per frame at room temperature. The data were scaled, and an absorption correction was applied using SADABS.[106] Structure solution and refinement were carried out using the SHELXTL program package (version 6.12),[155] and refined by full-matrix least-squares on F_O^2, including anisotropic displacement parameters. The single-crystal data were then solved and refined with two domains. The results of crystal structure refinements for La_3Au_3Ge, $LaAu_2Ge_2$, La_2AuGe_3, and Nd_2AuGe_3 are given in Table 6.1, 6.2 and the refined atomic coordinates and equivalent isotropic displacement parameters are presented in Table 6.3.

Table 6.1. Crystallographic data for La_3Au_3Ge and $LaAu_2Ge_2$ collected at room temperature

Refined formula	La_3Au_3Ge	$LaAu_2Ge_2$
Formula mass (g mol^{-1})	1080.22	678.02
space group; Z	$R\bar{3}$; 6	$I4/mmm$; 2
a (Å)	14.04(1)	4.429(1)
b (Å)	14.04(1)	4.429(1)
c (Å)	6.220(5)	10.497(6)
V (Å^3)	1062.5(13)	205.90(14)
ρ_{calc} (g cm^{-3})	10.130	10.936
absorption correction	Empirical	
radiation	Mo Kα	
μ (mm^{-1})	83.625	95.348
θ range (deg.)	2.90- 27.56	3.88-27.32
hkl ranges	$-18 \leq h \leq 17$, $-14 \leq k \leq 18$, $-8 \leq l \leq 7$	$-5 \leq h \leq 5$, $-5 \leq k \leq 5$, $-4 \leq l \leq 11$
No. reflections; R_{int}	1690; 0.055	449; 0.0203
No. unique reflections	539	90
No. parameters	26	8
$R(F)$ for $F_o^2 > 2\sigma(F_o^2)$ [a]	0.0381	0.0370
$R_w(F_o^2)$ [b]	0.1055	0.0969
Goodness of fit	1.05	1.238
$(\Delta\rho)_{max}$, $(\Delta\rho)_{min}$ (e Å^{-3})	3.86, – 2.55	4.26, –5.52

[a] $R(F) = \sum||F_o| - |F_c|| / \sum|F_o|$

[b] $R_w(F_o^2) = [\sum[w(F_o^2 - F_c^2)^2] / \sum wF_o^4]^{1/2}$; $w^{-1} = \left|\sigma^2(F_o{}^2) + (Ap)^2 + Bp\right|$ where $p = [\max(F_o^2, 0) + 2F_c^2]/3$

Table 6.2. Crystallographic data for La_2AuGe_3 and Nd_2AuGe_3 collected at room temperature

Refined formula	La_2AuGe_3	Nd_2AuGe_3
Formula mass (g mol^{-1})	1385.11	703.22
space group; Z	$I4_1/amd$; 4	$P6/mmm$; 1
a (Å)	4.435(5)	4.320(6)
b (Å)	4.435(5)	4.320(6)
c (Å)	14.935(2)	4.234(6)
V (Å^3)	281.98(7)	68.43(16)
ρ_{calc} (g cm^{-3})	8.157	17.07
absorption correction	Empirical	
radiation	Mo Kα	
μ (mm^{-1})	56.34	122.819
θ range (deg.)	3.74-27.46	4.81 - 28.66
hkl ranges	$-5 \leq h \leq 5$,	$-5 \leq h \leq 5$,
	$-4 \leq k \leq 5$,	$-3 \leq k \leq 5$,
	$-14 \leq k \leq 18$	$-4 \leq l \leq 5$
No. reflections; R_{int}	1261;0.0514	338; 0.0253
No. unique reflections	100	52
No. parameters	10	6
$R(F)$ for $F_o^2 > 2\sigma(F_o^2)$ [a]	0.0451	0.0251
$R_w(F_o^2)$ [b]	0.1054	0.0679
Goodness of fit	1.2	1.20
$(\Delta\rho)_{max}$, $(\Delta\rho)_{min}$ (e Å^{-3})	2.12, –3.05	1.70, – 1.79

[a] $R(F) = \sum||F_o| - |F_c|| / \sum|F_o|$

[b] $R_w(F_o^2) = [\sum[w(F_o^2 - F_c^2)^2]/\sum wF_o^4]^{1/2}$; $w^{-1} = \left|\sigma^2(F_o{}^2) + (Ap)^2 + Bp\right|$ where $p = [\max(F_o^2, 0) + 2F_c^2]/3$

Table 6.3. Refined atomic coordinates and equivalent isotropic displacement parameters for La_3Au_3Ge, $LaAu_2Ge_2$, La_2AuGe_3, and Nd_2AuGe_3

Compound	atom	*Wyck.* site	Occ.	*x*	*y*	*z*	U_{eq} (Å^2)[a]
(a) La_3Au_3Ge							
	La	18*f*	1	0.2095(1)	0.0440(1)	0.26465(2)	0.0178(5)
	Au1	18*f*	0.89(1)	0.4472(7)	0.0564(7)	0.1155(1)	0.0174(3)
	Ge1	18*f*	0.11(1)	0.4472(7)	0.0564(7)	0.1155(1)	0.0174(3)
	Au2	3*b*	0.43(2)	0	0	1/2	0.041(2)
	Ge2	3*b*	0.57(2)	0	0	1/2	0.041(2)
	Au3	3*a*	0.56(2)	0	0	0	0.037(1)
	Ge3	3*a*	0.44(2)	0	0	0	0.037(1)
(a) $LaAu_2Ge_2$							
	La	2*a*	1	0	0	0	0.0056(8)
	Au	4*d*	1	0	1/2	1/4	0.0142(6)
	Ge	4*e*	1	0	0	0.3828(2)	0.003(1)
(b) La_2AuGe_3							
	La	4*a*	1	0	0	0	0.036(4)
	Au	8*e*	0.30(1)	0	0	0.4123(2)	0.012(3)
	Ge	8*e*	0.70(1)	0	0	0.4123(2)	0.012(3)
(c) Nd_2AuGe_3							
	Nd	1*a*	1	0	1/4	0.5284(3)	0.0068(5)
	Au	2*d*	0.40(2)	0.333	0.666	1/2	0.0141(6)
	Ge	2*d*	0.60(2)	0.333	0.666	1/2	0.0141(6)

[a] U_{eq} is defined as one-third of the trace of the orthogonalized U_{ij} tensor.

Table 6.4. Selected bond length [Å] for $LaAu_2Ge_2$, La_2AuGe_3, and Nd_2AuGe_3

La_3Au_3Ge		$LaAu_2Ge_2$		La_2AuGe_3		Nd_2AuGe_3	
La−*M*1	3.026(2)	La−Ge	3.365(2)	La−*M*	3.263(4)	Nd−*M*[a]	3.271(3)
La−*M2*	3.059(2	La−Au	3.434(1)	La−*M*	3.318(5)	Nd−*M*	3.271(2)
La−*M3*	3.151(2)	La−Ge	4.018(5)	La−*M*	3.324(3)	Nd−Nd	4.320(3)
La−*M1*	3.218(3)	La−La	4.429(1)	La−*M*	3.444(5)	Nd−Nd	4.320(6)
La−La	3.672(2)	Au−Ge	2.617(2)	La−La	4.345(5)	*M*−*M*	2.494(2)
M−*M*	3.169(2)	Au−Au	3.1316(6)	*M*−*M*	2.448(5)	*M*−*M*	2.494(3)
*M*2 −*M3*	3.110(2)	Au−Au	4.429(1)	*M*−*M*	2.584(2)		
*M*1 −*M1*	3.020(2)	Ge−Ge	2.460(6)				

[a]*M*= Ge/Au

6.2.4 Electronic and Chemical Bonding Calculations

First-principles calculations on ordered models of La_2AuGe_3, including total energy calculations and chemical bonding analyses, were performed using the Vienna *ab initio* simulation package (VASP).[117,118] The calculations used a plane-wave basis set with projector augmented wave (PAW) potentials,[119] a cutoff energy of 500 eV, a 4×4×2 Γ-centered Monkhorst–Pack *k*-point grid, and a convergence criteria of 1×10^{-8} eV and 1×10^{-6} eV was set for electronic and structure relaxation, respectively. The chemical bonding of La_2AuGe_3 was calculated based on the crystal orbital Hamilton population (–COHP) using the Local-Orbital Basis Suite toward Electronic Structure (LOBSTER).[156,157]

6.3 Results and Discussion

6.3.1 Crystal Structure Solution

The ternary *RE*–Au–Ge (*RE* = La, Ce, Pr, Nd) system was investigated by arc-melting ten separate compositions in each phase space. Each arc-melted sample was sealed in a fused

silica tube and annealed at 850°C to ensure the products are at thermal equilibrium. Figure S6.1 and Table S6.1 shows the phase analysis of the resulting powder X-ray diffractograms. Five novel compounds with the general compositions of La_3Au_3Ge and RE_2AuGe_3 (*RE* = La, Ce, Pr, Nd) were found by the inability to index the products to any known compound in the Inorganic Crystal Structure Database (ICSD).[79] Moreover, the existence of $LaAu_2Ge_2$ was confirmed to crystallize analogous to the $CeAu_2Ge_2$ and $PrAu_2Ge_2$. All other compounds prepared could be completely indexed to known binary compounds indicating there are no promising ternary compounds in these samples. The crystal structures of the unknown products were solved by picking small single crystals small (≈15-20 μm) from the crushed bulk ingots using an optical microscope. The crystal structure refinement data are provided in Table 6.1, Table 6.2, and Table 6.3.

La_3Au_3Ge adopts a rhombohedral crystal structure with space group $R\bar{3}$ (No. 148, Z = 6), illustrated in Figure 6.1. This compound is isostructural with the Pu_3Pd_4-type structure, where mixed Au/Ge atoms are placed on the Pd position.[234] This structure type was also previously reported for RE_3Pt_4 (all *RE* atoms except Eu) series.[235] Intensity statistics for La_3Au_3Ge ($<|E^2 - 1|>$) gave a clear indication of a centrosymmetric space group, $R\bar{3}$. The single-crystal data was subsequently refined for the site occupancies by mixing Au and Ge on three crystallographic sites (Wyckoff 18*f*, 3*b*, and 3*a* sites). Modeling statistical mixing on these three crystallographic positions was necessary to accurately assign electron density at each position and produce reasonable atomic displacement parameters. Incorporating statistical mixing also yielded the nominally loaded composition.

This crystal structure contains four crystallographic positions, with La occupying Wyckoff site 18*f* and Au/Ge (*M*) on Wyckoff site 18*f*, 3*b*, and 3*a* sites (Table 6.3). The *M*1 atoms, with the general site symmetry of 1, form the puckered 12-pointed star tunnels,

where each of the atom is connected to two other *M*1 atoms. The *M*1-*M*1 contacts are separated by ≈3.16 Å. Figure 6.1 indicates this bonding network where the M2/M3 is placed in the center of the tunnel, and La atoms form puckered hexagon between the stars' point. *M*2 and *M*3 atoms contain $\bar{3}$. site symmetry and form an infinite *M*2-*M*3 linear chain with interactions in the range of 3.11-3.15 Å. The *M*-*M* polyanionic interactions in this structure are longer than gold's metallic bonding.; however, they are in the range of 2.8–3.5 Å, which are still acceptable for aurophilic contacts.[236,237] The coordination environments around La atom, with site symmetry of 1, are 9-coordinated Au/Ge atoms with seven *M*1 atoms, one *M*2, and one *M*3. Lastly, to confirm the phase purity, the calculated pattern from the single-crystal solved structure was compared with the powder X-ray diffraction pattern, Figure S6.2.

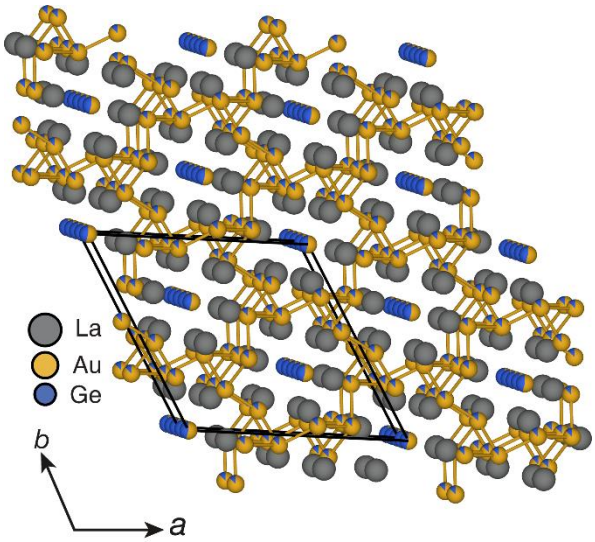

Figure 6.1. View of the La_3Au_3Ge crystal structure along the *c* axis. 12-pointed star tunnels of *M*1-*M*1 interactions centered with *M*2 and *M*3. Lanthanum, gold, and germanium are drawn as grey, yellow, and blue, respectively.

$LaAu_2Ge_2$, as shown in Figure 6.2a, crystallizes in the body-center tetragonal space group *I*4/*mmm* (No. 139, *Z* = 2) and adopts the $ThCr_2Si_2$-type crystal structure. The well-known $ThCr_2Si_2$-type is often described as an ordered ternary variant of the $BaAl_4$-type

structure.[238] This structure type contains three crystallographically independent positions, with La occupying Wyckoff site 2*a*, Au on Wyckoff 4*d* site, and Ge on Wyckoff 4*e* site. The structure is layered along the *c* axis with the edge-sharing [$AuGe_4$], separated by the planes of La atoms. The effective coordination polyhedron for the germanium and gold atoms corresponds to a distorted tetrahedron with site symmetry 4*mm* and $\bar{4}m2$, respectively. The coordination environments around the lanthanum atoms 8-coordinated by Ge with site symmetry 4/*mmm*. The germanium-germanium separation is 2.460(6) Å. The Au-Au distance is in the range of 3.1316(6) Å to 4.429(1) Å. Selected bond lengths for $LaAu_2Ge_2$ crystal structure are presented in Table 6.4. This crystal structure was confirmed by a Le Bail refinement of the powder X-ray diffraction patterns, Figure 6.2b, which also revealed the product is phase pure.

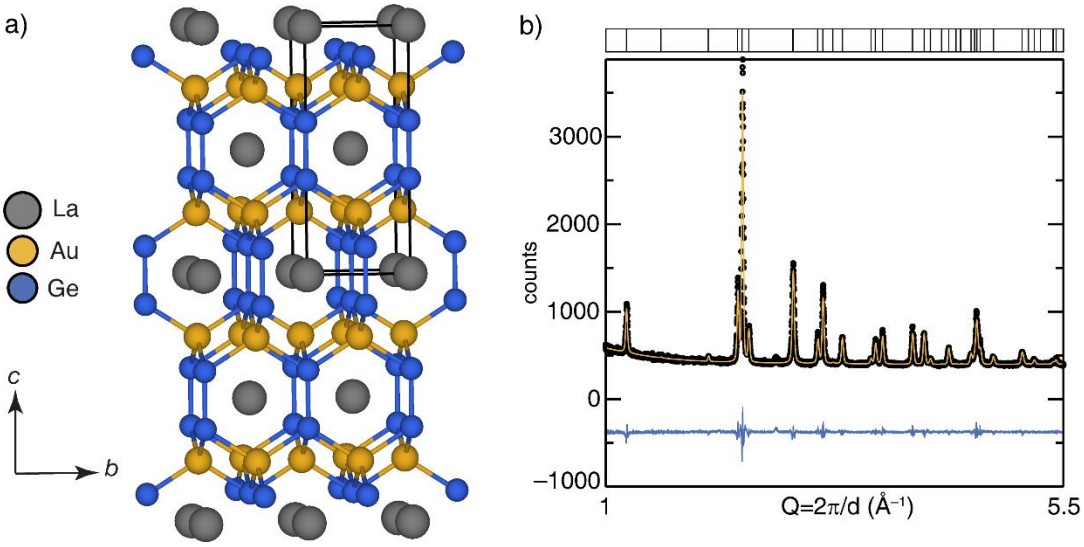

Figure 6.2. a) View of the $LaAu_2Ge_2$ crystal structure nearly along *a* axis. Lanthanum, gold, and germanium are drawn as grey, yellow, and blue, respectively. b) Le Bail refinement of powder X-ray diffractogram of $LaAu_2Ge_2$. The measured data are shown in black, the fit by the gold line, and the difference between the data and the fit by the blue line.

La_2AuGe_3 adopts the body-center tetragonal space group $I4_1/amd$ (No. 141, $Z = 4$) in the $ThSi_2$-type structure. There are two crystallographically positions in this structure, with La occupying Wyckoff site 4*a*, Ge/Au (M) on Wyckoff 8*e* site. Interestingly, this is the same structure as the binary $LaGe_2$ with slightly larger unit cell.[239] Since gold has a larger covalent radius than germanium (r_{Au} = 1.34 Å, r_{Ge}= 1.22 Å)[163] the unit cell parameters for La_2AuGe_3 from single-crystal X-ray diffraction are slightly larger than $LaGe_2$ increasing by only 0.27% in the *a/b* directions whereas the *c* lattice parameter increases by 4.7%. Thus, it is likely that a solid solution is forming, meaning it is better to rewrite the composition as $La(Au_{0.5}Ge_{1.5})$. The coordination number of *M* atom is nine, and the closest atoms are three *M* atoms with one apical contact ~ 2.408(6) (Å) and two horizontal contacts of ~ 2.504(2) (Å), as shown in Figure 6.3a. The Le Bail refinement of the powder X-ray diffraction patterns indicated the major phase is indeed $La(Au_{0.5}Ge_{1.5})$ with slight impurities of unidentified phase, signed with "+" in Figure 6.3b.

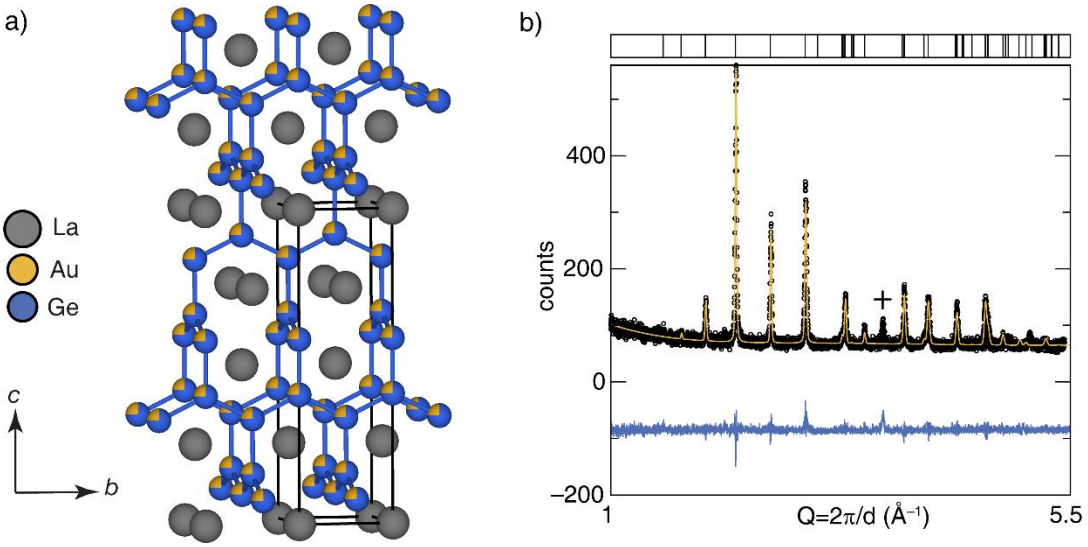

Figure 6.3. a) View of $La(Au_{0.5}Ge_{1.5})$ crystal structure nearly along *a* axis. Lanthanum, gold, and germanium are drawn as grey, yellow, and blue, respectively. b) Le Bail refinement of powder X-ray diffractogram of $La(Au_{0.5}Ge_{1.5})$. The measured data are shown in black, the fit by the gold line, and the difference between the data and the fit by the blue line.

Interestingly, changing the rare earth from La to Nd resulted in the discovery of an isotypic compound, Nd_2AuGe_3, that forms a different crystal structure. Illustrated in Figure 6.4a, Nd_2AuGe_3 forms a primitive hexagonal crystal structure (*P*6/*mmm*, No. 191, $Z = 1$) with the AlB_2-type structure. Based on systematic absences, the data set showed a primitive hexagonal lattice, and intensity statistics also ($<|E^2 - 1|>$) gave a clear indication of a centrosymmetric space group. The single-crystal data was refined to include site mixing between Ge and Au on a single crystallographic site (Wyckoff 2*d* site). Mixing on the 2*d* site was required to correctly describe electron density at this position. This well-known structure type contains two crystallographically independent positions, with Nd occupying Wyckoff site 1*a* and the (Ge/Au) statistically mixing on Wyckoff 2*d* site. The refined crystal structure contains an infinite honeycomb network formed by (Ge/Au)—(Ge/Au) interactions separated by 2.494(2) Å. These layers stack along the [001] direction, separated by 4.234(6) Å. The Nd atoms are located in the center of the hexagonal network with Nd—(Ge/Au) bonds of 3.271(1) Å. The phase purity and unit cell parameter are finally confirmed through a Le Bail refinement, shown in Figure 6.4b. The Le Bail refinement parameters are presented in Table S6.6.

The crystal structures of Ce_2AuGe_3 and Pr_2AuGe_3 were also determined, but using powder X-ray diffraction and starting from the Nd_2AuGe_3 structure refinement. Table S6.6 presents the Le Bail structural refinements for Ce_2AuGe_3 and Pr_2AuGe_3, and Figure S6.3, S6.4, is a plot of the refined diffractograms. Examining the crystal chemistry of these compounds by comparing their cell parameter and volume indicates the slight reduction in unit cell volume due to the decrease in rare-earth size.

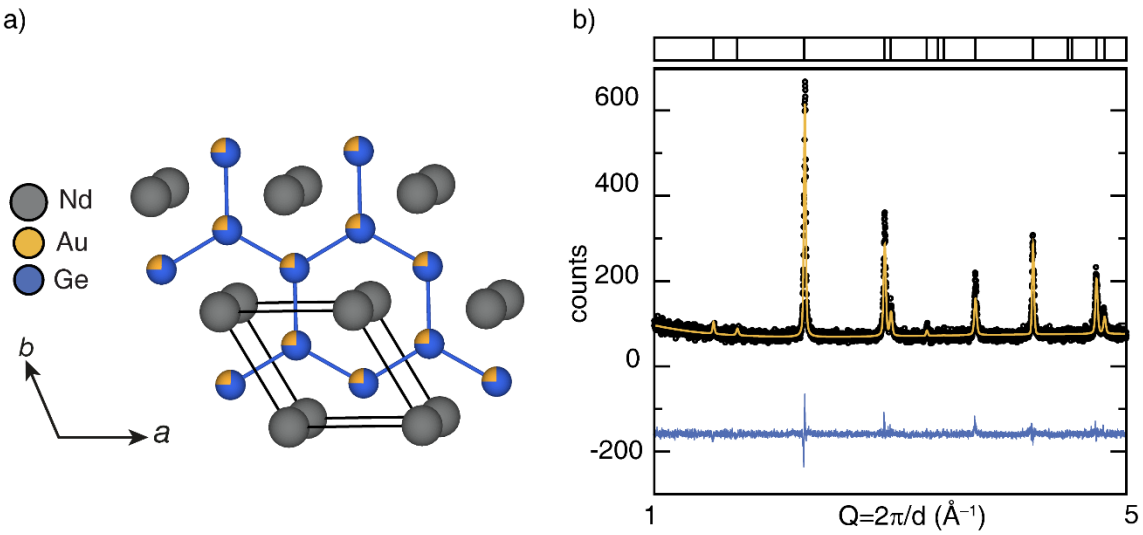

Figure 6.4 a) View of the Nd_2AuGe_3 crystal structure nearly along *c* axis. Lanthanum, gold, and germanium are drawn as grey, yellow, and blue, respectively. b) Le Bail refinement of powder X-ray diffractogram of Nd_2AuGe_3. The measured data are shown in black, the fit by the gold line, and the difference between the data and the fit by the blue line.

6.3.2 Crystal Structure Preference, Electronic structure, and Chemical Bonding in La_2AuGe_3

Lanthanides generally adopt the same crystal structure; however, there is some exception. For example, EuAuGe forms an orthorhombic *Imm*2 space group, whereas the other *RE*AuGe compounds adopt hexagonal $P6_3mc$. Interestingly, it appears a similar structure change occurs in the RE_2AuGe_3 (*RE* = La, Ce, Pr, Nd) series with the La composition forming a different structure type from the other rare-earths. Therefore, electronic structure calculations were employed to understand this structure preference. Since DFT fails at calculating the highly correlated 4*f* electrons present in Ce_2AuGe_3, Pr_2AuGe_3, and Nd_2AuGe_3, electronic structure calculations were only carried out on understanding the La_2AuGe_3 preference. Total energy calculations were therefore carried for this composition in space group $I4_1/amd$ and $P6/mmm$. Ordered models for both structures were required for these

calculations because the La_2AuGe_3 crystal structure contains a statistically mixed Au/Ge position. The program "Supercell"[165] was employed to enumerate all possible models, which resulted in 28 independent structures for the $I4_1/amd$ crystal structure after merging crystallographically equivalent models (Figure 6.5). The $P6/mmm$ structure produced five different ordered models after merging similar structures (Figure S6.5). These structural models were each optimized using DFT, and the relative total energies were calculated. According to this calculation, the total energy of the tetragonal $I4_1/amd$ structure (−5.2109 eV/atoms) is more favorable than the total energy of hexagonal $P6/mmm$ structure (−5.1996 eV/atom), in agreement with experimental results.

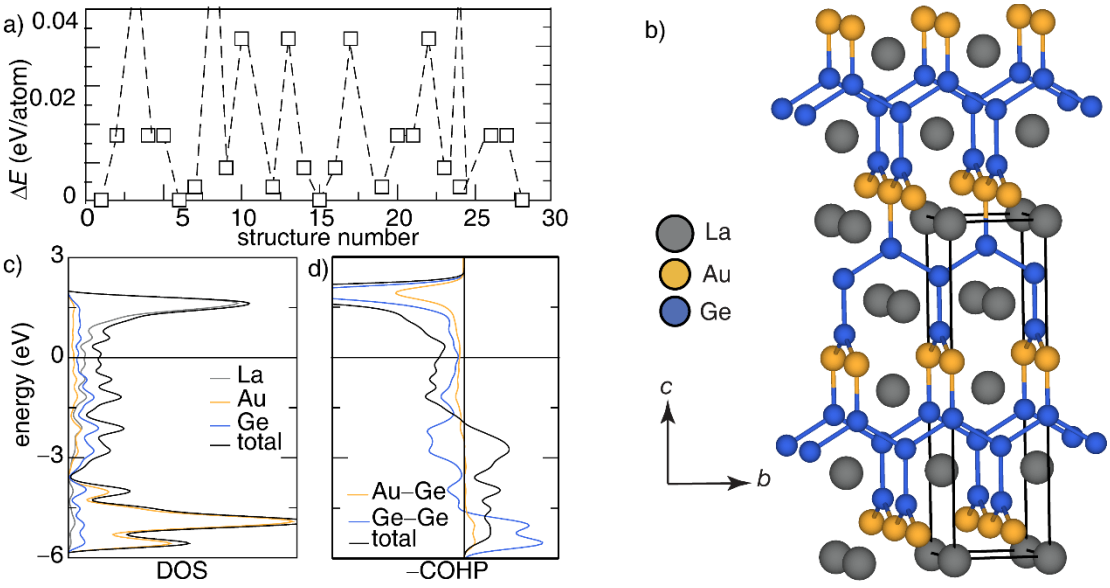

Figure 6.5. a) The Δ*E* of twenty-eight ordered crystal structures generated by Supercell for tetragonal $I4_1/amd$ space group for La_2AuGe_3. b) View of the lowest energy ordered crystal structure of La_2AuGe_3 with a tetragonal $I4_1/amd$ space group. Lanthanum, gold, and germanium are drawn as grey, yellow, and blue, respectively. c) The calculated density of states (DOS) for La_2AuGe_3. The total DOS is shown by the black line, while the partial DOS is shown for the Au in yellow, the La states in grey, and the Ge states blue. d) Crystal orbital Hamilton population (–COHP) curves plotting the total average of anionic sublattice interaction (black lines), the average Au–Ge interactions (yellow), and the average Ge–Ge interactions (blue). The positive direction on the abscissa is bonding interactions, whereas negative values are antibonding interactions. The Fermi level is set to 0 eV.

Examining the density of states (DOS) for La_2AuGe_3 with tetragonal $I4_1/amd$ space group, plotted in Figure 6.5c, indicates the Fermi level (E_F) falling into the pseudogap, implying the metallic nature of La_2AuGe_3. Decomposing the total DOS into its component orbitals illustrates the Au orbitals are mainly placed in the range of –6 to –3 eV, similar to other polar intermetallic compounds containing gold,[215,240] whereas the germanium orbitals are spread across the entire energy range calculated. The lanthanum orbitals fall primarily above the Fermi level as expected for the most electropositive element in the compound. The covalent-like chemical bonding was studied based on –COHP analyses using LOBSTER. These calculations were performed on the anionic network of La_2AuGe_3 structure, including gold and germanium interactions. As shown in Figure 6.5d, the majority of the occupied orbitals are bonding for the Au–Ge and Ge–Ge interactions (positive in the plot) and part of the occupied antibonding orbitals (negative in the plot) fall below E_F. Despite a number of occupied antibonding orbitals, these contacts have a net positive interaction based on the integrated crystal orbital Hamilton populations (–ICOHP). The average Au–Ge contacts is 0.395 eV/bond while average Ge–Ge interaction is 1.363 eV/bond, implying a majority of the total interactions are dominated by the Ge–Ge interaction. The Au–Au interactions in the La_2AuGe_3 crystal structure were insubstantial, suggesting no aurophilic contacts in this compound. Finally, La–Au and La–Ge interactions were also calculated (Figure S6.7) and show insignificant interaction, where the La–Ge contact (0.717 eV/bond) is more significant than La–Au (0.232 eV/bond) interaction.

6.4 Conclusion

The exploratory synthesis in the *RE*–Au–Ge phase space resulted in the discovery of six ternary compounds with the general composition with general compositions of La_3Au_3Ge,

$LaAu_2Ge_2$, and RE_2AuGe_3 (*RE* = La, Ce, Pr, Nd). All samples were arc-melted and annealed at 850 °C. The crystal structures were analyzed and solved using single-crystal X-ray diffraction analysis. La_3Au_3Ge crystallizes in a rhombohedral structure (space group $R\bar{3}$, No. 148, Z = 6) with a Pu_3Pd_4-type structure, whereas $LaAu_2Ge_2$ forms tetragonal space group $I4/mmm$ (No. 139, Z = 2) and adopts the $ThCr_2Si_2$-type crystal structure. In the RE_2AuGe_3 series, La_2AuGe_3 is isostructural with the parent structure of $LaGe_2$ ($ThSi_2$-type structure) with $I4_1/amd$ (No. 141, Z = 4) space group. Interestingly, the RE_2AuGe_3 series (*RE* = Ce, Pr, Nd) forms the well-known AlB_2-type structure ($P6/mmm$, No. 191, Z = 1). DFT calculations were performed on the La_2AuGe_3 compound to understand its structural preference, indicating the $I41/amd$ crystal structure is both thermodynamic and dynamic stability.

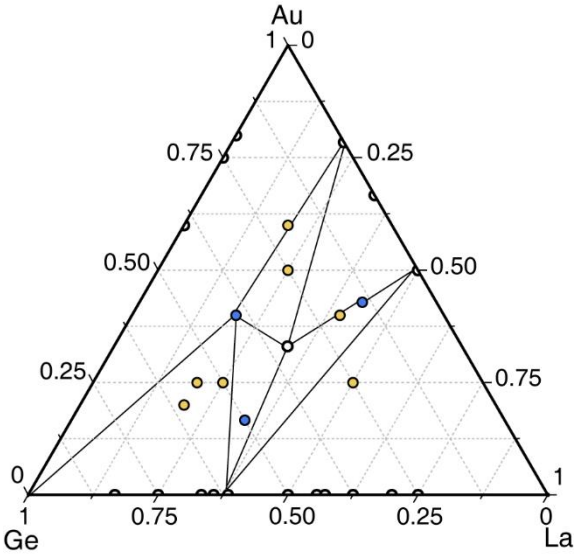

Figure S6.1. The La-Au-Ge ternary phase diagram at 850°C. The open circles indicate the reported ternary and binaries, while the colored circles illustrate the loaded compositions. Yellow circles are the compositions containing multiphases. Blue circles are the compositions identified by single-crystal X-ray diffraction analysis: La_2AuGe_3, $LaAu_2Ge_2$, and La_3Au_3Ge.

Table S6.1. Loaded La–Au–Ge compositions (at.%) and results of powder X-ray phase analysis after annealing at 850°C

No.	% La	% Au	% Ge	Targeted Composition	Products
1	33.3	16.7	50.0	La_2AuGe_3	La_2AuGe_3
2	20.0	40.0	40.0	$LaAu_2Ge_2$	$LaAu_2Ge_2$
3	42.9	42.9	14.2	La_3Au_3Ge	La_3Au_3Ge
4	20.0	20.0	60.0	$LaAuGe_3$	$LaAu_2Ge_2 + La_3Ge_5 + Ge$
5	25.0	25.0	50.0	$LaAuGe_2$	$LaAu_2Ge_2 + La_3Ge_5 + Ge$
6	20.0	25.0	55.0	$La_4Au_5Ge_{11}$	$LaAu_2Ge_2 + Ge$
7	25.0	50.0	25.0	$LaAu_2Ge$	$La_{14}Au_{51} + La_2Au_2Ge + LaAuGe$
8	20.0	60.0	20.0	$LaAu_3Ge$	$LaAu_2Ge_2 + La_{14}Au_{51}$
9	50.0	25.0	25.0	La_2AuGe	$La_3Ge_5 + LaAu + La$
10	40.0	40.0	20.0	La_2Au_2Ge	$LaAu + La_3Ge_5 + LaAuGe$

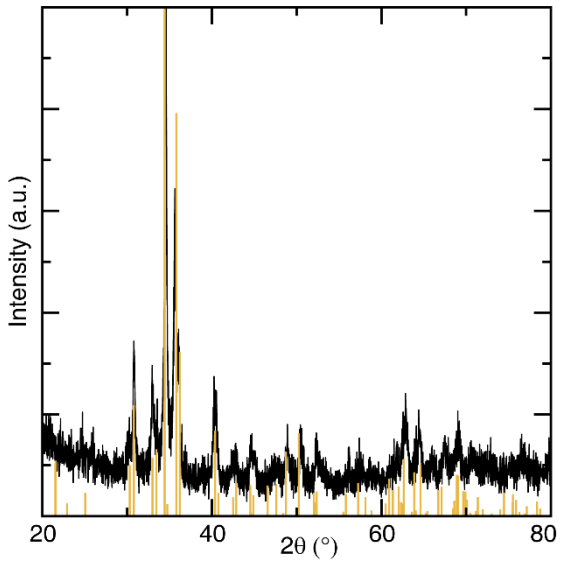

Figure S6.2. Powder X-ray diffraction pattern (black lines) of La_3Au_3Ge comparing with calculated pattern from single-crystal X-ray diffraction (yellow lines).

Table S6.2. Anisotropic displacement parameters (Å^2) for La_3Au_3Ge

Atom	U_{11}	U_{22}	U_{33}	U_{23}	U_{13}	U_{12}
La	0.0272(8)	0.0142(7)	0.0117(7)	0	0	0
Au1	0.0197(5)	0.0189(5)	0.0146(5)	0	0	0
Ge1	0.0197(5)	0.0189(5)	0.0146(5)	0	0	0
Au2	0.0136(15)	0.0136(15)	0.097(4)	0	0	0
Ge2	0.0136(15)	0.0136(15)	0.097(4)	0	0	0
Au3	0.0297(15)	0.0297(15)	0.052(3)	0	0	0
Ge3	0.0297(15)	0.0297(15)	0.052(3)	0	0	0

Table S6.3. Anisotropic displacement parameters (Å^2) for $LaAu_2Ge_2$

Atom	U_{11}	U_{22}	U_{33}	U_{23}	U_{13}	U_{12}
La	0.0052(1)	0.0052(1)	0.0063(2)	0	0	0
Ge	0.0056(1)	0.0056(1)	0.0027(2)	0	0	0
Au	0.0144(7)	0.0144(7)	0.0139(6)	0	0	0

Table S6.4. Anisotropic displacement parameters (Å^2) for La_2AuGe_3

Atom	U_{11}	U_{22}	U_{33}	U_{23}	U_{13}	U_{12}
Nd	0.026(6)	0.044(7)	0.039(8)	0	0	0
Ge	0.012(4)	0.014(4)	0.010(5)	0	0	0
Au	0.012(4)	0.014(4)	0.010(5)	0	0	0

Table S6.5. Anisotropic displacement parameters (Å^2) for Nd_2AuGe_3

Atom	U_{11}	U_{22}	U_{33}	U_{23}	U_{13}	U_{12}
Nd	0.0086(7)	0.0086(7)	0.0070(8)	0	0	0.0043(3)
Ge	0.0079(7)	0.0079(7)	0.0241(9)	0	0	0.0039(3)
Au	0.0079(7)	0.0079(7)	0.0241(9)	0	0	0.0039(3)

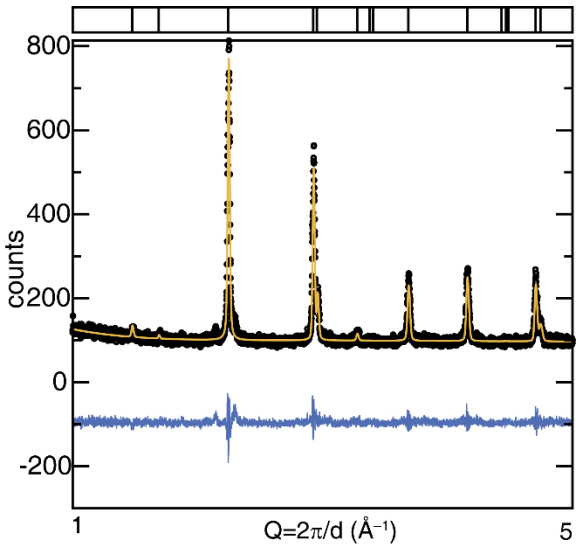

Figure S6.3. Le Bail refinement of X-ray powder diffraction data of Ce_2AuGe_3. The measured data are shown in black, the fit by the gold line, and the difference between the data and the fit by the blue line.

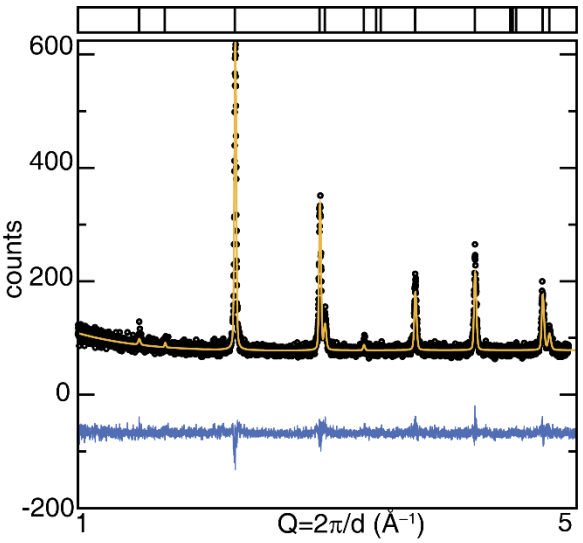

Figure S6.4. Le Bail refinement of X-ray powder diffraction data of Pr_2AuGe_3. The measured data are shown in black, the fit by the gold line, and the difference between the data and the fit by the blue line.

Table S6.7. Le Bail Refinement data for Ce_2AuGe_3, Pr_2AuGe_3, and Nd_2AuGe_3

Formula	Ce_2AuGe_3	Pr_2AuGe_3	Nd_2AuGe_3
Space group; Z		*P6/mmm;* 1	
a (Å)	4.2971(1)	4.2769(2)	4.2628(2)
c (Å)	4.2526(3)	4.2155(3)	4.1842(3)
Volume (Å^3)	578.979(1)	66.780(4)	65.846(4)
Calculated density (g cm^{-3})	8.485	8.659	8.867
Formula weight (g mol^{-1})	347.488	348.276	351.608
R_p	0.1203	0.1189	0.1109
R_{wp}	0.1696	0.1578	0.1637
χ^2	3.703	3.453	6.265

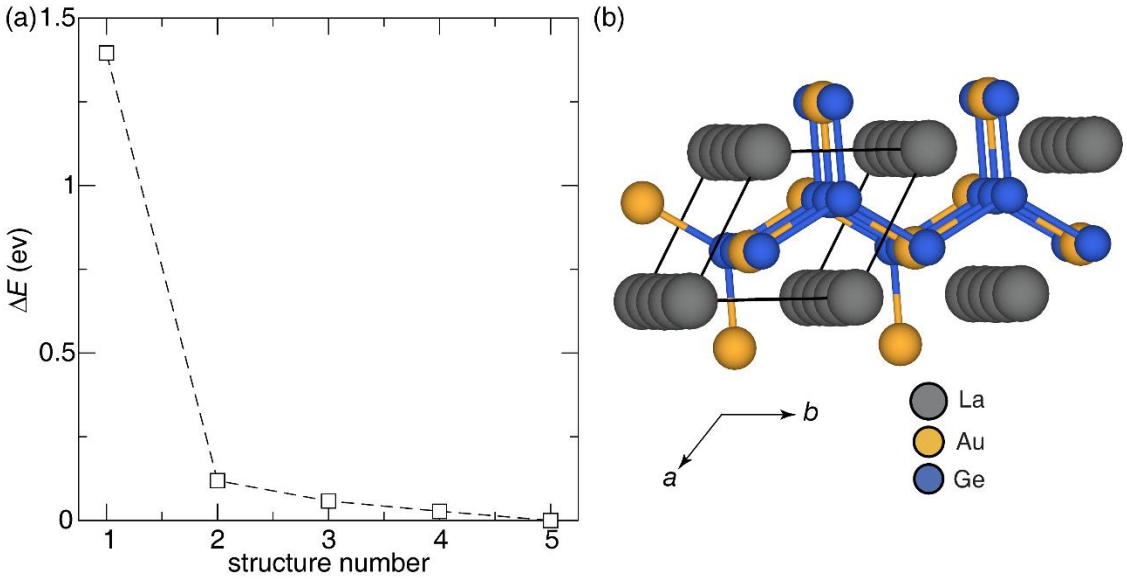

Figure S6.5. a) The ΔE of five ordered crystal structures of La_2AuGe_3 in *P*6/*mmm* space group generated by Supercell. b) View of the lowest energy ordered crystal structure of La_2AuGe_3 with hexagonal *P*6/*mmm* space group. Lanthanum, gold, and germanium are drawn as grey, yellow, and blue, respectively.

Table S6.8. Optimize- crystal structure La_2AuGe_3 in tetragonal space group

	Cal. La_2AuGe_3	Exp. La_2AuGe_3	Difference %
a (Å)	4.359	4.345	−0.42%
b (Å)	4.445	4.345	−2.30%
c (Å)	14.997	14.935	−0.43%
V (Å^3)	290.669	281.98	−3.08%

Table S6.9. Atomic coordinates for La_2AuGe_3 in tetragonal $I4_1/amd$ space group

atom	*x*	*y*	*z*
Ge	0	0	0.41757
Ge	1/2	1/2	0.91757
Ge	0	1/2	0.66530
Ge	1/2	0	0.16530
Ge	1/2	0	0.33139
Ge	0	1/2	0.83139
Au	1/2	1/2	0.08613
Au	0	0	0.58613
La	0	0	0.99540
La	0	0	0.49540
La	0	1/2	0.25421
La	1/2	0	0.75421

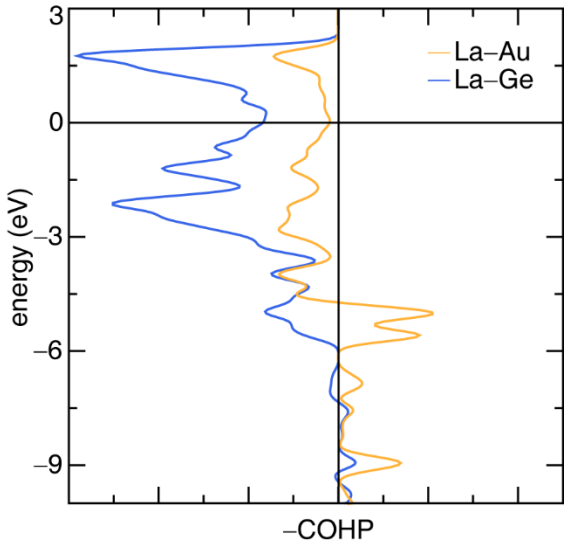

Figure S6.7. Crystal orbital Hamilton population (–COHP) curves plotting the La–Au and La–Ge interactions in the La_2AuGe_3 crystal structure.

Chapter 7

Conclusion and Future Outlook

The research presented in this dissertation focused on the complex crystal structure of novel intermetallic phases and established methodologies to accelerate the discovery of metal-rich compounds. Understanding the crystal chemistry of metal-rich solids is of great interest owing to the close connection between the crystal structure, composition, electronic structure, and observed physical properties. Thus, the electronic structure and chemical bonding of every discovered intermetallic were studied in this research. Moreover, machine learning algorithms were created to help generate new intermetallics that have never been reported. Most significantly, this work has conceived new methodologies to combine possible approaches in solid-state chemistry, including classical synthesis, characterization, computation, and data-driven analysis to address the scientific need.

First, a systematic search of the *RE*–Au–Sn (*RE* = La, Ce, Pr, Nd) ternary phase space revealed the existence of a series of compounds with the general formula $RE\mathrm{Au}_{1.5}\mathrm{Sn}_{0.5}$. These phases crystallize in the orthorhombic space group *Imma* with the CeCu_2-type structure. Most notable in these compounds is the polyanionic backbone composed of a single statistically mixed Au and Sn position, which creates a puckered hexagonal bonding network separated by the rare-earth atoms. *Ab initio* calculations were then carried out to identify the origin of the crystal structure. Electronic structure calculations to produce the density of states indicated the gold 5*d* bands dominate the Fermi level, while the crystal orbital Hamilton population (–COHP) curves demonstrated Au–Au and Au–Sn interactions which stabilized the crystal structure. Likewise, a qualitative electron localization function analysis supported the existence of a polyanionic network, and a Bader charge analysis

implied an anionic character of Au and Sn. Lastly, the preference for these compounds to adopt the simple $CeCu_2$-type structure was also determined using density functional theory calculations and compared to related compounds to establish a better picture of the unusual behavior of gold in polar intermetallic compounds.

The second investigation for the discovery of metal-rich materials used an *ab initio* approach coupled with a structure-search algorithm (CALYPSO) to predict the crystal structure of intermetallics under pressure. High-pressure synthesis and materials characterization is extremely arduous; therefore, employing a computational crystal structure predictive algorithm is a practical alternative to identify novel compounds. The research presented in this work indicated the existence of two compounds with the formula A_3Ir (A = Rb, Cs) that form at high pressure by constructing convex hulls for the Rb−Ir and Cs−Ir binary systems. These phases were identified using a nonbiased automatic structure search method based on DFT accompanied by a particle swarm optimization (PSO) algorithm. Increasing the applied pressure above ≈10 GPa showed a favorable formation enthalpy (ΔH) for Rb_3Ir with the Cu_3Ti structure type (space group *Pmnm*; No. 59), and Cs_3Ir in the Ni_3Ta structure type (space group $P2_1/m$; No. 11). Phonon calculations indicated that both compositions are dynamically stable in these structure types. Electronic structure calculations revealed that Rb_3Ir is a semiconductor with a ≈1.3 eV band gap, calculated using a hybrid exchange-correlation functional, whereas the Fermi level for Cs_3Ir falls into a deep pseudogap, suggesting poor metallic character. These high-pressure phases finally illustrated unusual oxidation states on the transition metal. Significantly, the charge on Ir is calculated to surpass −1 due to charge transfer between the alkali metal and iridium, implying the presence of an iridide anion at high pressure.

Despite the high-fidelity of DFT computation for predicting crystal structures, state-of-art machine-learning approaches are far more (computationally) efficient for predicting the existence of new phases. This dissertation presented an approach to aid the discovery of novel inorganic solids by combining experimental solid-state synthesis, DFT calculations, and machine learning. A support vector regression (SVR) algorithm was constructed to predict a compound's formation energy ($\Delta E_{f,\,\mathrm{SVR}}$) based solely on chemical composition using data from 313,965 high-throughput DFT calculations. These predicted formation energies (r^2 = 0.94; MAE = 85 meV/atom) were then utilized to construct zero-Kelvin convex hull diagrams and identify compositions immediately on the hull, as well as +50 meV above the convex hull, to capture potential compounds that are considered energetically unfavorable but that are still experimentally accessible. Using this methodology, four ternary composition diagrams, Y–Ag–*Tr* (*Tr* = B, Al, Ga, In), were explored. A particularly promising but unexplored region in the Y–Ag–In diagram was identified, and the ensuing solid-state high-temperature synthesis produced $YAg_{0.65}In_{1.35}$, which has not been reported. DFT calculations were finally used to determine the ordering of Ag and In as well as confirm the crystal structure solution since X-ray diffraction techniques failed to distinguish the mixing of Ag/In.

Finally, a systematic search of the *RE*-Au-Ge (*RE* = La, Ce, Pr, Nd) ternary phase space was performed by loading more than ten compositions. All compositions were reacted by arc-melting the elements followed by annealing at 800°C. Analyzing the products by X-ray diffraction indicated the existence of six novel compounds with general compositions of La_3Au_3Ge, $LaAu_2Ge_2$, and RE_2AuGe_3 (*RE* = La, Ce, Pr, Nd). La_3Au_3Ge adopts a rhombohedral structure (space group $R\bar{3}$, No. 148, Z = 6) with a Pu_3Pd_4-type structure, whereas $LaAu_2Ge_2$ crystallizes in tetragonal space group $I4/mmm$ (No. 139, Z = 2) and

adopts the $ThCr_2Si_2$-type crystal structure. In the RE_2AuGe_3 series, La_2AuGe_3 is isostructural with the parent structure of $LaGe_2$ ($ThSi_2$-type structure) with the $I4_1/amd$ (No. 141, Z = 4) space group. The RE_2AuGe_3 series (RE = Ce, Pr, Nd), interestingly, forms the well-known AlB_2-type structure ($P6/mmm$, No. 191, Z = 1). First-principles calculations were performed on the La_2AuGe_3 compound to understand this peculiar behavior of the RE_2AuGe_3 series. The results show that the $I4_1/amd$ crystal structure exhibits both thermodynamic and dynamic stability.

In conclusion, the research presented in this dissertation has led to the discovery of novel intermetallic phases and the understanding of their crystal structures through different methodologies. Undoubtedly, there are many research opportunities to continue this work. Indeed, this research has highlighted the significance of combining different approaches, such as solid-state synthesis, first-principles calculations, and machine-learning algorithms. Despite the long history of intermetallics, there are numerous unstudied phases in which chemists were not able to overcome experimental barriers. However, DFT computation and data-driven approaches hold the promise to aid scientists in identifying novel phases by predicting crystal structures and the formation energy of compounds. Employing the knowledge generated through this work will undoubtedly guide scientists to accelerate the discovery of novel metal-rich materials, leading in the identification of their exotic physical properties to fulfill scientific and industrial goals.

Bibliography

(1) Kauzlarich, S. M. Special Issue: Advances in Zintl Phases. *Materials*. **2019**, 2554.

(2) Gvozdetskyi, V.; Owens-Baird, B.; Hong, S.; Zaikina, J. Thermal Stability and Thermoelectric Properties of NaZnSb. *Materials (Basel).* **2018**, *12* (1), 48.

(3) Holger Kahlert, H. K.; Hans-Uwe Schuster, H. S. Elektrovalente terNäre Phasen Des Natriums Bzw. Kaliums Mit 2 B- Und 5 B-Elementen. *Z. Naturforsch. B*. **1976**, 1538–1539.

(4) Gille, P.; Grin, Y. *Crystal Growth of Intermetallics*; De Gruyter, **2018**.

(5) Kauzlarich, S. M.; Zevalkink, A.; Toberer, E.; Snyder, G. J. Zintl Phases: Recent Developments in Thermoelectrics and Future Outlook. *RSC Energy Environ. Ser.* **2017**, *17*, 1–26.

(6) Miller, G. J.; Thimmaiah, S.; Smetana, V.; Palasyuk, A.; Lin, Q. Gold's Structural Versatility within Complex Intermetallics: From Hume-Rothery to Zintl and Even Quasicrystals. In *Materials Research Society Symposium Proceedings*; Cambridge University Press, **2013**, *1517*, 55–66.

(7) Smetana, V.; Rhodehouse, M.; Meyer, G.; Mudring, A. V. Gold Polar Intermetallics: Structural Versatility through Exclusive Bonding Motifs. *Acc. Chem. Res.* **2017**, *50*

(11), 2633–2641.

(8) Brrmy, B. R. L.; Raynoi, G. V. The Crystal Chemistry of the Laves Phases. *Acta Cryst* **1953**, *6*, 178.

(9) Murty, B. S.; Yeh, J. W.; Ranganathan, S. Intermetallics, Interstitial Compounds and Metallic Glasses in High-Entropy Alloys. In *High Entropy Alloys*; Elsevier, **2014**, 119–131.

(10) Johnston, R. L.; Hoffmann, R. Structure-Bonding Relationships in the Laves Phases. *Zeitschrift für Anorg. und Allg. Chemie* **1992**, *616* (10), 105–120.

(11) Seibel, E. M.; Schoop, L. M.; Xie, W.; Gibson, Q. D.; Webb, J. B.; Fuccillo, M. K.; Krizan, J. W.; Cava, R. J. Gold–Gold Bonding: The Key to Stabilizing the 19-Electron Ternary Phases LnAuSb (Ln = La–Nd and Sm). *J. Am. Chem. Soc.* **2015**, *137* (3), 1282–1289.

(12) Li, B.; Kim, S. J.; Miller, G. J.; Corbett, J. D. Gold Tetrahedra as Building Blocks in K_3Au_5Tr (Tr=In, Tl) and Rb_2Au_3Tl and in Other Compounds: A Broad Group of Electron-Poor Intermetallic Phases. *Inorg. Chem.* **2009**, *48* (14), 6573–6583.

(13) Black, P. . Structural Relationships between Intermetallic Compounds. *Acta Metall.* **1956**, *4* (2), 172–179.

(14) Stoloff, N. S.; Liu, C. T.; Deevi, S. C. Emerging Applications of Intermetallics. *Intermetallics* **2000**, *8* (9–11), 1313–1320.

(15) Holt, S. L. *Inorganic Syntheses*; Wiley Blackwell, **2006**, 22.

(16) Corbett, J. D. Exploratory Synthesis: The Fascinating and Diverse Chemistry of Polar Intermetallic Phases. *Inorg. Chem.* **2010**, *49* (1), 13–28.

(17) Corbett, J. D.; Simon, A. Tantalum as a High-Temperature Container Material for Reduced Halides. In *Inorganic Syntheses*; **2006**, 22, 15–22.

(18) Merkle, R.; Maier, J. On the Tammann-Rule. *Zeitschrift für Anorg. und Allg. Chemier Anorg. und Allg. Chemie* **2005**, *631* (6–7), 1163–1166.

(19) Shcherbakov, A. I. Theory of Dissolution of Binary Alloys and the Tamman Rule. *Prot. Met.* **2005**, *41* (1), 30–35.

(20) Sologub, O. L.; Hiebl, K.; Salamakha, P. S.; Ipser, H. Crystal Structure and Physical Properties of Ternary Compounds RPt_3B, R = La, Pr, Nd. *J. Alloys Compd.* **2003**.

(21) Salamakha, P. S.; Sologub, O. L.; Rizzoli, C.; Hester, J. R.; Stepien-Damm, J.; Gonçalves, A. P.; Lopes, E. B.; Almeida, M. Ternary RPt_4B (R=La, Ce, Pr, Nd) Compounds; Structural and Physical Characterisation. *Intermetallics* **2004**, *12* (12), 1325–1334.

(22) Ku, H. C.; Meisner, G. P.; Acker, F.; Johnston, D. C. Superconducting and Magnetic Properties of New Ternary Borides with the $CeCo_3B_2$-Type Structure. *Solid State Commun.* **1980**, *35* (2), 91–96.

(23) Jung, W. Ternäre Seltenerd-Iridiumboride $SEIr_2B_2$ (SE ≡ Y, La, Ce, Pr, Nd, Sm, Eu, Gd, Tb, Dy) Mit $CaRh_2B_2$-Struktur. *J. Less-Common Met.* **1991**, *171* (1), 119–125.

(24) Rogl, P. The Crystal Structure of $LaIr_4B_4$, $ThOs_4B_4$, $ThIr_4B_4$ ($NdCo_4B_4$-Type) and URu_4B_4, UOs_4B_4 (LuRu4B<sub>4-Type). *Monatshefte für Chemie* **1980**, *111* (2), 517–527.

(25) Xu, R.; Pang, W.; Huo, Q. *Modern Inorganic Synthetic Chemistry*; Elsevier, 2011.

(26) Munir, Z. A.; Anselmi-Tamburini, U.; Ohyanagi, M. The Effect of Electric Field and

Pressure on the Synthesis and Consolidation of Materials: A Review of the Spark Plasma Sintering Method. *Journal of Materials Science*. **2006**, 763–777.

(27) Spark Plasma Sintering - an overview | ScienceDirect Topics.

(28) Kanatzidis, M. G.; Pöttgen, R.; Jeitschko, W. The Metal Flux: A Preparative Tool for the Exploration of Intermetallic Compounds. *Angewandte Chemie - International Edition*. **2005**, 6996–7023.

(29) Campbell, F. *Phase Diagrams: Understanding the Basics*; ASM International, **2012**.

(30) Zhao, J. C. *Methods for Phase Diagram Determination*; **2007**.

(31) Owens-Baird, B.; Wang, J.; Wang, S. G.; Chen, Y.-S.; Lee, S.; Donadio, D.; Kovnir, K. III–V Clathrate Semiconductors with Outstanding Hole Mobility: $Cs_8In_{27}Sb_{19}$ and $A_8Ga_{27}Sb_{19}$ (A = Cs, Rb). *J. Am. Chem. Soc.* **2020**, *142* (4), 2031–2041.

(32) Smetana, V.; Corbett, J. D.; Miller, G. J. Four Polyanionic Compounds in the K–Au–Ga System: A Case Study in Exploratory Synthesis and of the Art of Structural Analysis. *Inorg. Chem.* **2012**, *51* (3), 1695–1702.

(33) Smetana, V.; Corbett, J. D.; Miller, G. J. Four Polyanionic Compounds in the K–Au–Ga System: A Case Study in Exploratory Synthesis and of the Art of Structural Analysis. *Inorg. Chem.* **2012**, *51* (3), 1695–1702.

(34) Müller, J.; Zachwieja, U. K_4Au_8Ga: Eine Auffüllungsvariante Des $MgCu_2$-Typs. *Zeitschrift für Anorg. und Allg. Chemie* **2000**, *626* (9), 1867–1870.

(35) Phelan, W. A.; Menard, M. C.; Kangas, M. J.; McCandless, G. T.; Drake, B. L.; Chan, J. Y. Adventures in Crystal Growth: Synthesis and Characterization of Single Crystals of

Complex Intermetallic Compounds. *Chemistry of Materials*. **2012**, 409–420.

(36) Canfield, P. C.; Fisk, Z. Growth of Single Crystals from Metallic Fluxes. *Philos. Mag. B Phys. Condens. Matter; Stat. Mech. Electron. Opt. Magn. Prop.* **1992**, *65* (6), 1117–1123.

(37) MacAluso, R. T.; Millican, J. N.; Nakatsuji, S.; Lee, H. O.; Carter, B.; Moreno, N. O.; Fisk, Z.; Chan, J. Y. A Comparison of the Structure and Localized Magnetism in Ce_2PdGa_{12} with the Heavy Fermion $CePdGa_6$. *J. Solid State Chem.* **2005**, *178* (11), 3547–3553.

(38) Macaluso, R. T.; Nakatsuji, S.; Lee, H.; Fisk, Z.; Moldovan, M.; Young, D. P.; Chan, J. Y. Synthesis, Structure, and Magnetism of a New Heavy-Fermion Antiferromagnet, $CePdGa_6$. *J. Solid State Chem.* **2003**, *174* (2), 296–301.

(39) Millican, J. N.; Macaluso, R. T.; Young, D. P.; Moldovan, M.; Chan, J. Y. Synthesis, Structure, and Physical Properties of Ce_2PdGa_{10}. *J. Solid State Chem.* **2004**, *177* (12), 4695–4700.

(40) Park, S. M.; Eun, S. C.; Kang, W.; Kim, S. J. $Eu_5In_2Sb_6$, $Eu_5In_{2-x}Zn_xSb_6$: Rare Earth Zintl Phases with Narrow Band Gaps. *J. Mater. Chem.* **2002**, *12* (6), 1839–1843.

(41) Ferreira, S. *Advanced Topics on Crystal Growth*; **2013**.

(42) Tomaszewski, P. E. Jan Czochralski - Father of the Czochralski Method. *J. Cryst. Growth* **2002**, *236* (1–3), 1–4.

(43) Müller, G. Review: The Czochralski Method - Where We Are 90 Years after Jan Czochralski's Invention. In *Crystal Research and Technology*; John Wiley & Sons, Ltd, **2007**, 42, 1150–1161.

(44) Brown, R. A. Theory of Transport Processes in Single Crystal Growth from the Melt.

AIChE J. **1988**, *34* (6), 881–911.

(45) Oliynyk, A. O.; Mar, A. Discovery of Intermetallic Compounds from Traditional to Machine-Learning Approaches. *Acc. Chem. Res.* **2018**, *51* (1), 59–68.

(46) Wang, Y.; Lv, J.; Zhu, L.; Ma, Y. Crystal Structure Prediction via Particle-Swarm Optimization. *Phys. Rev. B - Condens. Matter Mater. Phys.* **2010**, *82* (9).

(47) Wu, S. Q.; Ji, M.; Wang, C. Z.; Nguyen, M. C.; Zhao, X.; Umemoto, K.; Wentzcovitch, R. M.; Ho, K. M. An Adaptive Genetic Algorithm for Crystal Structure Prediction. *J. Phys. Condens. Matter* **2014**, *26* (3), 35402.

(48) Pickard, C. J.; Needs, R. J. Ab Initio Random Structure Searching. *J. Phys. Condens. Matter*. **2011**.

(49) Glass, C. W.; Oganov, A. R.; Hansen, N. USPEX-Evolutionary Crystal Structure Prediction. *Comput. Phys. Commun.* **2006**, *175*, 713–720.

(50) Trimarchi, G.; Zunger, A. Global Space-Group Optimization Problem: Finding the Stablest Crystal Structure without Constraints. *Phys. Rev. B - Condens. Matter Mater. Phys.* **2007**, *75* (10).

(51) Lonie, D. C.; Zurek, E. XtalOpt: An Open-Source Evolutionary Algorithm for Crystal Structure Prediction. *Comput. Phys. Commun.* **2011**, *182* (2), 372–387.

(52) Bahmann, S.; Kortus, J. EVO - Evolutionary Algorithm for Crystal Structure Prediction. *Comput. Phys. Commun.* **2013**, *184* (6), 1618–1625.

(53) Wang, Y.; Lv, J.; Zhu, L.; Ma, Y. CALYPSO: A Method for Crystal Structure Prediction. *Comput. Phys. Commun.* **2012**, *183* (10), 2063–2070.

(54) Zurek, E.; Bi, T. High-Temperature Superconductivity in Alkaline and Rare Earth Polyhydrides at High Pressure: A Theoretical Perspective. *J CHEM PHYS*. 2019.

(55) Peng, F.; Wang, Y.; Wang, H.; Zhang, Y.; Ma, Y. Stable Xenon Nitride at High Pressures. *Phys. Rev. B - Condens. Matter Mater. Phys.* **2015**, *92* (9), 81.

(56) Zhong, X.; Yang, L.; Qu, X.; Wang, Y.; Yang, J.; Ma, Y. Crystal Structures and Electronic Properties of Oxygen-Rich Titanium Oxides at High Pressure. **2018**.

(57) Liu, H.; Naumov, I. I.; Hoffmann, R.; Ashcroft, N. W.; Hemley, R. J. Potential High-Tc Superconducting Lanthanum and Yttrium Hydrides at High Pressure. *Proc. Natl. Acad. Sci. U. S. A.* **2017**, *114* (27), 6990–6995.

(58) Miao, M. S.; Wang, X. L.; Brgoch, J.; Spera, F.; Jackson, M. G.; Kresse, G.; Lin, H. Q. Anionic Chemistry of Noble Gases: Formation of Mg-NG (NG = Xe, Kr, Ar) Compounds under Pressure. *J. Am. Chem. Soc.* **2015**, *137* (44), 14122–14128.

(59) Zhu, L.; Liu, H.; Pickard, C. J.; Zou, G.; Ma, Y. Reactions of Xenon with Iron and Nickel Are Predicted in the Earth's Inner Core. *Nat. Chem.* **2014**, *6* (7), 644–648.

(60) Miao, M.; Brgoch, J.; Krishnapriyan, A.; Goldman, A.; Kurzman, J. A.; Seshadri, R. On the Stereochemical Inertness of the Auride Lone Pair: Ab Initio Studies of AAu (A = K, Rb, Cs). *Inorg. Chem.* **2013**, *52* (14), 8183–8189.

(61) Brgoch, J.; Hermus, M. Pressure-Stabilized Ir^{-3} in a Superconducting Potassium Iridide. *J. Phys. Chem. C* **2016**, *120* (36), 20033–20039.

(62) Lotfi, S.; Brgoch, J. Predicting Pressure-Stabilized Alkali Metal Iridides: A–Ir (A = Rb, Cs). *Comput. Mater. Sci.* **2019**, *158*, 124–129.

(63) Wang, H.; Wang, Y.; Lv, J.; Li, Q.; Zhang, L.; Ma, Y. CALYPSO Structure Prediction Method and Its Wide Application. *Comput. Mater. Sci.* **2016**, *112*, 406–415.

(64) Li, Q.; Wang, H.; Ma, Y. M. Predicting New Superhard Phases. *J. Superhard Mater.* **2010**, *32* (3), 192–204.

(65) Mansouri Tehrani, A.; Brgoch, J. Hard and Superhard Materials: A Computational Perspective. *J. Solid State Chem.* **2019**, *271*, 47–58.

(66) Mayo, M.; Griffith, K. J.; Pickard, C. J.; Morris, A. J. Ab Initio Study of Phosphorus Anodes for Lithium- and Sodium-Ion Batteries. *Chem. Mater.* **2016**, *28* (7), 2011–2021.

(67) Zurek, E.; Yao, Y. Theoretical Predictions of Novel Superconducting Phases of BaGe 3 Stable at Atmospheric and High Pressures. *Inorg. Chem.* **2015**, *54* (6), 2875–2884.

(68) Mayo, M.; Morris, A. J. Structure Prediction of Li-Sn and Li-Sb Intermetallics for Lithium-Ion Batteries Anodes. *Chem. Mater.* **2017**, *29* (14), 5787–5795.

(69) Zhang, X.; Qin, J.; Sun, X.; Xue, Y.; Ma, M.; Liu, R. First-Principles Structural Design of Superhard Material of ZrB_4. *Phys. Chem. Chem. Phys.* **2013**, *15* (48), 20894–20899.

(70) Kumar, R. S.; Svane, A.; Vaitheeswaran, G.; Zhang, Y.; Kanchana, V.; Hofmann, M.; Campbell, S. J.; Xiao, Y.; Chow, P.; Chen, C.; et al. Pressure-Induced Valence and Structural Changes in $YbMn_2Ge_2$—Inelastic X-Ray Spectroscopy and Theoretical Investigations. *Inorg. Chem.* **2013**, *52* (2), 832–839.

(71) Gui, X.; Zhao, X.; Sobczak, Z.; Wang, C. Z.; Klimczuk, T.; Ho, K. M.; Xie, W. Ternary Bismuthide $SrPtBi_2$: Computation and Experiment in Synergism to Explore Solid-

State Materials. *J. Phys. Chem. C* **2018**, *122* (9), 5057–5063.

(72) Zhao, X.; Nguyen, M. C.; Zhang, W. Y.; Wang, C. Z.; Kramer, M. J.; Sellmyer, D. J.; Li, X. Z.; Zhang, F.; Ke, L. Q.; Antropov, V. P.; et al. Exploring the Structural Complexity of Intermetallic Compounds by an Adaptive Genetic Algorithm. *Phys. Rev. Lett.* **2014**, *112* (4), 45502.

(73) Jain, A.; Ong, P.; Hautier, G.; Chen, W.; Richards, W. D.; Dacek, S.; Cholia, S.; Gunter, D.; Skinner, D.; Ceder, G.; et al. Commentary: The Materials Project: A Materials Genome Approach to Accelerating Materials Innovation. *J. Chem. Phys.* **2013**, *1*, 11002.

(74) Curtarolo, S.; Setyawan, W.; Hart, G. L. W.; Jahnatek, M.; Chepulskii, R. V.; Taylor, R. H.; Wang, S.; Xue, J.; Yang, K.; Levy, O.; et al. AFLOW: An Automatic Framework for High-Throughput Materials Discovery. *Comput. Mater. Sci.* **2012**, *58*, 218–226.

(75) Kirklin, S.; Saal, J. E.; Meredig, B.; Thompson, A.; Doak, J. W.; Aykol, M.; Rühl, S.; Wolverton, C. The Open Quantum Materials Database (OQMD): Assessing the Accuracy of DFT Formation Energies. *npj Comput. Mater.* **2015**, *1* (1), 15010.

(76) O'Mara, J.; Meredig, B.; Michel, K. Materials Data Infrastructure: A Case Study of the Citrination Platform to Examine Data Import, Storage, and Access. *JOM* **2016**, *68* (8), 2031–2034.

(77) Schmidt, J.; Chen, L.; Botti, S.; Marques, M. A. L. Predicting the Stability of Ternary Intermetallics with Density Functional Theory and Machine Learning. *J. Chem. Phys.* **2018**, *148* (24), 241728.

(78) Hill, J.; Mulholland, G.; Persson, K.; Seshadri, R.; Wolverton, C.; Meredig, B. Materials Science with Large-Scale Data and Informatics: Unlocking New Opportunities. *MRS*

Bull. **2016**, *41* (5), 399–409.

(79) Fluck, E. Inorganic Crystal Structure Database (ICSD) and Standardized Data and Crystal Chemical Characterization of Inorganic Structure Types (TYPIX)-Two Tools for Inorganic Chemists and Crystallographers. *J. Res. Natl. Inst. Stand. Technol.* **1996**, *101* (3), 217–220.

(80) Balachandran, P. V.; Theiler, J.; Rondinelli, J. M.; Lookman, T. Materials Prediction via Classification Learning. *Sci. Rep.* **2015**, *5*.

(81) Awad, M.; Khanna, R.; Awad, M.; Khanna, R. Support Vector Regression. In *Efficient Learning Machines*; Apress, 2015; pp 67–80.

(82) Geurts, P.; Ernst, D.; Wehenkel, L. Extremely Randomized Trees. *Mach. Learn.* **2006**, *63* (1), 3–42.

(83) He, J.; Amsler, M.; Xia, Y.; Naghavi, S. S.; Hegde, V. I.; Hao, S.; Goedecker, S.; Ozoliņš, V.; Wolverton, C. Ultralow Thermal Conductivity in Full Heusler Semiconductors. *Phys. Rev. Lett.* **2016**, *117* (4), 46602.

(84) He, J.; Naghavi, S. S.; Hegde, V. I.; Amsler, M.; Wolverton, C. Designing and Discovering a New Family of Semiconducting Quaternary Heusler Compounds Based on the 18-Electron Rule. *Chem. Mater.* **2018**, *30* (15), 4978–4985.

(85) Kim, K.; Ward, L.; He, J.; Krishna, A.; Agrawal, A.; Wolverton, C. Machine-Learning-Accelerated High-Throughput Materials Screening: Discovery of Novel Quaternary Heusler Compounds. *Phys. Rev. Mater.* **2018**, *2* (12), 123801.

(86) Lotfi, S.; Zhang, Z.; Viswanathan, G.; Fortenberry, K.; Mansouri Tehrani, A.; Brgoch, J.

Targeting Productive Composition Space Through Machine-Learning Directed Inorganic Synthesis. *ChemRxiv Prepr.* **2020**.

(87) Legrain, F.; Carrete, J.; van Roekeghem, A.; Madsen, G. K. H.; Mingo, N. Materials Screening for the Discovery of New Half-Heuslers: Machine Learning versus Ab Initio Methods. *J. Phys. Chem. B* **2018**, *122* (2), 625–632.

(88) Medasani, B.; Gamst, A.; Ding, H.; Chen, W.; Persson, K. A.; Asta, M.; Canning, A.; Haranczyk, M. Predicting Defect Behavior in B2 Intermetallics by Merging Ab Initio Modeling and Machine Learning. *npj Comput. Mater.* **2016**, *2* (1), 1–10.

(89) Dolara, A.; Grimaccia, F.; Leva, S.; Mussetta, M.; Ogliari, E. Comparison of Training Approaches for Photovoltaic Forecasts by Means of Machine Learning. *Appl. Sci.* **2018**, *8* (2), 228.

(90) Agiorgousis, M. L.; Sun, Y.; Choe, D.; West, D.; Zhang, S. Machine Learning Augmented Discovery of Chalcogenide Double Perovskites for Photovoltaics. *Adv. Theory Simulations* **2019**, *2* (5).

(91) Iwasaki, Y.; Takeuchi, I.; Stanev, V.; Kusne, A. G.; Ishida, M.; Kirihara, A.; Ihara, K.; Sawada, R.; Terashima, K.; Someya, H.; et al. Machine-Learning Guided Discovery of a New Thermoelectric Material. *Sci. Rep.* **2019**, *9* (1).

(92) Amsler, M.; Ward, L.; Hegde, V. I.; Goesten, M. G.; Yi, X.; Wolverton, C. Ternary Mixed-Anion Semiconductors with Tunable Band Gaps from Machine-Learning and Crystal Structure Prediction. *Phys. Rev. Mater.* **2019**, *3* (3).

(93) Wei, J.; De Luna, P.; Bengio, Y.; Aspuru-Guzik, A.; Sargent, E. Use Machine Learning to Find Energy Materials. *Nature*. Nature Publishing Group 2017, pp 23–25.

(94) Liu, Y.; Zhu, Y.; Cui, Y. Challenges and Opportunities towards Fast-Charging Battery Materials. *Nature Energy*. **2019**, 540–550.

(95) Oliynyk, A. O.; Antono, E.; Sparks, T. D.; Ghadbeigi, L.; Gaultois, M. W.; Meredig, B.; Mar, A. High-Throughput Machine-Learning-Driven Synthesis of Full-Heusler Compounds. *Chem. Mater.* **2016**, *28* (20), 7324–7331.

(96) Viswanathan, G.; Oliynyk, A. O.; Antono, E.; Ling, J.; Meredig, B.; Brgoch, J. Single-Crystal Automated Refinement (SCAR): A Data-Driven Method for Determining Inorganic Structures. *Inorg. Chem.* **2019**, *58* (14), 9004–9015.

(97) Oliynyk, A. O.; Adutwum, L. A.; Harynuk, J. J.; Mar, A. Classifying Crystal Structures of Binary Compounds AB through Cluster Resolution Feature Selection and Support Vector Machine Analysis. *Chem. Mater.* **2016**, *28* (18), 6672–6681.

(98) Horikoshi, H.; Takeda, S.; Komura, Y. Prediction of Intermetallic Compounds. *Russ. Chem. Rev* **2009**, *78*, 569.

(99) Oliynyk, A. O.; Gaultois, M. W.; Hermus, M.; Morris, A. J.; Mar, A.; Brgoch, J. Searching for Missing Binary Equiatomic Phases: Complex Crystal Chemistry in the Hf–In System. *Inorg. Chem.* **2018**, *57* (13), 7966–7974.

(100) PANalytical, B. V. X'Pert HighScore Plus (Computer Software). *Almelo, The Netherlands*. **2006**.

(101) ICDD, P. D. F. International Centre for Diffraction Data. *Powder Diffraction File, Pennsylvania, USA*. **1997**.

(102) Le Bail, A. Whole Powder Pattern Decomposition Methods and Applications: A

Retrospection. *Powder Diffr.* **2005**, *20* (4), 316–326.

(103) Toby, B. H. EXPGUI , a Graphical User Interface for GSAS. *J. Appl. Crystallogr.* **2001**, *34* (2), 210–213.

(104) Larson, A. C.; Dreele, R. B. General Structure Analysis System (GSAS); Report LAUR 86-748; Los Alamos National Laboratory: Los Alamos, NM, 2000. Los Alamos National Laboratory, **2000**, 86-748.

(105) Harris, K. D. M.; Tremayne, M. Crystal Structure Determination from Powder Diffraction Data. *Chem. Mater.* **1996**, *8* (11), 2554–2570.

(106) Bruker, A. X. S. APEX2, SAINT and SADABS. *Bruker AXS Inc., Madison*. 2009.

(107) Sheldrick, G. M. TWINABS; University of Göttingen: Göttingen, Germany, **2008**.

(108) Sheldrick, G. M. XPREP in SHELXTL (Linux Version 6.0). *Bruker AXS Inc., Madison, Wisconsin, USA*. **2001**.

(109) Sheldrick, G. M. SHELXS-97, Program for Crystal Structure Solution. *University of Göttingen, Germany,*. **1997**.

(110) Sheldrick, G. M. SHELXL-97, Program for the Refinement of Crystal Structures. *University of Göttingen: Göttingen, Germany,*. **1997**.

(111) Sheldrick, G. M. Crystal Structure Refinement with SHELXL. *Acta Crystallogr. Sect. C Struct. Chem.* **2015**, *71* (1), 3–8.

(112) Momma, K.; Izumi, F. VESTA 3 for Three-Dimensional Visualization of Crystal, Volumetric and Morphology Data. *J. Appl. Crystallogr.* **2011**, *44* (6), 1272–1276.

(113) Hermann, A. *Reviews in Computational Chemistry*; Parrill, A. L., Lipkowitz, K. B., Eds.; John Wiley & Sons, Inc., Hoboken, New Jersey, **2017**.

(114) Seminario, J. M. An Introduction to Density Functional Theory in Chemistry. *Theor. Comput. Chem.* **1995**, *2* (C), 1–27.

(115) Fiolhais, C.; Nogueira, F.; Marques, M. A Primer in Density Functional Theory. *Mater. Today* **2003**, *6* (12), 59.

(116) Sholl, D. S.; Steckel, J. A. Density Functional Theory: A Practical Introduction. A John Willey & Sons. *Inc., Publ.* **2009**, 238.

(117) Kresse, G.; Furthmüller, J. Efficient Iterative Schemes for Ab Initio Total-Energy Calculations Using a Plane-Wave Basis Set. *Phys. Rev. B* **1996**, *54* (16), 11169–11186.

(118) Kresse, G.; Joubert, D. From Ultrasoft Pseudopotentials to the Projector Augmented-Wave Method. *Phys. Rev. B* **1999**, *59* (3), 1758–1775.

(119) Blöchl, P. E. Projector Augmented-Wave Method. *Phys. Rev. B* **1994**, *50* (24), 17953–17979.

(120) Perdew, J. P.; Burke, K.; Ernzerhof, M. Generalized Gradient Approximation Made Simple. *Phys. Rev. Lett.* **1996**, *77* (18), 3865–3868.

(121) Perdew, J. P.; Levy, M. Physical Content of the Exact Kohn-Sham Orbital Energies: Band Gaps and Derivative Discontinuities. *Phys. Rev. Lett.* **1983**, *51* (20), 1884–1887.

(122) Zurek, E.; Grochala, W. Predicting Crystal Structures and Properties of Matter under Extreme Conditions via Quantum Mechanics: The Pressure Is on. *Phys. Chem. Chem. Phys.* **2015**, *17* (5), 2917–2934.

(123) Wang, Y.; Lv, J.; Zhu, L.; Lu, S.; Yin, K.; Li, Q.; Wang, H.; Zhang, L.; Ma, Y. Materials Discovery via CALYPSO Methodology. *J. Phys. Condens. Matter* **2015**, *27* (20), 203203.

(124) Togo, A.; Oba, F.; Tanaka, I. First-Principles Calculations of the Ferroelastic Transition between Rutile-Type and $CaCl_2$-Type SiO_2 at High Pressures. *Phys. Rev. B* **2008**, *78* (13), 134106.

(125) Parlinski, K.; Li, Z. Q.; Kawazoe, Y. First-Principles Determination of the Soft Mode in Cubic ZrO_2. *Phys. Rev. Lett.* **1997**, *78* (21), 4063–4066.

(126) Agrawal, A.; Choudhary, A. Perspective: Materials Informatics and Big Data: Realization of The "fourth Paradigm" of Science in Materials Science. *APL Mater.* **2016**, *4* (5), 53208.

(127) Jain, A.; Ong, S. P.; Hautier, G.; Chen, W.; Richards, W. D.; Dacek, S.; Cholia, S.; Gunter, D.; Skinner, D.; Ceder, G.; et al. Commentary: The Materials Project: A Materials Genome Approach to Accelerating Materials Innovation. *APL Mater.* **2013**, *1* (1), 11002.

(128) Oses, C.; Gossett, E.; Hicks, D.; Rose, F.; Mehl, M. J.; Perim, E.; Takeuchi, I.; Sanvito, S.; Scheffler, M.; Lederer, Y.; et al. AFLOW-CHULL: Cloud-Oriented Platform for Autonomous Phase Stability Analysis. *J. Chem. Inf. Model.* **2018**, *58* (12), 2477–2490.

(129) Ghiringhelli, L. M.; Vybiral, J.; Levchenko, S. V; Draxl, C.; Scheffler, M. Big Data of Materials Science: Critical Role of the Descriptor. **2015**.

(130) Pauling, L.; Ewing, F. J. The Ratio of Valence Electrons to Atoms in Metals and Intermetallic Compounds. *Rev. Mod. Phys.* **1948**, *20* (1), 112–122.

(131) Miller, G. J.; Schmidt, M. W.; Wang, F.; You, T. S. Quantitative Advances in the Zintl-Klemm Formalism. *Struct. Bond.* **2011**, *139*, 1–55.

(132) Corbett, J. D. Polyatomic Zintl Anions of the Post Transition Elements. *Chem. Rev.* **1985**, *85*, 383–397.

(133) Meyer, G.; Naumann, D.; Wesemann, L. *Inorganic Chemistry Highlights*; Wiley-VCH, **2002**.

(134) Thimmaiah, S.; Miller, G. J. Rhombohedrally Distorted γ-$Au_{5-x}Zn_{8+y}$ Phases in the Au-Zn System. *Inorg. Chem.* **2013**, *52* (3), 1328–1337.

(135) Zachwieja, U. Einkristallzüchtung Und Strukturverfeinerung von $NaAu_2$- Ein Neuer Syntheseweg Für Alkalimetall-Gold-Verbindungen. *J. Alloys Compd.* **1993**, *196* (1–2), 171–172.

(136) Zachwieja, U. Synthesis and Structure of $CaAu_2$ and $SrAu_2$. *J. Alloys Compd.* **1996**, *235* (1), 12–14.

(137) Xiao, C.; Wang, L. L.; Maligal-Ganesh, R. V; Smetana, V.; Walen, H.; Thiel, P. A.; Miller, G. J.; Johnson, D. D.; Huang, W. Intermetallic $NaAu_2$ as a Heterogeneous Catalyst for Low-Temperature CO Oxidation. *J. Am. Chem. Soc.* **2013**, *135* (26), 9592–9595.

(138) Kwolek, E. J.; Widmer, R.; Groning, O.; Deniz, O.; Walen, H.; Yuen, C. D.; Huang, W. Y.; Schlagel, D. L.; Wallingford, M.; Thiel, P. A. The (111) Surface of $NaAu_2$: Structure, Composition, and Stability. *Inorg. Chem.* **2015**, *54* (3), 1159–1164.

(139) Kim, S. J.; Miller, G. J.; Corbett, J. D. Zigzag Chains of Alternating Atoms in A_2AuBi (A = Na, K) and K_2AuSb. Synthesis, Structure, and Bonding. *Z. Anorg. Allg. Chem.* **2010**, *636*

(1), 67–73.

(140) Liu, S.; Corbett, J. D. Ba_2AuTl_7: An Intermetallic Compound with a Novel Condensed Structure. *Inorg. Chem.* **2004**, *43* (8), 2471–2473.

(141) Li, B.; Corbett, J. D. Different Cation Arrangements in Au-In Networks. Syntheses and Structures of Six Intermetallic Compounds in Alkali-Metal-Au-In Systems. *Inorg. Chem.* **2007**, *46* (15), 6022–6028.

(142) Schwickert, C.; Gerke, B.; Pöttgen, R. Gold-Tin Ordering in $SrAu_2Sn_2$. *Z. Naturforsch* **2014**, *69*, 767–774.

(143) Lin, Q.; Corbett, J. D. The Low-Temperature Form of Calcium Gold Stannide, CaAuSn. *Acta Crystallogr. Sect. C Struct. Chem.* **2014**, *70* (8), 773–775.

(144) Lin, Q.; Mishra, T.; Corbett, J. D. Hexagonal-Diamond-like Gold Lattices, Ba and $(Au,T)_3$ Interstitials, and Delocalized Bonding in a Family of Intermetallic Phases $Ba_2Au_6(Au,T)_6$ (T = Zn, Cd, Ga, In, or Sn). *J. Am. Chem. Soc.* **2013**, *135* (30), 11023–11031.

(145) Celania, C.; Smetana, V.; Provino, A.; Pecharsky, V.; Manfrinetti, P.; Mudring, A.-V. R_3Au_9Pn (*R* = Y, Gd−Tm; *Pn* = Sb, Bi): A Link between $Cu_{10}Sn_3$ and $Gd_{14}Ag_{51}$. *Inorg. Chem.* **2017**, No. 56, 7247–7256.

(146) Mazzone, D.; Marazza, R.; Riani, P.; Zanicchi, G.; Cacciamani, G.; Fornasini, M. L.; Manfrinetti, P. The Isothermal Section at 600°C of the Ternary Pr-Au-Sn Phase Diagram. *CALPHAD Comput. Coupling Phase Diagrams Thermochem.* **2009**, *33* (1), 31–43.

(147) Boulet, P.; Vybornov, M.; Simopoulos, A.; Kostikas, A.; Noël, H.; Rogl, P. Phase Equilibria and Magnetic Studies in the Ternary System U–Ag–Sn. *J. Alloys Compd.* **1999**, *283* (1–2), 49–53.

(148) Bojin, M. D.; Hoffmann, R. The RE M E Phases. *Helv. Chim. Acta* **2003**, *86* (5), 1653–1682.

(149) Yannello, V. J.; Fredrickson, D. C. Generality of the 18-N Rule: Intermetallic Structural Chemistry Explained through Isolobal Analogies to Transition Metal Complexes. *Inorg. Chem.* **2015**, *54* (23), 11385–11398.

(150) Fickenscher, T.; Rodewald, U. C.; Niehaus, O.; Gerke, B.; Haverkamp, S.; Eckert, H.; Pöttgen, R. The Stannides $RE_3Au_6Sn_5$ (RE = La, Ce, Pr, Nd, Sm) – Synthesis, Structure, Magnetic Properties and 119Sn Mössbauer Spectroscopy. *Zeitschrift für Naturforsch. B* **2015**, *70* (6), 425–434.

(151) McMasters, O. .; Gschneidner, K. .; Bruzzone, G.; Palenzona, A. Stoichiometry, Crystal Structures and Some Melting Points of the Lanthanide-Gold Alloys. *J. Less Common Met.* **1971**, *25* (2), 135–160.

(152) Gratz, E.; Bauer, E.; Barbara, B. Transport and Magnetic Properties of $Ce_xLa_{1-x}Au_2$ ($0 \leq x \leq 0.7$) and $PrAu_2$ Related Content $CeCu_2$: A New Kondo Lattice Showing Magnetic Order. *J. Phys. Condens. Matter* **1989**, *1*.

(153) Saccone, A.; Macciò, D.; Giovannini, M.; Delfino, S. The Praseodymium-Gold System. *J. Alloys Compd.* **1997**, *247* (1–2), 134–140.

(154) Landelli, A.; Palenzona, A. On The MX_2 Phases of the Rare Earths with the IB, IIB and IIIB Group Elements and Their Crystal Structure. *J. Less Common Met.* **1968**, *15* (3),

273–284.

(155) Sheldrick, G. M. A Short History of SHELX. *Acta Crystallogr. Sect. A Found. Crystallogr.* **2008**, *64* (1), 112–122.

(156) Deringer, V. L.; Tchougreeff, A. L.; Dronskowski, R. Crystal Orbital Hamilton Population (COHP) Analysis as Projected from Plane-Wave Basis Sets. *J. Phys. Chem. A* **2011**, *115*, 5461–5466.

(157) Dronskowski, R.; Blöchl, P. E. Crystal Orbital Hamilton Populations (COHP). Energy-Resolved Visualization of Chemical Bonding in Solids Based on Density-Functional Calculations. *J. Phys. Chem* **1993**, *97*, 8617–8624.

(158) Kohout, M.; Wagner, F. R.; Grin, Y. Electron Localization Function for Transition-Metal Compounds. *Theor. Chem. Acc.* **2002**, *108* (3), 150–156.

(159) Grin, Y.; Savin, A.; Silvi, B. The ELF Perspective of Chemical Bonding. In *The Chemical Bond*; Wiley-VCH Verlag GmbH & Co. KGaA: Weinheim, Germany, 2014; pp 345–382.

(160) Kohout, M.; Savin, A. Influence of Core-Valence Separation of Electron Localization Function. *J. Comput. Chem.* **1997**, *18* (12), 1431–1439.

(161) Tang, W.; Sanville, E.; Henkelman, G. A Grid-Based Bader Analysis Algorithm without Lattice Bias. *J. Phys. Condens. Matter* **2009**, *21* (8), 84204.

(162) G M Sheldrick. CELL_NOW, Program for Unit Cell Determination. University of Göttingen, Germany**, 2008**.

(163) Pauling, L. Atomic Radii and Interatomic Distances in Metals. *J. Am. Chem. Soc.* **1947**, *69* (3), 542–553.

(164) Zachwieja, U. 1[Sn3/3]-Röhren Und $AuSn_3$-Baugruppen: Darstellung Und Struktur von Na_2AuSn_3. *Z. Anorg. Allg. Chem.* **2001**, *627* (3), 353–356.

(165) Okhotnikov, K.; Charpentier, T.; Cadars, S. Supercell Program: A Combinatorial Structure-Generation Approach for the Local-Level Modeling of Atomic Substitutions and Partial Occupancies in Crystals. *J. Cheminform.* **2016**, *8* (1), 17.

(166) Savin, A.; Nesper, R.; Wengert, S.; Fässler, T. F. ELF: The Electron Localization Function. *Angew. Chemie* **1997**, *36* (17), 1808–1832.

(167) Seshadri, R.; Hill, N. A. Visualizing the Role of Bi 6s "lone Pairs" in the off-Center Distortion in Ferromagnetic $BiMnO_3$. *Chem. Mater.* **2001**, *13* (9), 2892–2899.

(168) Mcmillan, P. F. High Pressure Synthesis of Solids. *Curr. Opin. Solid State Mater. Sci.* **1999**, *4*, 171–178.

(169) Badding, J. V. High-Pressure Synthesis, Characterization, and Tuning of Solid State Materials. *Annu. Rev. Mater. Sci* **1998**, *28*, 631–658.

(170) Prewitt, C. T.; Downs, R. T. High-Pressure Crystal Chemistry. *Rev. Mineral. Geochemistry* **1998**, *37*, 283–317.

(171) Tracy, C. L.; Park, S.; Rittman, D. R.; Zinkle, S. J.; Bei, H.; Lang, M.; Ewing, R. C.; Mao, W. L. High Pressure Synthesis of a Hexagonal Close-Packed Phase of the High-Entropy Alloy CrMnFeCoNi. *Nat. Commun.* **2017**, *8*.

(172) Zhang, W.; Oganov, A. R.; Goncharov, A. F.; Zhu, Q.; Boulfelfel, S. E.; Lyakhov, A. O.; Stavrou, E.; Somayazulu, M.; Prakapenka, V. B.; Konôpková, Z. Unexpected Stable Stoichiometries of Sodium Chlorides. *Science* **2013**, *342* (6165), 1502–1505.

(173) Wang, Y.; Ma, Y. Perspective: Crystal Structure Prediction at High Pressures. *J. Chem. Phys.* **2014**, *140* (4), 40901.

(174) Lyakhov, A. O.; Oganov, A. R.; Stokes, H. T.; Zhu, Q. New Developments in Evolutionary Structure Prediction Algorithm USPEX. *Comput. Phys. Commun.* **2013**, *184* (4), 1172–1182.

(175) Grochala, W.; Hoffmann, R.; Feng, J.; Ashcroft, N. W. The Chemical Imagination at Work in Very Tight Places. *Angew. Chemie Int. Ed.* **2007**, *46* (20), 3620–3642.

(176) Zurek, E. *Handbook of Solid State Chemistry*; Dronskowski, R., Ed.; **2017**.

(177) Miao, M. S. Caesium in High Oxidation States and as a P-Block Element. *Nat. Chem.* **2013**, *5* (10), 846–852.

(178) Liu, Z.; Botana, J.; Hermann, A.; Valdez, S.; Zurek, E.; Yan, D.; Lin, H.; Miao, M. Reactivity of He with Ionic Compounds under High Pressure. *Nat. Commun.* **2018**, *9* (1), 951.

(179) Dong, X.; Oganov, A. R.; Goncharov, A. F.; Stavrou, E.; Lobanov, S.; Saleh, G.; Qian, G.-R.; Zhu, Q.; Gatti, C.; Deringer, V. L.; et al. A Stable Compound of Helium and Sodium at High Pressure. *Nat. Chem.* **2017**, *9* (5), 440–445.

(180) Lu, C.; Miao, M.; Ma, Y. Structural Evolution of Carbon Dioxide under High Pressure. *J. Am. Chem. Soc.* **2013**, *135* (38), 14167–14171.

(181) Baettig, P.; Zurek, E. Pressure-Stabilized Sodium Polyhydrides: NaH_n (N > 1). *Phys. Rev. Lett.* **2011**, *106* (23), 237002.

(182) Yang, G.; Wang, Y.; Peng, F.; Bergara, A.; Ma, Y. Gold as a 6p-Element in Dense Lithium

Aurides. *J. Am. Chem. Soc.* **2016**, *138* (12), 4046–4052.

(183) Heyd, J.; Scuseria, G. E.; Ernzerhof, M. Hybrid Functionals Based on a Screened Coulomb Potential. *J. Chem. Phys.* **2003**, *118* (18), 8207–8215.

(184) Kelly, F. M.; Pearson, W. B. The Rubidium Transition at ~ 180°K. *Can. J. Phys.* **1955**, *33* (1), 17–24.

(185) Schwarz, U.; Grzechnik, A.; Syassen, K.; Loa, I.; Hanfland, M. Rubidium-IV: A High Pressure Phase with Complex Crystal Structure. *Phys. Rev. Lett.* **1999**, *83* (20), 4085–4088.

(186) Nelmes, R. J.; McMahon, M. I.; Loveday, J. S.; Rekhi, S. Structure of Rb-III: Novel Modulated Stacking Structures in Alkali Metals. *Phys. Rev. Lett.* **2002**, *88* (15), 155503.

(187) McMahon, M. I.; Rekhi, S.; Nelmes, R. J. Pressure Dependent Incommensuration in Rb-IV. *Phys. Rev. Lett.* **2001**, *87* (5), 55501.

(188) Weir, C. E.; Piermarini, G. J.; Block, S. On the Crystal Structures of Cs II and Ga II. *Cit. J. Chem. Phys.* **1971**, *54*, 1221.

(189) Moock, K.; Seppelt, K. Indications of Cesium in a Higher Oxidation State. *Angew. Chemie Int. Ed. English* **1989**, *28* (12), 1676–1678.

(190) Takemura, K.; Syassen, K. High-Pressure Structural Investigation of Cesium above 10 GPa. *Phys. Rev. B* **1985**, *32* (4), 2213–2217.

(191) Hull, A. W.; Davey, W. P. Graphical Determination of Hexagonal and Tetragonal Crystal Structures from X-Ray Data. *Phys. Rev.* **1921**, *17* (5), 549–570.

(192) Ling, R. G.; Belin, C. Preparation and Crystal Structure Determination of the New Intermetallic Compound $RbGa_3$. *Zeitschrift für Anorg. und Allg. Chemie* **1981**, *480* (9), 181–185.

(193) Deiseroth, H.-J.; Strunck, A. Hg_8("Mercubane") Clusters in $Rb_{15}Hg_{16}$. *Angew. Chemie Int. Ed. English* **1989**, *28* (9), 1251–1252.

(194) Botana, J.; Brgoch, J.; Hou, C.; Miao, M. Iodine Anions beyond -1: Formation of Li_nI (N = 2-5) and Its Interaction with Quasiatoms. *Inorg. Chem.* **2016**, *55* (18), 9377–9382.

(195) Pöttgen, R.; Johrendt, D. *Intermetallics*; OLDENBOURG WISSENSCHAFTSVERLAG: München, 2014.

(196) Lv, J.; Wang, Y.; Zhu, L.; Ma, Y. Predicted Novel High-Pressure Phases of Lithium. *Phys. Rev. Lett.* **2011**, *106* (1).

(197) Miao, M. S. Caesium in High Oxidation States and as a P-Block Element. *Nat. Chem.* **2013**, *5* (10), 846–852.

(198) Kolmogorov, A. N.; Shah, S.; Margine, E. R.; Bialon, A. F.; Hammerschmidt, T.; Drautz, R. New Superconducting and Semiconducting Fe-B Compounds Predicted with an Ab Initio Evolutionary Search. *Phys. Rev. Lett.* **2010**, *105* (21), 217003.

(199) Zhang, X.; Wang, Y.; Lv, J.; Zhu, C.; Li, Q.; Zhang, M.; Li, Q.; Ma, Y. First-Principles Structural Design of Superhard Materials. *J. Chem. Phys.* **2013**, *138* (11), 114101.

(200) Agrawal, A.; Meredig, B.; Wolverton, C.; Choudhary, A. A Formation Energy Predictor for Crystalline Materials Using Ensemble Data Mining. *2016 IEEE 16th Int. Conf. Data Min. Work.* **2016**, 1276–1279.

(201) Oliynyk, A. O.; Adutwum, L. A.; Rudyk, B. W.; Pisavadia, H.; Lotfi, S.; Hlukhyy, V.; Harynuk, J. J.; Mar, A.; Brgoch, J. Disentangling Structural Confusion through Machine Learning: Structure Prediction and Polymorphism of Equiatomic Ternary Phases ABC. *J. Am. Chem. Soc.* **2017**, *139* (49).

(202) Schmidt, J.; Shi, J.; Borlido, P.; Chen, L.; Botti, S.; Marques, M. A. L. Predicting the Thermodynamic Stability of Solids Combining Density Functional Theory and Machine Learning. *Chem. Mater.* **2017**, *29* (12), 5090–5103.

(203) Mansouri Tehrani, A.; Oliynyk, A. O.; Parry, M.; Rizvi, Z.; Couper, S.; Lin, F.; Miyagi, L.; Sparks, T. D.; Brgoch, J. Machine Learning Directed Search for Ultraincompressible, Superhard Materials. *J. Am. Chem. Soc.* **2018**, *140* (31), 9844–9853.

(204) Sun, W.; Bartel, C. J.; Arca, E.; Bauers, S. R.; Matthews, B.; Orvañanos, B.; Chen, B. R.; Toney, M. F.; Schelhas, L. T.; Tumas, W.; et al. A Map of the Inorganic Ternary Metal Nitrides. *Nat. Mater.* **2019**, *18* (7), 732–739.

(205) Schleder, G. R.; Padilha, A. C. M.; Acosta, C. M.; Costa, M.; Fazzio, A. From DFT to Machine Learning: Recent Approaches to Materials Science–a Review. *J. Phys. Mater.* **2019**, *2* (3), 32001.

(206) Ward, L.; Agrawal, A.; Choudhary, A.; Wolverton, C. A General-Purpose Machine Learning Framework for Predicting Properties of Inorganic Materials. *npj Comput. Mater.* **2016**, *2* (1), 16028.

(207) Deml, A. M.; O'Hayre, R.; Wolverton, C.; Stevanović, V. Predicting Density Functional Theory Total Energies and Enthalpies of Formation of Metal-Nonmetal Compounds by Linear Regression. *Phys. Rev. B* **2016**, *93* (8).

(208) Zheng, X.; Zheng, P.; Zhang, R.-Z. Machine Learning Material Properties from the Periodic Table Using Convolutional Neural Networks. *Chem. Sci.* **2018**, *9* (44), 8426–8432.

(209) Pedregosa; Michel, V.; Olivier; Blondel, M.; Prettenhofer, P.; Weiss, R.; Vanderplas, J.; Cournapeau, D.; Pedregosa, F.; Varoquaux, G.; et al. Scikit-Learn: Machine Learning in Python. *J. Mach. Learn. Res.* **2011**, *12*, 2825–2830.

(210) Ward, L.; Agrawal, A.; Choudhary, A.; Wolverton, C. A General-Purpose Machine Learning Framework for Predicting Properties of Inorganic Materials. *npj Comput. Mater.* **2016**, *2* (1), 16028.

(211) Obrowski, W. Die Struktur Der Diboride von Gold Und Silber. *Naturwissenschaften* **1961**, *48* (11), 428.

(212) Barber, C. B.; Dobkin, D. P.; Huhdanpaa, H.; Huhdanpaa, H. The Quickhull Algorithm for Convex Hulls. *ACM Trans. Math. Softw.* **1996**, *22* (4), 469–483.

(213) Jacobs, R.; Mayeshiba, T.; Booske, J.; Morgan, D. Material Discovery and Design Principles for Stable, High Activity Perovskite Cathodes for Solid Oxide Fuel Cells. *Adv. Energy Mater.* **2018**, *8* (11).

(214) Sun, W.; Dacek, S. T.; Ong, S. P.; Hautier, G.; Jain, A.; Richards, W. D.; Gamst, A. C.; Persson, K. A.; Ceder, G. The Thermodynamic Scale of Inorganic Crystalline Metastability. *Sci. Adv.* **2016**, *2* (11).

(215) Lotfi, S.; Oliynyk, A. O.; Brgoch, J. Polyanionic Gold–Tin Bonding and Crystal Structure Preference in $REAu_{1.5}Sn_{0.5}$ (RE = La, Ce, Pr, Nd). *Inorg. Chem.* **2018**, *57* (17), 10736–10743.

(216) Larsson, P.; Ahuja, R.; Liivat, A.; Thomas, J. O. Structural and Electrochemical Aspects of Mn Substitution into Li_2FeSiO_4 from DFT Calculations. *Comput. Mater. Sci.* **2010**, *47* (3), 678–684.

(217) Brgoch, J.; Mahmoud, Y. A.; Miller, G. J. Atomic Site Preferences and Its Effect on Magnetic Structure in the Intermetallic Borides $M_2Fe(Ru_{0.8}T_{0.2})_5B_2$ (M=Sc, Ti, Zr; T=Ru, Rh, Ir). *J. Solid State Chem.* **2012**, *196*, 168–174.

(218) Zhak, O. V.; Kuz'ma, Y. B.; Pugach, O. V. 500°C Section of the Y-Ag-Sb Phase Diagram. *Inorg. Mater.* **2003**, *39* (4), 323–326.

(219) Paufler, P. P. Villars, L. D. Calvert. Pearson's Handbook of Crystallographic Data for Intermetallic Phases. *Cryst. Res. Technol.* **1987**, *22* (11), 1436–1436.

(220) Lin, Q.; Corbett, J. D. Interpenetrating Networks of Three-Dimensional Penrose Tiles in $CaAu_3Ga$, the Structurally Simplest Cubic Approximant of an Icosahedral Quasicrystal.

(221) Voßwinkel, D.; Niehaus, O.; Pöttgen, R. New Rhodium-Rich Germanides $RERh_6Ge_4$ (RE = Y, La, Pr, Nd, Sm-Lu). *Zeitschrift fur Anorg. und Allg. Chemie* **2013**, *639* (14), 2623–2630.

(222) Venturini, G.; Méot-Meyer, M.; Marêché, J. F.; Malaman, B.; Roques, B. De Nouveaux Isotypes de $U_2Co_3Si_5$ Ou $Lu_2Co_3Si_5$ Dans Les Systems R-T-Ge (R = Elements Des Terres Rares; T = Ru, Co, Rh, Ir). Supraconductivite de $Y_2Ir_3Ge_5$. *Mater. Res. Bull.* **1986**, *21* (1), 33–39.

(223) Gil, A.; Szytuła, A.; Tomkowicz, Z.; Wojciechowski, K.; Zygmunt, A. Magnetic Properties of $RNiSi_2$ and $RNiGe_2$ Compounds. *J. Magn. Magn. Mater.* **1994**, *129* (2–3),

271–278.

(224) Oliynyk, A. O.; Stoyko, S. S.; Mar, A. Many Metals Make the Cut: Quaternary Rare-Earth Germanides $RE_4M_2InGe_4$ (M = Fe, Co, Ni, Ru, Rh, Ir) and $RE_4RhInGe_4$ Derived from Excision of Slabs in RE_2InGe_2. *Inorg. Chem.* **2015**, *54* (6), 2780–2792.

(225) Haiying, B.; Zelinska, O. Y.; Tkachuk, A. V.; Mar, A. Structures and Physical Properties of Rare-Earth Chromium Germanides $RECrGe_3$ (RE = La - Nd, Sm). *Chem. Mater.* **2007**, *19* (18), 4613–4620.

(226) Morozkin, A. V.; Knotko, A. V.; Yapaskurt, V. O.; Yuan, F.; Mozharivskyj, Y.; Pani, M.; Provino, A.; Manfrinetti, P. The Ho-Ni-Ge System: Isothermal Section and New Rare-Earth Nickel Germanides. *J. Solid State Chem.* **2015**, *225*, 193–201.

(227) Rieger, W.; Parthé, E. Ternäre Erdalkali-Und Seltene Erdmetall-Silicide Und-Germanide Mit $ThCr_2Si_2$-Struktur. *Monatshefte für Chemie* **1969**, *100* (2), 444–454.

(228) Szytuła, A.; Kaczorowski, D.; Gondek, L.; Arulraj, A.; Baran, S.; Penc, B. Magnetic Properties of $NdAu_2Ge_2$. *J. Magn. Magn. Mater.* **2009**, *321* (20), 3402–3405.

(229) Rossi, D.; Marazza, R.; Ferro, R. Ternary Rare Earth Alloys: RAuGe Compounds. *J. Alloys Compd.* **1992**, *187* (2), 267–270.

(230) Schnelle, W.; Pöttgen, R.; Kremer, R. K.; Gmelin, E.; Jepsen, O. The Crystal Structure, Magnetic Susceptibility, Electrical Resistivity, Specific Heat, and Electronic Band Structure of RAuGe (R = Sc, Y, La, Lu). *J. Phys. Condens. Matter* **1997**, *9* (7), 1435–1450.

(231) Pöttgen, R.; Borrmann, H.; Kremer, R. K. Ferromagnetic Ordering in CeAuGe. *J. Magn.*

Magn. Mater. **1996**, *152* (1–2), 196–200.

(232) Menon, L.; Adroja, D. T.; Rainford, B. D.; Malik, S. K.; Yelon, W. B. Neutron Scattering Studies on CeRhSb. *Solid State Commun.* **1999**, *112* (2), 85–89.

(233) Krimmel, A.; Hemberger, J.; Kegler, C.; Nicklas, M.; Engelmayer, A.; Knebel, G.; Fritsch, V.; Reehuis, M.; Brando, M.; Loidl, A. The Evolution from Long-Range Magnetic Order to Spin-Glass Behaviour in $PrAu_2(Si_{1-x}Ge_x)_2$ Related Content The Evolution from Long-Range Magnetic Order to Spin-Glass Behaviour in $PrAu_2(Si_{1-x}G$. *J. Phys. Condens. Matter* **1999**, *11* (36), 6991–7003.

(234) Cromer, D. T.; Larson, A. C.; Roof Jr, R. B. *The Crystal Structure of Pu3Pd4**; 1973; Vol. 29.

(235) Palenzona, A. The Crystal Structure and Lattice Constants of R_3Pt_4 Compounds. *J. Less-Common Met.* **1977**, *53* (1), 133–136.

(236) Seibel, E. M.; Schoop, L. M.; Xie, W.; Gibson, Q. D.; Webb, J. B.; Fuccillo, M. K.; Krizan, J. W.; Cava, R. J. Gold-Gold Bonding: The Key to Stabilizing the 19-Electron Ternary Phases LnAuSb (Ln = La-Nd and Sm). *J. Am. Chem. Soc.* **2015**, *137* (3), 1282–1289.

(237) Schmidbaur, H.; Schier, A. A Briefing on Aurophilicity. *Chem. Soc. Rev.* **2008**, *37* (9), 1931–1951.

(238) Johrendt, D.; Felser, C.; Jepsen, O.; Andersen, O. K.; Mewis, A.; Rouxel, J. LMTO Band Structure Calculations of $ThCr_2Si_2$-Type Transition Metal Compounds. *J. Solid State Chem.* **1997**, *130* (2), 254–265.

(239) Gladyshevskii, E. I. Crystal Structure of the Digermanide of Rare Earth Elements. *J.*

Struct. Chem. **1964**, *5* (4), 523–529.

(240) Bartlett, N. Relativistic Effects and the Chemistry of Gold. *Gold Bull.* **1998**, *31* (1), 22–25.